

ARMY RESEARCH LABORATORY



Optically Assisted Three Dimensional Packaging for Multichip Module Applications

Michael Wang

ARL-CR-271

June 1996

prepared by
Physical Optics Corporation
2545 West 237th Street
Torrance, CA 90505

under contract
DAAL01-93-C-3318

19960729 112

APPROVED FOR PUBLIC RELEASE; DISTRIBUTION IS UNLIMITED.

DTIC QUALITY INSPECTED 1

NOTICES

Disclaimers

The findings in this report are not to be construed as an official Department of the Army position, unless so designated by other authorized documents.

The citation of trade names and names of manufacturers in this report is not to be construed as official Government endorsement or approval of commercial products or services referenced herein.

DISCLAIMER NOTICE



THIS DOCUMENT IS BEST QUALITY AVAILABLE. THE COPY FURNISHED TO DTIC CONTAINED A SIGNIFICANT NUMBER OF COLOR PAGES WHICH DO NOT REPRODUCE LEGIBLY ON BLACK AND WHITE MICROFICHE.

REPORT DOCUMENTATION PAGE			Form Approved OMB NO. 0704-0188	
Public reporting burden for this collection of information is estimated to average 1 hour per response, including the time for reviewing instructions, searching existing data sources, gathering and maintaining the data needed, and completing and reviewing the collection of information. Send comment regarding this burden estimate or any other aspect of this collection of information, including suggestions for reducing this burden, to Washington Headquarters Services, Directorate for Information Operations and Reports, 1215 Jefferson Davis Highway, Suite 1204, Arlington, VA 22202-4302, and to the Office of Management and Budget, Paperwork Reduction Project (0704-0188), Washington, DC 20503.				
1. AGENCY USE ONLY (Leave blank)		2. REPORT DATE June 1996		3. REPORT TYPE AND DATES COVERED Final Report: 29 Apr 93 to 8 Aug 95
4. TITLE AND SUBTITLE OPTICALLY ASSISTED THREE DIMENSIONAL PACKAGING FOR MULTICHIP MODULE APPLICATIONS			5. FUNDING NUMBERS C: DAAL01-93-C-3318	
6. AUTHOR(S) Michael Wang				
7. PERFORMING ORGANIZATION NAMES(S) AND ADDRESS(ES) Physical Optics Corporation 2545 West 237th Street, Suite B Torrance, CA 90505			8. PERFORMING ORGANIZATION REPORT NUMBER	
9. SPONSORING / MONITORING AGENCY NAME(S) AND ADDRESS(ES) US Army Research Laboratory (ARL) Physical Sciences Directorate ATTN: AMSRL-PS-EB (Tsang-Der Ni) Fort Monmouth, NJ 07703-5601			10. SPONSORING / MONITORING AGENCY REPORT NUMBER ARL-CR-271	
11. SUPPLEMENTARY NOTES				
12a. DISTRIBUTION / AVAILABILITY STATEMENT Approved for public release; distribution is unlimited.			12 b. DISTRIBUTION CODE	
13. ABSTRACT (Maximum 200 words) This report presents a board-to-board optical interconnect system for 3-D packaging of multichip module applications. The interconnect prototype demonstrates both waveguide-backplane-fiber interconnects and fiber ribbon interconnects for inter-board applications. On the fiber-ribbon-based board-to-board interconnects, distributed feedback laser arrays are used as signal transmitters. PIN type photo-detector arrays are used for optical-to-electrical signal conversion at the receiver board. On the waveguide-backplane-fiber interconnects, channel waveguide electro-optic modulator arrays were used as signal transmitters that convert chip electrical signals to optical signals. These devices will potentially have a much lower cost and will operate at a much higher speed for use in computing systems and other high-speed electronic instruments such as signal generators, oscilloscopes, signal amplifiers, and transceiver modules.				
14. SUBJECT TERMS Packaging; multichip module packaging; modulators; optics; optical circuits; optical waveguides; waveguides; fiber optics; prisms(optics); signal conversion; laser modulators; semiconductor lasers; photodetectors			15. NUMBER IF PAGES 115	
			16. PRICE CODE	
17. SECURITY CLASSIFICATION OR REPORT Unclassified		18. SECURITY CLASSIFICATION OF THIS PAGE Unclassified		19. SECURITY CLASSIFICATION OF ABSTRACT Unclassified
			20. LIMITATION OF ABSTRACT UL	

TABLE OF CONTENTS

	ABSTRACT	v
1.0	INTRODUCTION	1
2.0	PRINCIPLE OF OPTICAL INTERCONNECTS.....	3
2.1	Board-to-Board Optical Interconnect Structures	3
2.2	Waveguide-Backplane-Waveguide Optical Interconnect Structures	6
2.2.1	Channel Waveguide Arrays	9
2.2.2	Channel Waveguide Electro-Optic Modulators	11
2.2.3	Channel Waveguide Modulator Arrays	12
2.2.4	Channel Waveguide Modes and Radiated Beam Collimation	14
2.2.5	Holographic Backplane and Chromatic Sensitivity.....	18
2.2.6	Design of Achromatic Holographic Grating Couplers	23
2.2.7	Achromatic Prism-Glass Optical Backplane.....	32
2.2.8	Guided Beam Receiver Array Design and Consideration.....	33
2.2.9	Advantages and Disadvantages of the Waveguide-Backplane Interconnect Concept.....	36
2.3	Fiber Ribbon Based Board-to-Board Optical Interconnect Structure	37
2.3.1	Laser Transmitter Arrays	37
2.3.2	Photodetector Receiver Arrays.....	39
2.3.3	Fiber Ribbons and Ribbon Connectors.....	40
2.3.4	Advantages and Disadvantages of the Fiber Ribbon Based Interconnect Concept.....	41
2.4	Revised Phase II Prototype Structure	42
3.0	PROTOTYPE DESIGN, FABRICATION, PACKAGING, AND PERFORMANCE.....	46
3.1	Design and Fabrication of Waveguide Modulator Arrays.....	46
3.1.1	Design and Fabrication of Waveguide Modulator	46
3.1.2	Modulator End-Face Polishing and Optical Coupling.....	52
3.1.3	Electrode Pattern Design and Fabrication.....	54
3.1.4	Modulator Testing.....	57
3.1.5	Summary of Design and Fabrication Parameters	58
3.1.6	Thermal Annealing for Modulator Performance Optimization.....	60
3.1.7	Fabrication of Modulator Arrays	62
3.1.8	Optical Throughput and Loss Analysis	65
3.1.9	Modulator Frequency Response	68
3.1.9.1	RLC Lumped-Element Modulator Circuit Model	68
3.1.9.2	Determination of Circuit Element Values.....	72
3.1.9.3	Modulator Simulations	74
3.1.10	Fiber/Waveguide Pigtail	74
3.2	Receiver Fabrication for Mid-Program Prototype.....	77
3.2.1	Design Guidelines Established from the Mid-Program Prototype.....	80
3.2.2	Mid-Program Board-to-Board Optical Interconnect Prototype.....	81
3.3	Design and Fabrication of Final Prototype.....	85
3.3.1	Design and Fabrication of Transmitter and Receiver Boards.....	86
3.3.2	Design and Fabrication of Prism-Glass Optical Backplane.....	89
3.3.3	Prototype Packaging Assembly and Interconnect Demonstration	89
3.3.3.1	Assembly of the Phase II Interconnect Prototype	89
3.3.3.2	Other Phase II Delivery	92
3.4	Technical Difficulties Encountered in the Assembly of the Final Prototype.....	94
3.4.1	Replacement of the Multimode Fibers to Improve Numerical Aperture (NA) Matching.....	94

TABLE OF CONTENTS (CONT)

3.4.2	Reparation of Integrated Laser Diode Array and Detector Array.....	95
3.4.3	Solution of Over Heating Problems on the Receiver Board.....	95
3.4.4	Repair of the Receiving Circuit Board.....	96
4.0	POTENTIAL APPLICATIONS.....	96
5.0	COMMERCIAL ACTIVITIES.....	97
6.0	PUBLICATIONS RESULTING FROM PROGRAM DEVELOPMENT.....	99
7.0	CONCLUSION.....	100
8.0	REFERENCES.....	101

LIST OF FIGURES

1-1	Board-to-Board Optical Interconnects for 3-D Packaging of Multichip Modules.....	3
2-1	Backplane Substrate Optical Interconnects Using laser Transmitters.....	4
2-2	Holographic Optical Backplane Interconnects Using Reflection Mirrors.....	4
2-3	Wafer Scale Chip-to-Chip Optical Interconnects Using Channel Waveguide Arrays.....	6
2-4	Input Coupling of a High Power Laser Diode to a Fiber Fanout and Channel Waveguide Array.....	8
2-5	Input Coupling of a High-Power Laser Diode to Channel Waveguide Arrays.....	8
2-6	Schematic of Straight Channel Waveguide Arrays.....	10
2-7	Waveguide Mach-Zehnder Interferometer Modulator.....	12
2-8	Schematic of a Parallel Mach-Zehnder Modulator Array.....	13
2-9	Schematic of a Modulator Array with One-to-Four Waveguide Fanout.....	14
2-10	Channel Waveguide Mode Profiles.....	16
2-11	Length of a GRIN Lens and its Effect on Point Source Location for Collimation.....	18
2-12	Backplane Substrate Interconnect with Slanted Input and Output Coupling Holograms.....	19
2-13	Definition of Recording Angles for Slanted Holographic Gratings.....	20
2-14	Schematic of a Holographic Bragg Diffraction.....	21
2-15	Wavelength Variation Causes Substrate Beam Spot Shift at the Output Coupling Hologram in a Two-Grating Structure.....	23
2-16	Three-grating system for backplane substrate interconnects, providing stable output diffraction angle θ and output beam position over the entire laser diode wavelength shift ranges.....	24
2-17	Relationship Between angle β' and Angle α for Different Ratios $g = m_2/m_1$ Satisfying the Achromatic Coupling Condition.....	27
2-18	The Ratio f as a Function of Angle α Under Different g Values. Minimizing f is important for reducing total substrate beam propagation length and thus propagation and scattering losses.....	28

2-19	Calculated Achromatic Wavelength Range $R_{\lambda, 1}$ for Beam Spot Shift Compensation at $g = 0.05$	32
2-20	Prism-Based Optical Backplane.....	33
2-21	Butt Coupling of Receiving Waveguides and PIN Photodetectors.....	34
2-22	Fiber Based Guided Beam Receiver Arrays	35
2-23	Rugged Fiber/Photodetector Packaging Using Fermionic Photodetectors with Fiber Guides	35
2-24	Photograph of the DFB Laser Diode Array Delivered by JPL to POC	38
2-25	Photodetector Array Delivered by JPL to POC.....	39
2-26	Multimode Fiber Ribbon.....	40
2-27	Schematic of the Fiber Ribbon Connector	41
2-28	Revised Schematic of the Board-to-Board Optical Interconnect Prototype.....	43
2-29	Schematic of the First Circuit Board.....	45
2-30	Schematic of the second circuit board.	45
3-1	Design Layout of POC's Single-Unit Mach-Zehnder Waveguide Modulator.....	47
3-2	S-Bending at the y-Junction of the Mach-Zehnder Waveguide Modulator.....	48
3-3	Mask Pattern of the Waveguide Mach-Zehnder Modulator	49
3-4	Process for Channel Waveguide Fabrication on an x-Cut LiNbO_3 Substrate.....	50
3-5	Schematic of Butt-Coupling From Fiber to Channel Waveguide	53
3-6	Near Field View of the Output Spot from a Mach-Zehnder Modulator.....	53
3-7	Mode confinement in the Mach-Zehnder modulator mode profile of the guided light.....	54
3-8	Electrode Mask Pattern	55
3-9	Cross sectional view of electrodes on channel waveguides.....	55
3-10	Fabrication process for electrode pattern deposition on a channel waveguide sample.	56
3-11	Probe testing of waveguide modulator array	57
3-12	Over 99% modulation depth produced by POC waveguide modulator.	58
3-13	Measured waveguide modulator modulation depth of about 36% under a driving voltage of 15 V.....	61
3-14	Measured waveguide modulator modulation depth of about 70% under a driving voltage of 15 V.....	61
3-15	Waveguide layout of a fanout Mach-Zehnder modulator array device.....	64
3-16	Developed waveguide modulator array with four element modulators and channel waveguide fanouts	65
3-17	Block diagram of the experimental setup for optical throughput measurement.....	66
3-18	RLC Circuit Model for Grating Coupler Modulator	69
3-19	Circuit Model Simulations	70
3-20	Circuit Model Simulation with and without Frequency-Dependent Electrode Resistance.....	71
3-21	Frequency Response of POC Waveguide Modulator.....	74
3-22	Laser, Fiber, and Waveguide Coupling.....	75
3-23	Optical Pigtailling Alignment Stage.....	75

3-24	Packaged Modulator Unit with an Input Fiber and an Output Collimation GRIN Lens.....	76
3-25	Pigtailed modulator Array with GRIN Lens Array	77
3-26	A High-Speed Receiver Design	79
3-27	Fabricated 1.5 Gbits/s Optical Receiver Module	80
3-28	Packaged Waveguide Modulator Transmitter.....	81
3-29	Photograph of the optical backplane constructed by a piece of polished optical glass and a pair of prisms.....	83
3-30	Packaging Hardware	84
3-31	Packaged Board-to-Board Optical Interconnect Prototype.....	84
3-32	Photograph of the Interconnect Performance.....	85
3-33	Schematic of the Receiver Circuit.....	87
3-34	Schematic of Laser Driver Circuit.....	88
3-35	Schematic of Temperature Control Circuit for Laser Diode Array	88
3-36	Final Prototype During Assembly	90
3-37	First Circuit Board in Assembly	91
3-38	Second Circuit Board in Assembly	92
3-39	Fiber Pigtailed Four-Element Modulator Array Chip.....	93
3-40	Single-Fiber Pigtailed Modulator Chip.....	93
3-41	Two Additional Un-pigtailed Modulator Chips	94
4-1	High-Speed Compact Packaged Hybrid Optic/electronic Computer	97
5-1	Packaged Laser Transmitter Array in a Butterfly Package with Temperature Control.....	98
5-2	Another type of laser transmitter array with butt-coupling from laser array to fiber ribbon	98
5-3	Receiver Array with Butt-Coupling from Fiber Ribbon to Photodetector Array	99

LIST OF TABLES

3-1	APE Parameters Used By POC.....	59
3-2	Fabrication Parameters of POC's Integrated Mach-Zehnder Modulators.....	60
3-3	Optical Throughput and Related Losses.....	67

ABSTRACT

Physical Optics Corporation proposed and demonstrated in this Phase II program board-to-board optical interconnects for 3-D packaging of multichip module applications. The interconnect prototype demonstrated both waveguide-backplane-fiber interconnects and fiber ribbon interconnects for inter-board applications.

On the waveguide-backplane-fiber interconnects, channel waveguide electro-optic modulator arrays were used as signal transmitters that convert chip electrical signals to optical signals. We have developed miniaturized Mach-Zehnder waveguide modulator arrays for this purpose. An external high power CW laser diode is the optical source for the modulators and optical interconnects. It creates no heat problem for the circuit boards or MCM units. The holographic backplane, which was successfully demonstrated in Phase I was further examined, but was considered too wavelength-sensitive for the hologram pair configuration, since slight laser wavelength fluctuation due to ambient temperature and laser bias can greatly affect backplane performance. We have thus designed and published a new technique of achieving achromatic backplane couplings with three holographic elements. A simple wavelength-insensitive configuration based on prism pair was actually used for the Phase II backplane interconnects. Multimode fiber arrays with excellent backplane beam reception coupling and good coupling with high-speed photodetectors were used at the receiving board.

On the fiber ribbon based board-to-board interconnects, distributed feedback laser arrays were used as signal transmitters. PIN type photodetector arrays were used for optical-to-electrical signal conversion at the receiver boards. Both laser diode arrays and photodetector arrays were specially fabricated with array element spacing matched with the commercially available fiber ribbon spacing. The fiber ribbons were used to connect laser arrays to photodetector arrays with a simple plug-in connection, making interconnect alignment easy enough for inexperienced engineers.

During the program study, extensive efforts were also directed to the design and fabrication of waveguide electro-optic modulator arrays, which are not commercially available. The study will be useful for future POC commercialization of related photonic devices. We have also spent significant effort on backplane design in the context of solving the chromatic sensitivity problem. Collaboration with JPL has resulted in the availability of

DFB laser arrays and photodetector arrays for the fiber ribbon-based interconnects. Furthermore, we have demonstrated a laser transmitter array in a butterfly package for commercial consideration.

This research and development has resulted in several deliverables in addition to quarterly reports and this final technical report detailing related technical issues. These deliverables are: (1) a board-to-board optical interconnect prototype demonstrating both waveguide/backplane optical interconnects and fiber ribbon-based optical interconnects; (2) a fiber pigtailed four-element modulator array chip; (3) a single fiber pigtailed modulator chip; and (4) two additional un-pigtailed modulator chips.

The successful demonstration of backplane optical interconnects can result in a number of applications, including 3-D packaging of MCMs with immunity to EMI. These devices will have increased speed and reduced cost for use in computing systems and other high-speed electronic instruments such as signal generators, oscilloscopes, signal amplifiers, and transceiver modules.

1.0

INTRODUCTION

On-going research and development efforts in very large scale integrated (VLSI) circuits have led to a dramatic decrease in component size and an increase in overall chip size [1,2]. The increase in complexity and density of ICs is expected to increase the speed and reliability of the systems in which they are used [3] and, at the same time, reduce the amount of power consumed. One major limitation of packaged chips which use electrical interconnects is the relatively long distances required to interconnect devices and circuits on a common substrate, or to connect chip packages on different PC boards. Often, the interconnections use aluminum or polysilicon lines, which extend over distances greater than several millimeters. Ohmic power losses, long delay times, excessive wafer space, and complex patterning techniques are some of the other limitations associated with electrical interconnects. Operating speed, for example, can be limited by external electromagnetic interference (EMI) from connecting wires, which can keep speeds to less than a few hundred MHz for compact systems [4].

In comparison to electrical interconnects, optical interconnects offer several advantages, including the ability to achieve high data rate signal transmission, large fanout densities, and the ability to reduce capacitive and inductive loading effects [1,2,4-17]. Because of their high speed and wide bandwidth capabilities (which are independent of interconnection distance), optical interconnects are excellent candidates for the replacement of electrical interconnects in a variety of applications, including those which require high data rate operation, long distance signal propagation (> 1 mm), low power consumption, and immunity to radiation and EMI [4]. A comparison between optical and electrical interconnects, based on power and speed considerations [4], has shown that the switching energy for electrical interconnects increases abruptly, making them unsuitable for practical systems. Crosstalk and EMI effects can further degrade their performance, making optical interconnects very attractive for chip-to-chip and board-to-board applications.

A large number of optical interconnect architectures have been reported in literature [1,15-42]. These include free-space interconnects [1,15-24], fiber interconnects [1,25,26], guided wave planar interconnects [27-30], and substrate wave interconnects [31-42]. Free-space interconnects require an air gap and the use of diffractive, reflective, and/or focusing elements. Their use is limited in stacked architectures, such as three-dimensional packaged systems, because they can suffer from severe alignment and fragility problems. Fiber interconnects require point-to-point fiber connections, are expensive to fabricate, and are

bulky. Furthermore, the inability to achieve small fiber bending radii limits the use of optical fiber in short distance point-to-point transmission. Recent advancements in fiber ribbon technology and ribbon connectors can greatly reduce these packaging issues and facilitate some applications in board-to-board interconnects. The other interconnection schemes, including guided wave and substrate wave interconnects, offer the potential advantages of compactness, high alignment accuracy, and efficient signal transmission.

This Phase II research program proposed by Physical Optics Corporation (POC) was aimed at the demonstration of board-to-board optical interconnects using waveguide and backplane substrate interconnect schemes for three-dimensional (3-D) MCM packaging applications. Commercial prototype demonstration was also a target of the Phase II program. The original proposed board-to-board interconnect architecture is depicted in Figure 1-1. The interconnect principle and a description of the structure are given in Section 2 of this report, where the design guidelines and the revision of the prototype structure are detailed as well. Section 3 describes the device fabrication procedures, including design and fabrication of channel waveguide modulators and modulator arrays on LiNbO_3 , output beam collimation using GRIN lenses, backplane formation, design and fabrication of transmitter and receiver array units, and interconnect system packaging and demonstration. The potential applications of the interconnect structure are summarized in Section 4. Section 5 describes the commercial activities in the Phase II performance period. The resulting published papers are attached in Section 6. Finally, concluding remarks are given in Section 7.

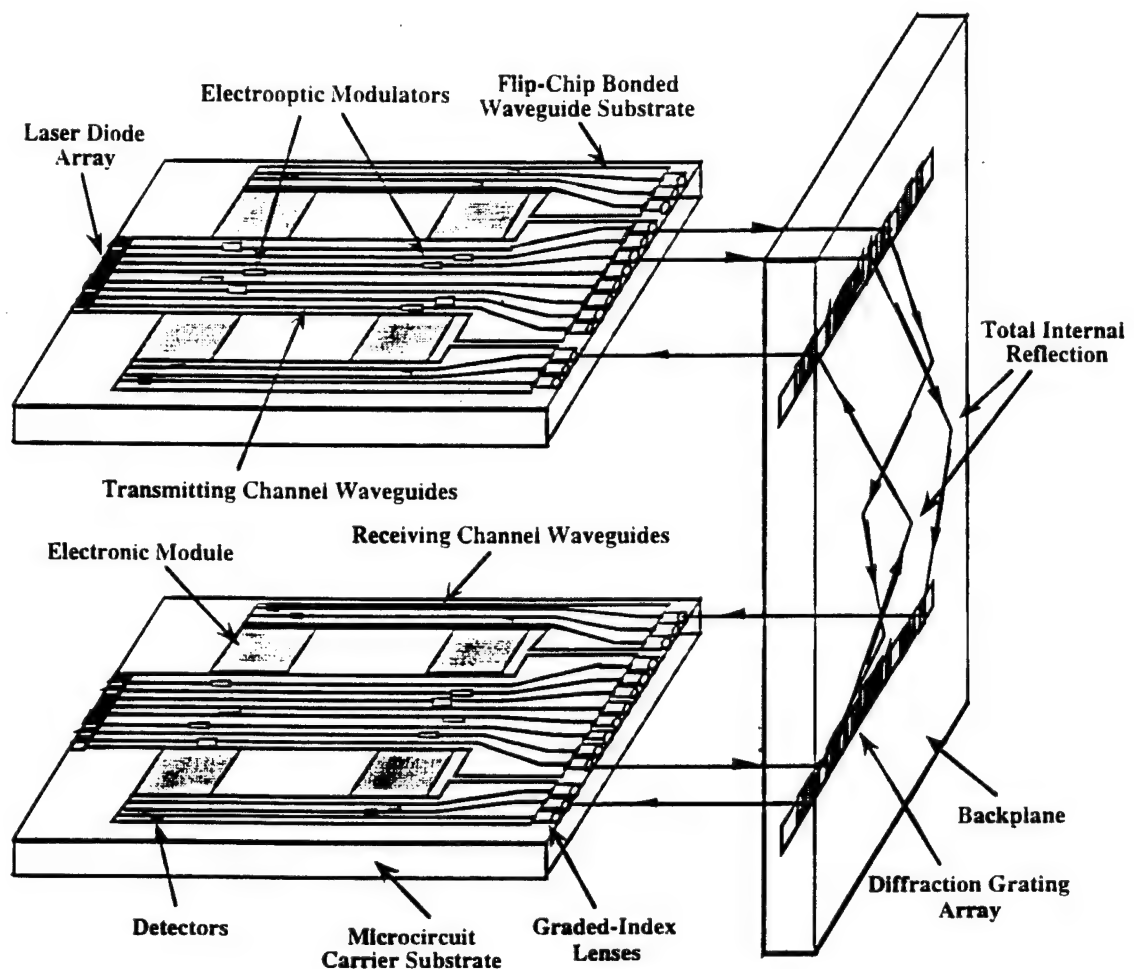


Figure 1-1
Board-to-Board Optical Interconnects for 3-D Packaging of Multichip Modules

2.0 PRINCIPLE OF OPTICAL INTERCONNECTS

2.1 Board-to-Board Optical Interconnect Structures

Two basic potential structures for board-to-board interconnections are illustrated in Figures 1-1 and 2-1. Each circuit board consists of a laser or a channel waveguide electro-optic modulator transmitter (Tx) and a photodetector or waveguide/detector receiver (Rx) as its optical I/O. An electrical signal to be transmitted is first converted to an intensity-modulated optical signal through a transmitter. The optical signal beam is then collimated by a lens at the corresponding transmitter output, and is deflected by a holographic grating element fabricated on the backplane. The deflected beam can propagate in free-space

(Figure 2-2) and be reflected back by a mirror, or it can propagate within the transparent backplane through multiple total internal reflections at its medium/air boundaries.

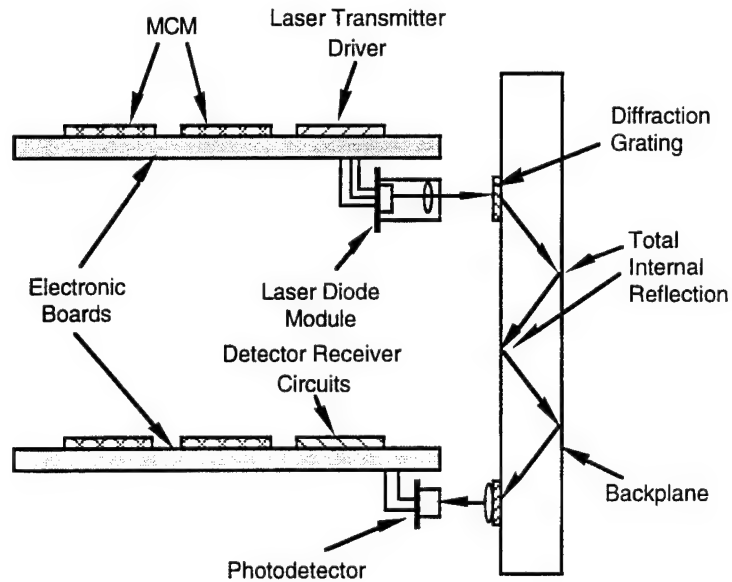


Figure 2-1
Backplane Substrate Optical Interconnects Using laser Transmitters

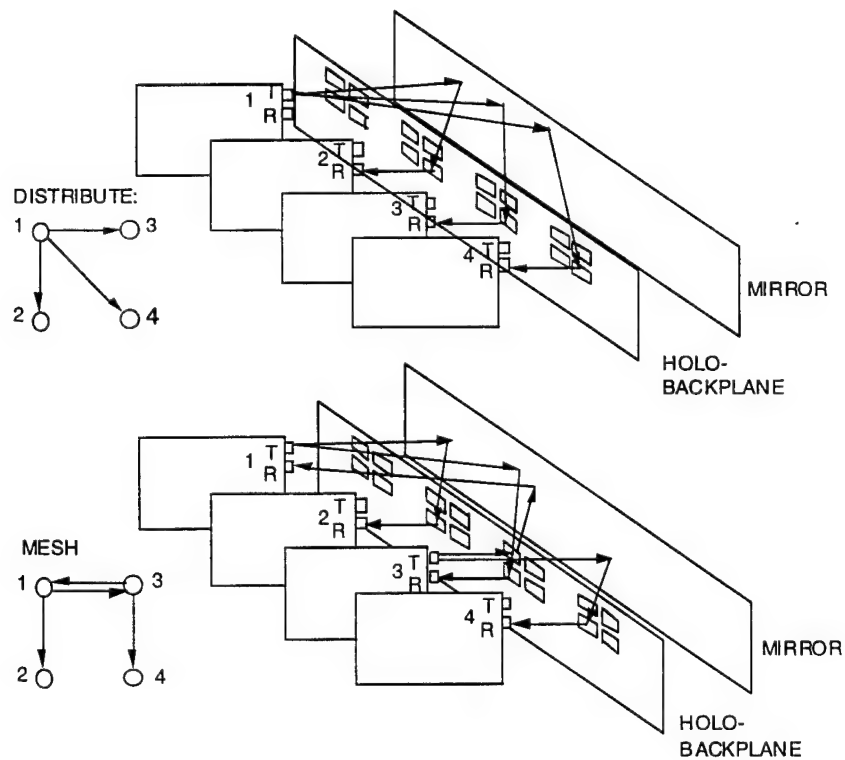


Figure 2-2
Holographic Optical Backplane Interconnects Using Reflection Mirrors

The second type of backplane beam propagation and interconnection, when used in wafer-scale circuit packaging, is known as substrate optical interconnection [42]. In this study, it is called backplane substrate interconnection. After the beam is reflected or guided to the receiving location, it is deflected by yet another holographic element to a detector or waveguide detector/receiver on a different circuit board, thus accomplishing the required board-to-board optical interconnection. Both interconnection schemes are attractive.

Direct modulation of laser diodes at the transmitter is a mature technology. Commercially available laser diodes or laser diode arrays can be modulated at GHz speeds. Electrical signals to be transmitted from electronic modules or chips are first converted into current-modulated signals to modulate the laser. Laser driving circuits are required for this transmitter configuration, as was shown in Figure 2-1. The advantage of this transmitter configuration is that packaging and optical alignment issues can be addressed on the engineering level. It thus represents a short term solution for optical board-to-board interconnects, and the scheme can well be implemented in a practical system. However, it suffers from a potential heat dissipation problem, and the laser diode transmitters should not be placed in the vicinity of electronic chips. This drawback limits its use in wafer-scale chip-to-chip interconnects, but does not hinder the design of board-to-board optical interconnects, since the transmitters can be placed near the edge of the circuit boards.

Waveguide modulator transmitters are a more advanced solution to the heat dissipation problem. As was depicted in Figure 1-1, the laser diode array at the edge of the board provides CW light to the channel waveguide arrays. Channel waveguide modulators are employed to convert the electrical signals from the chips to intensity-modulated optical signals via the electro-optic effect. Driving circuits are not required in this modulation configuration, since the modulation voltages of the modulators can be designed to match the electronic chip signal output levels. The primary advantage of the waveguide modulator approach is that it can achieve high waveguide packaging density (50 to 500 channels per cm) and be placed near the electronic chips. Thus, the metallic interconnect lengths between the modulator electrodes and electronic chips can be minimal. This is essential for high-speed operation. The channel waveguide modulator approach is also suitable for wafer scale chip-to-chip interconnects, as depicted in Figure 2-3. Channel waveguide and modulator arrays are fabricated on electro-optic substrates such as LiNbO_3 , and their use in multichip module packaging is implemented by wire bonding or flip-chip bonding on microcircuit carrier substrates.

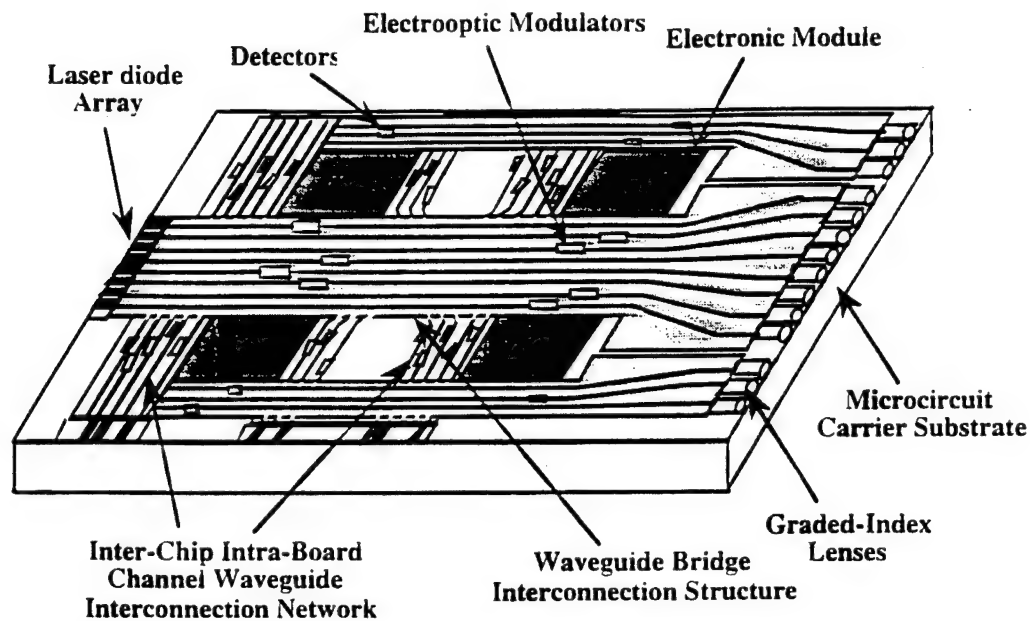


Figure 2-3
Wafer Scale Chip-to-Chip Optical Interconnects Using Channel Waveguide Arrays

Comparing these two different transmitter configurations, POC believes that both types of interconnects (Figures 1-1 and 2-1) are important. More research and development efforts should be focused on the waveguide-backplane-waveguide interconnect configuration (Figure 1-1) since it has advantages in high-speed operation, high channel packing density, low-cost batch fabrication, and rugged alignment, and it creates no heat-generation problems near electronic chips.

The Phase II research thus mainly focused on the waveguide interconnect approach shown in Figure 1-1; the laser transmitter approach in Figure 2-2 was demonstrated in Phase I with a holographic backplane. Laser transmitters were also addressed in Phase II, along with fiber ribbon packaging, which will be described later.

2.2 Waveguide-Backplane-Waveguide Optical Interconnect Structures

Since the waveguide-backplane-waveguide interconnects were the main focus of the proposed research, a more detailed discussion of their operation is necessary. As depicted

in Figure 1-1, the new board-to-board optical interconnects employ a channel waveguide/holographic-backplane/channel waveguide structure for optical signal routing. An array of channel waveguide optical interconnection buses with electro-optic modulators fabricated on a thin LiNbO_3 substrate layer is hybrid-packaged on common Si, GaAs, or other microcircuit carrier substrates. There are two types of optical data buses. One type, located on the center portion of the substrate (as shown in Figure 1-1), is a transmitting channel waveguide, while the type located on the outer portion of the substrate is the receiving channel. This arrangement can be reversed, with the receiving channels placed in the center portion of the substrate and the transmitting channels located on the outer portion. The primary reason for using LiNbO_3 is to take advantage of its large electro-optic coefficient for electro-optic modulation, its low-loss guided wave propagation ($-0.1 \sim -0.4$ dB/cm), and its relatively mature guided wave device fabrication technology. A good quality electro-optic modulator can be constructed on such a substrate to perform efficient electrical-to-optical signal conversion.

An array of separately fabricated laser diodes (shown in Figure 1-1) whose dimensions match with the channel waveguide optical buses can be hybrid-packaged on the same substrate, and optically aligned to facilitate optical butt coupling and provide constant light power for the transmitting channel waveguides. An alternate configuration uses a high-power laser diode and a fiber or waveguide fan-out device, as shown in Figures 2-4 and 2-5. This configuration allows distribution of high-power laser light to all channels, and has the advantages of: (a) one-step fiber/waveguide pigtail alignment; (b) no excess heat dissipation problem at the circuit board due to laser operation, since the laser is located far from the circuit board; and (c) easy replacement of damaged laser diodes with the use of fiber connectors.

An array of commercially available GRIN (graded index) lenses can be placed on the ends of the transmitting channels to couple optical signals from the channels for backplane interconnection. They can also be used to couple backplane beams to receiving channels. Collimated beam interconnections from one chip carrier board to the other can be achieved in the transparent backplane via a total internal reflection scheme.

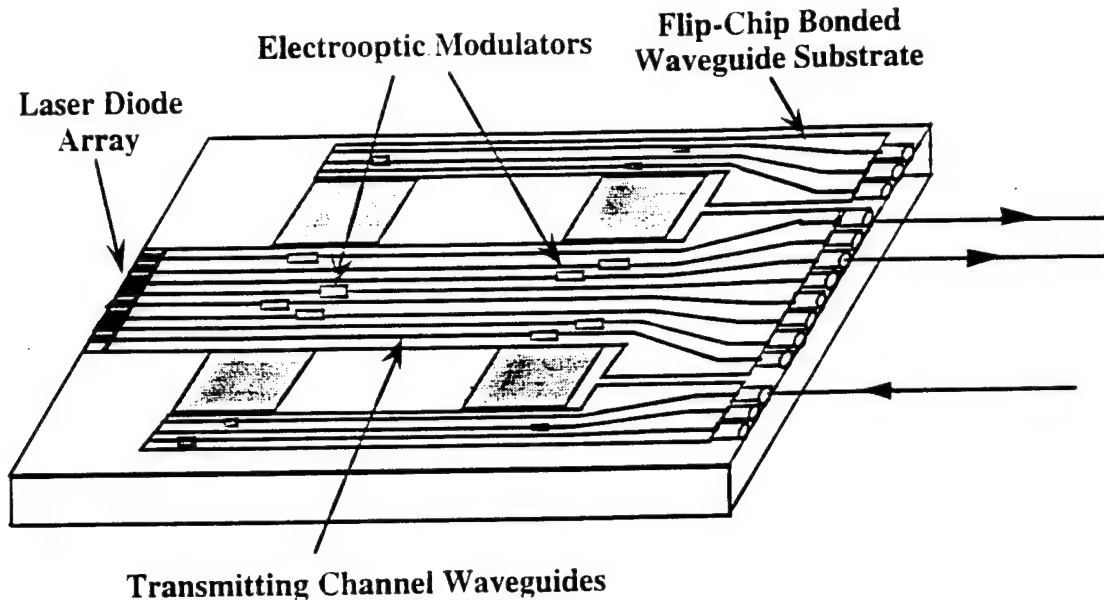


Figure 2-4
Input Coupling of a High Power Laser Diode to a Fiber Fanout and Channel Waveguide Array

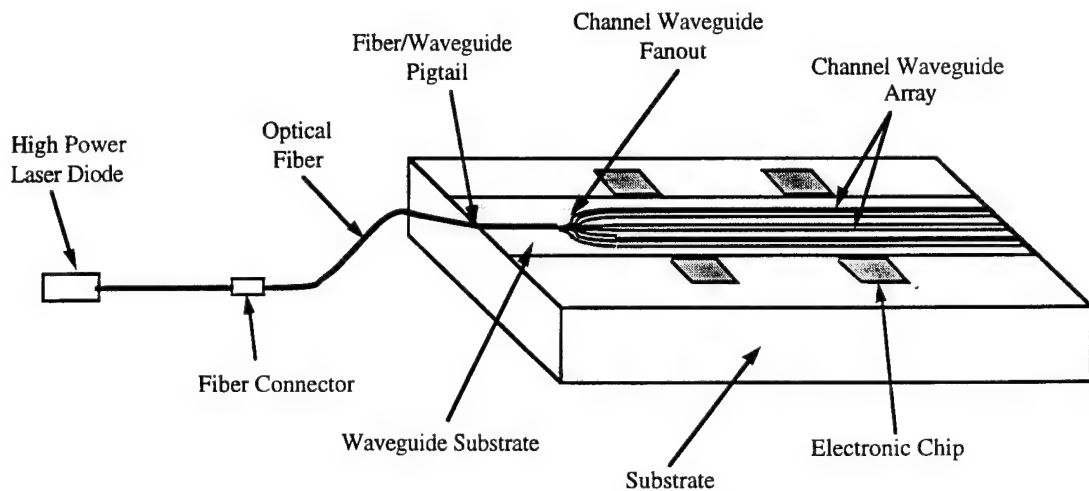


Figure 2-5
Input Coupling of a High-Power Laser Diode to Channel Waveguide Arrays

The use of conjugate pairs of holographic grating elements on the backplane can reduce the directional sensitivity of the backplane output beam to laser wavelength shifts caused by environmental effects and bias fluctuations. This issue will be addressed in more detail in a later section. The planarized backplane substrate interconnect can facilitate the formation of a variety of device components, including fan-outs [42,43], wavelength dispersive elements

[44], and even active devices on the common backplane, to provide a complete optical signal distribution system. The inherent advantage of backplane substrate interconnects is the reduction of alignment/space constraints often associated with bulk optics. Additionally, multiple conjugate holographic grating pairs can be constructed, and the interconnection pattern can be reconfigured through parallel backplane movement to activate different sets of interconnection holograms (see Figure 2-2). This capability not only allows different interconnect configurations for parallel and distributed processing (hypercube, mesh, etc.), but also allows them to be made compatible with such standard electrical buses as VME Bus and Futurebus. The holographic backplane can even interconnect multiple transmitters and/or receivers on a board to achieve truly flexible processing schemes, including different logic processing capabilities.

2.2.1 Channel Waveguide Arrays

In the preceding section, we described the overall picture of the proposed board-to-board optical interconnects. The channel waveguide is an important component in this technique. The choice of channel waveguide arrays is predicated on five basic requirements: (a) the channel waveguide orientation must satisfy the electro-optic modulator requirement for efficient beam intensity modulation; (b) the spacing between channels must allow the positioning of proper modulation electrodes; (c) the waveguides fabricated on any substrate and at any particular orientation must demonstrate low loss propagation for guided modes; (d) it must be possible for the channel waveguide end-face to be cut and polished with optical quality facets perpendicular to the channel waveguides; and (e) the waveguide mode pattern at the channel output should allow the diverging output radiated beam to be collimated by the graded index (GRIN) lens for backplane beam diffraction and propagation.

The use of an X-cut LiNbO_3 substrate can satisfy the efficient electro-optic modulation requirement. The typical channel waveguide orientation on this substrate is along the y-axis. The waveguide can be fabricated by either titanium indiffusion or proton exchange. Both fabrication techniques can result in low loss (from -0.1 to -0.4 dB/cm) optical waveguides. The LiNbO_3 substrate allows the channel end-faces to be cut and polished perpendicular to the channel waveguide. Thus, the design issues are reduced to the choice of modulator type, channel spacing, and waveguide mode profile.

The waveguide modulator can be any of the following types: Mach-Zehnder interferometer [45], directional coupler modulator [46], X-switch modulator [47], cut-off modulator [48], mode conversion modulator [49], Bragg grating diffraction modulator [50], guided-to-radiation coupling modulator [51-54], and the recently demonstrated electro-optic grating coupler modulator [55]. More details on waveguide modulators are given in the next section. For compact packaging and space saving considerations, a one-port-in and one-port-out straight channel configuration is preferred. A schematic of the straight channel waveguide array is shown in Figure 2-6. Channel spacing can be as small as 20 μm , since the typical electrode pad width is 15 to 30 μm . At a channel spacing of 20 μm , the channel waveguide packing density is 500 channels/cm.

The total number of channels that can be used for the optical interconnection is limited by the number of GRIN lenses that can be placed on one end of a circuit carrier board (see Figure 1-1). When 1 mm diameter GRIN lenses are used, a 3" wide circuit board can accommodate nearly 75 lenses; hence, the total number of channels that can be placed on the board is limited to 75. The number of channels the interconnect system can be increased if other circuit board edges are also used for board-to-board interconnect purposes. We note that when some channels are used for intra-board inter-chip optical interconnection, the packing density of these channels is not limited by the dimensional constraints of the GRIN lenses. In this case, high channel packing density is a significant plus to the interconnect systems.

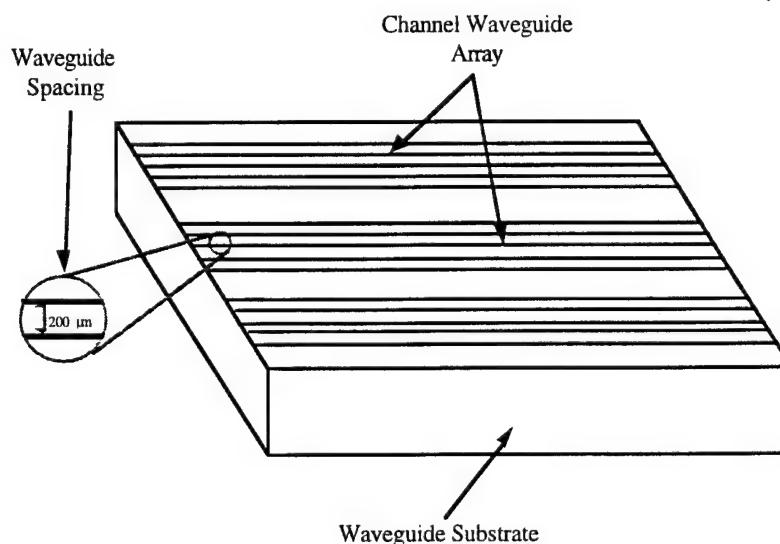


Figure 2-6
Schematic of Straight Channel Waveguide Arrays

2.2.2 Channel Waveguide Electro-Optic Modulators

Integrated electro-optic modulators have been studied for more than two decades. Electro-optic modulation methods can be divided into three groups: phase, polarization, and intensity modulation. Phase and polarization modulated signals eventually must be converted into intensity modulation for the modulated signals to be detectable by photodetectors. Hence, intensity modulation is desired for the optical interconnects. One of the most popular types of modulators is the directional coupler modulator [46]. Because of the overlap in the evanescent fields of two waveguides, light couples between adjacent channels; the coupling coefficient depends on waveguide parameters, wavelength, and inter-waveguide separation. With proper design and fabrication conditions, all of the light entering one waveguide can be coupled to that of the other, or can be uncoupled by the electro-optic tuning of the waveguide parameters. Another modulation scheme is the integrated optic version of the Mach-Zehnder interferometer [45]. This type of modulator employs the interference principle of coherent light traveling through different optical path lengths, which are tunable through modulator biases. Throughput intensity is modulated according to the phase difference of the two optical paths. There are seven other types of waveguide modulators: cutoff [48], phase [46], mode conversion [49], Bragg diffraction [50], X-switch [47], guided-to-radiation coupling [51-54], and electro-optic grating coupler modulators [55].

Each of the above intensity modulators has been demonstrated on insulating and semiconductor substrates, and some of them have also been demonstrated on electro-optic polymer waveguides [56]. All of them employ thin film dielectric waveguides as the fundamental building blocks. They also have a combination of properly designed electrode patterns. A high-frequency, wide-bandwidth electro-optic modulator (up to 20 GHz at $\lambda = 1.3 \mu\text{m}$) has been achieved [57] on GaAs.

From the optical interconnection point of view, the requirements for an electro-optic modulator are: (a) high speed and wide bandwidth (demonstrated on most channel waveguide modulators on LiNbO_3); (b) high packing density with one input port and one output port (which rules out the use of a directional coupler modulator, X-switch, or Bragg diffraction modulator); (c) high throughput optical intensity (which rules out the use of a cutoff modulator); and (d) small modulator length with direct intensity modulation (which

rules out the use of phase- and mode-conversion modulators). Thus, there remain only three types of electro-optic modulators that can potentially be used in the proposed optical interconnect system: the Mach-Zehnder interferometer, the guided-to-radiation coupling modulator, and the electro-optic grating coupler modulator.

The Mach-Zehnder interferometer modulator, shown in Figure 2-7, has been studied and is commercially available. It thus represents a mature waveguide modulator technology. (The guided-to-radiation coupling modulator and electro-optic grating coupler modulators are premature for the Phase II system demonstration.) However, most demonstrated Mach-Zehnder interferometer modulators have a device length of over 2 cm. A smaller device length of < 5 mm is possible, based on the operating principle of the device, but has yet to be demonstrated. In Phase II, we demonstrated a miniaturized Mach-Zehnder interferometer modulator and modulator arrays.

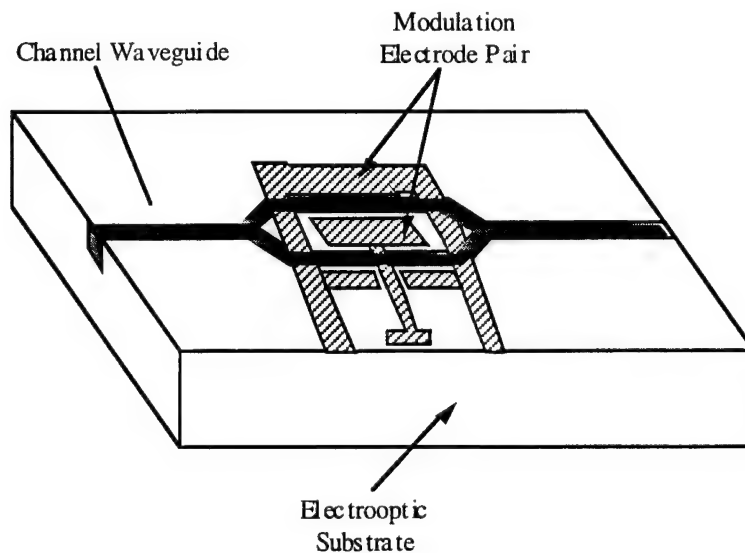


Figure 2-7
Waveguide Mach-Zehnder Interferometer Modulator. It is a well developed modulator technology and is employed in Phase II in a miniaturized version.

2.2.3 Channel Waveguide Modulator Arrays

The system requires waveguide modulator arrays. The modulator array outputs will be coupled to the optical backplane and delivered to the receiving board to accomplish the board-to-board optical interconnects. As mentioned above, optical waveguide modulators

are available from commercial vendors, among them Crystal Technology and United Technology Photonics. However, the available single modulator devices are too long, too costly, and not suitable for this Phase II application (\$5000 to \$9000 per modulator). Furthermore, there are no commercial modulator *arrays*. The goal was thus to produce waveguide modulator arrays of desired spacing, short modulator length (< 5 mm from y-junction to y-junction), and good modulator performance.

In order to provide application flexibility, two types of modulator arrays were investigated. The first type is the so-called parallel Mach-Zehnder modulator array, shown in Figure 2-8. This device has four single parallel waveguide Mach-Zehnder modulator units integrated in a single X-cut LiNbO_3 substrate. Taking into consideration the fact that aperture of most common GRIN lenses is 1.8 mm, the separation between the adjacent modulators was chosen as 2 mm. The second type is the so-called one-to-four fan-out Mach-Zehnder modulator array, shown in Figure 2-9. In this device architecture, four modulator units are integrated in parallel through a properly designed one-to-four channel waveguide fan-out structure. The separation between the adjacent modulators is chosen at either 125 mm or 250 mm, so that a suitable fiber optic ribbon cable can be readily attached. Details on device design are given in Section 3.1.1. The present design uses a lumped electrode structure, since the required data rate is only 1.5 Gb/s. When optimized, this type of electrode design should be able to transmit over 10 Gb/s.

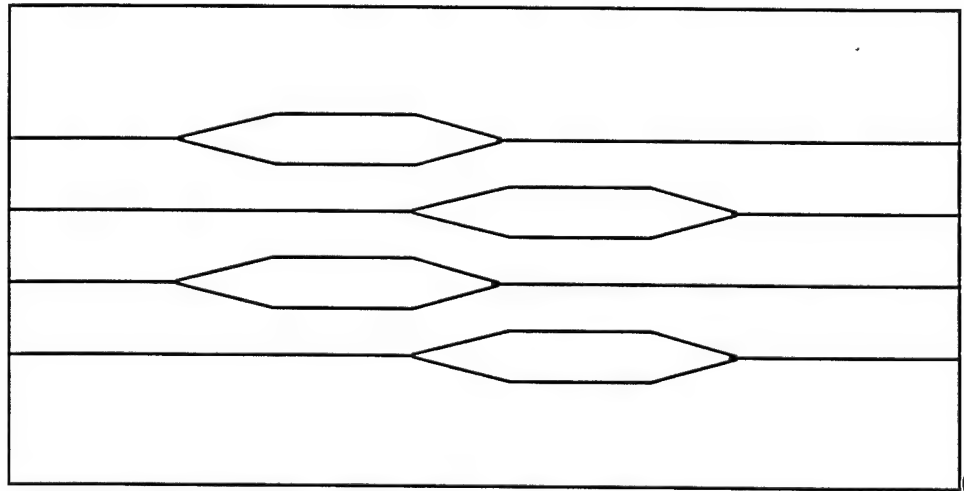


Figure 2-8
Schematic of a Parallel Mach-Zehnder Modulator Array

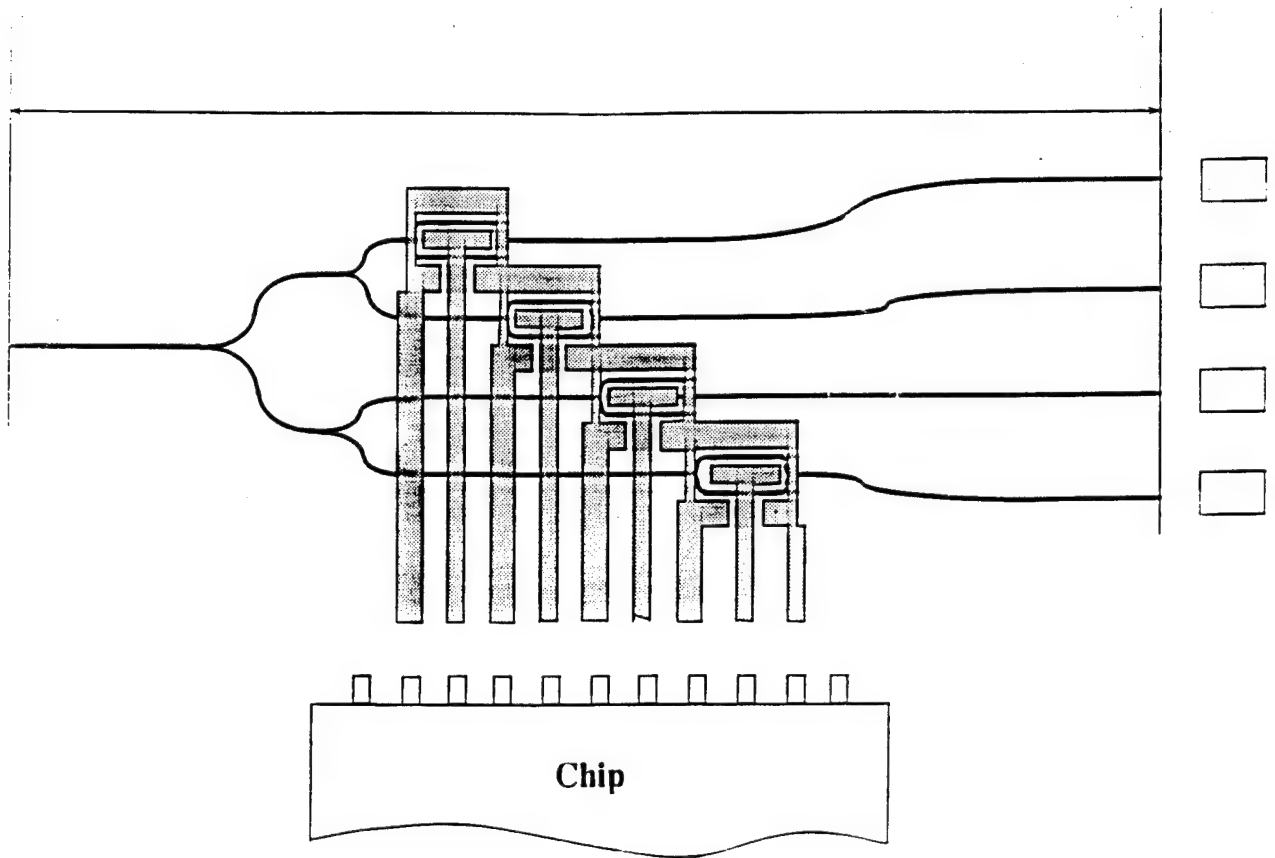


Figure 2-9
Schematic of a Modulator Array with One-to-Four Waveguide Fanout

2.2.4 Channel Waveguide Modes and Radiated Beam Collimation

Channel waveguide modes are determined by the channel waveguide width and depth, the channel waveguide index distribution profile, and the amount of index change caused by fabrication. For proton-exchanged channel waveguides, the maximum change in the extraordinary index is as large as 0.12. Hence, the channel waveguide can support optical modes with a very small exchanged channel depth. In this case, the side diffusion can be ignored, and the channel waveguide possesses nearly rectangular boundaries with uniform index distribution. This is sometimes called step index distribution. Under this condition, the channel waveguide mode can be calculated easily by the effective index method [58] or the Marcatilli's method [59].

Figure 2-10 shows a calculated guided single-mode field distribution. We note that to ensure good collimation of the channel radiated beam by the GRIN lens, singlemode distribution is required. As for the collimation or fiber pigtailling of a semiconductor laser, the radiated beam from the single-mode channel waveguide should demonstrate a near-elliptical far-field beam profile due to the different width and depth in its heterostructure. The small dimensions of the single-mode channel, 4 to 5 μm width and about 0.26 μm depth, as compared to the lens diameter of 1800 μm , guarantee excellent collimation since the channel output acts like a point source. In a practical case, the depth will be increased and the channel refractive index will be reduced by thermal annealing. The overall channel waveguide size is less than 9 μm . The channel output is still like a point source.

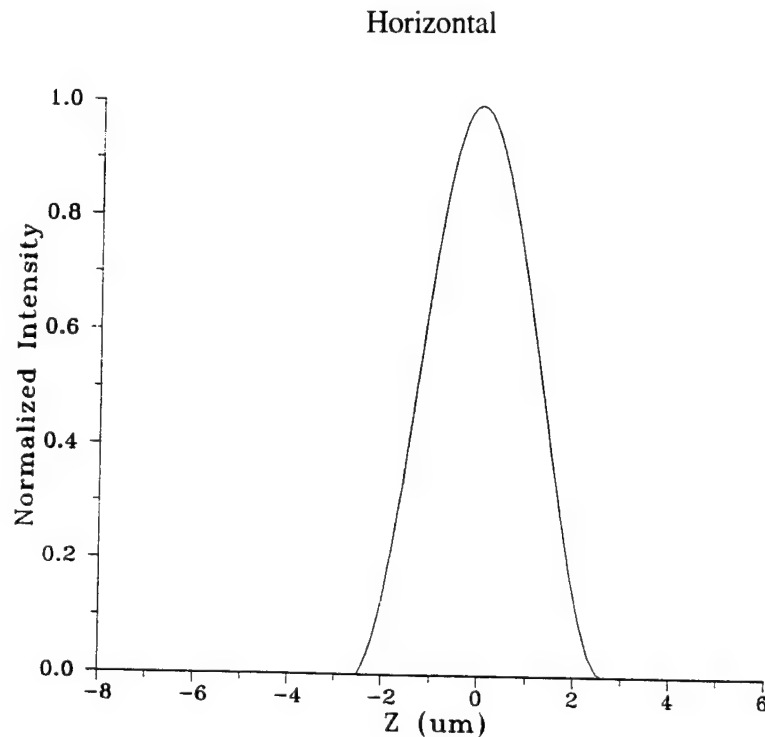


Figure 2-10
Channel Waveguide Mode Profiles
(continued)

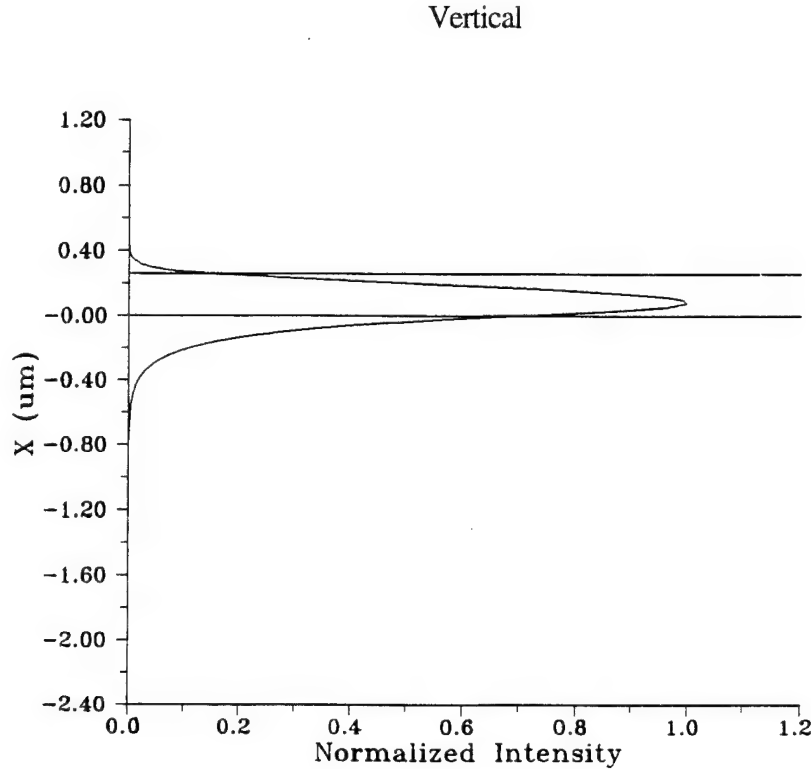


Figure 2-10
Channel Waveguide Mode Profiles

To achieve excellent energy efficiency for the channel radiated beam collimation, the numerical aperture of the channel waveguide must be smaller than that of the GRIN lens. To justify such a statement, we must first understand the definition of numerical aperture for both channel waveguides and GRIN lenses.

For channel waveguides, the channel mode radiated into free-space has diverging angles. Due to the asymmetry in channel width and channel depth, the diverging angles in the horizontal and vertical directions are not the same. Based on the calculations shown in Fig. 2-10 above, the estimated diverging angle for the vertical direction is

$$2\theta_{\perp} = 84^{\circ} \quad (2-1)$$

while the diverging angle for the horizontal direction is

$$2\theta_{//} = 8.86^{\circ} \quad (2-2)$$

Since the numerical aperture (N.A.) is defined as the index n of the radiation medium multiplied by the sinusoidal function of the half of the diverging angle, $\sin \theta$, the numerical aperture for the channel waveguide is

$$N.A._{\perp} = 0.67 \quad (2-3)$$

$$N.A._{\parallel} = 0.077 \quad (2-4)$$

The vertical numerical aperture is relatively large. It can be experimentally reduced to below 0.5 by a thermal annealing process. In GRIN lenses, the material refractive index varies parabolically as a function of radius, as given by

$$n_r = n_o \left(1 - \frac{A}{2} r^2 \right) \quad (2-5)$$

where n_r is the refractive index at a distance r from the optical axis, n_o is the design index on the optical axis, and A is a positive constant depending on fabrication conditions. As a result of the parabolic index variation, a ray incident on the front end of the lens will propagate in a sinusoidal path inside the lens. Based on its unique property of optical beam propagation, the GRIN lens can be used for imaging or beam collimation. When it is used for collimation, the length of the GRIN lens should depend on the location of the point source (see Figure 2-11) as well as on the optical wavelength. For compact packaging, the GRIN lens should be in contact with the channel waveguide end-face. A 0.25P type lens should be chosen. For ease of handling, to allow proper adjustment of beam collimation, a 0.23P or shorter lens should be used. The numerical aperture of the GRIN lens depends on fabrication and typically ranges between 0.37 and 0.60. These are provided by NSG America, Inc. and Melles Griot, Inc. For channel radiated beam collimation, the chosen GRIN lens can easily satisfy the design requirement for maximum energy collection efficiency.

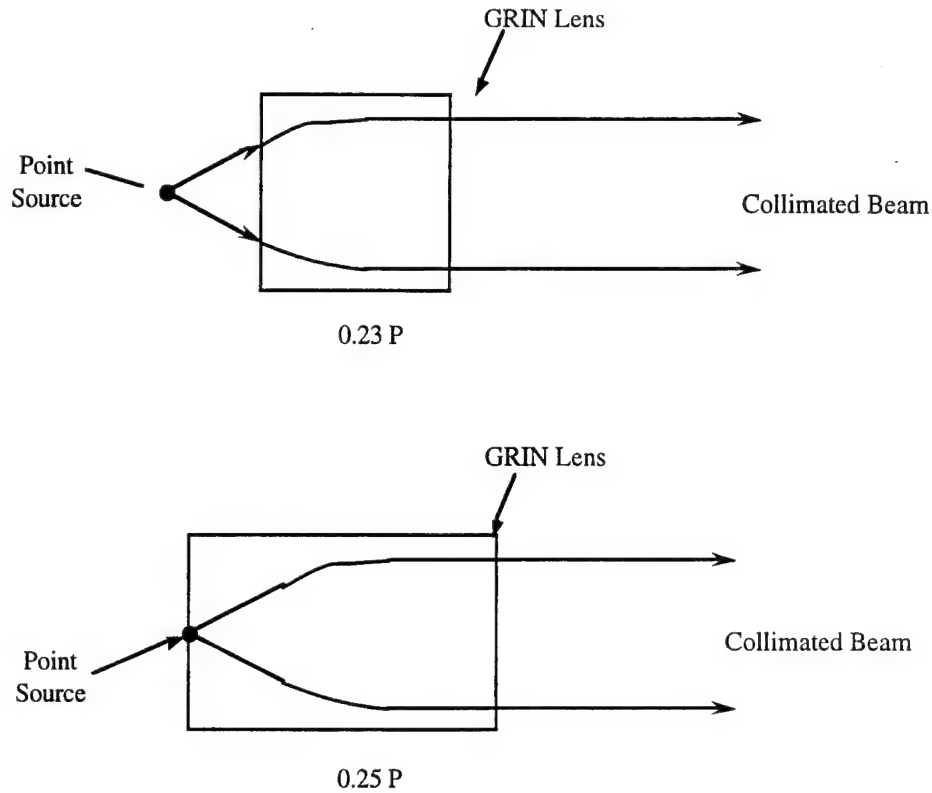


Figure 2-11
Length of a GRIN Lens and its Effect on Point Source Location for Collimation

It is anticipated that a collimated beam can be similarly focused back into the channel waveguide. This is the basis for coupling the backplane beam to the receiving channel with a GRIN lens.

2.2.5 Holographic Backplane and Chromatic Sensitivity

The architecture of the diffraction hologram for the backplane optical interconnect was shown in Figure 1-1. This type of hologram is sometimes referred to as a total internal reflection (TIR) hologram, or Bragg diffraction hologram. It has slanted fringes, and it diffracts the incoming collimated optical signal into the transparent substrate medium. In the backplane substrate, the diffracted optical beam propagates and is kept between the two medium/air boundaries through total internal reflection. When the beam is guided to the receiving location, it is diffracted out of the backplane substrate by another conjugate

hologram, also with slanted holographic grating fringes (Figure 2-12). This establishes the required backplane substrate interconnection.

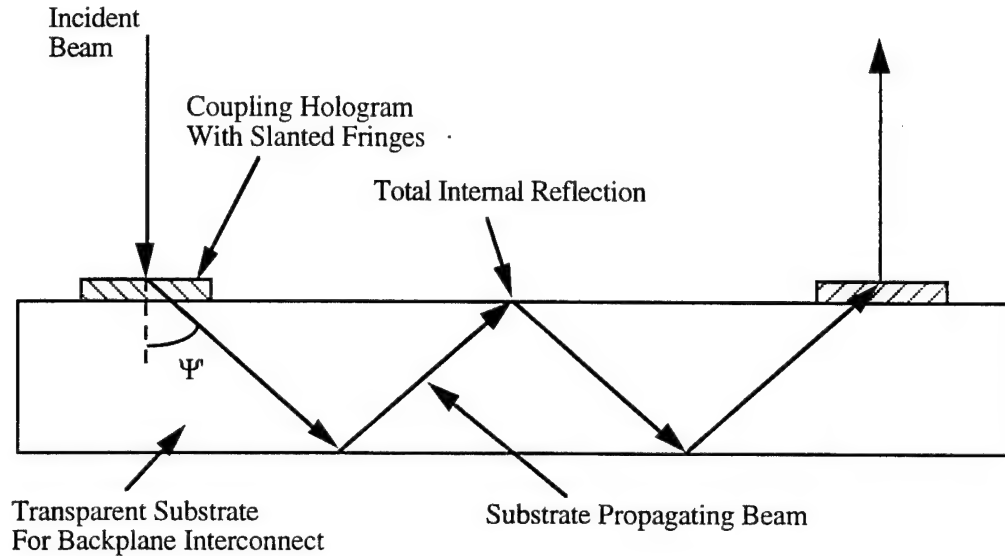


Figure 2-12
Backplane Substrate Interconnect with Slanted Input and Output Coupling Holograms

This type of holographic grating is usually fabricated by the two-beam interference method. To form the slanted grating coupler which converts the vertical incident optical wave to a total internal reflection mode with bouncing angle Ψ' (between surface normal and diffracted wave propagation direction, see Figure 2-12), the two incident angles of the recording beams (Figure 2-13) can be expressed as

$$\theta_1 = \sin^{-1} \left(\frac{n_f}{n_{re}} \sin \delta' \right) \quad (2-6)$$

$$\theta_2 = \sin^{-1} \left(\frac{n_t}{n_{re}} \sin(\Psi' - \delta') \right) \quad (2-7)$$

where n is the index of refraction of the holographic emulsion. In this case, dichromated gelatin (DCG) is used as the recording film, and $n \sim 1.53$. n_{re} is the refractive index above the film during the recording process ($n_{re} = 1$ for air). d is related to the bouncing angle Ψ' and the recording and reconstruction wavelengths, λ_{re} and λ_c , by

$$\delta' = \frac{\Psi'}{2} - \sin^{-1} \left(\frac{\lambda_{re}}{\lambda_c} \sin \left(\frac{\Psi'}{2} \right) \right) \quad (2-8)$$

To increase the bouncing angle Ψ' for a longer beam propagation distance in each bounce, we can either decrease the ratio of λ_{re}/λ_c by changing the recording and reconstructing wavelengths, or increase n_{re} by putting a high-index prism right on top of the holographic emulsion during the recording process.

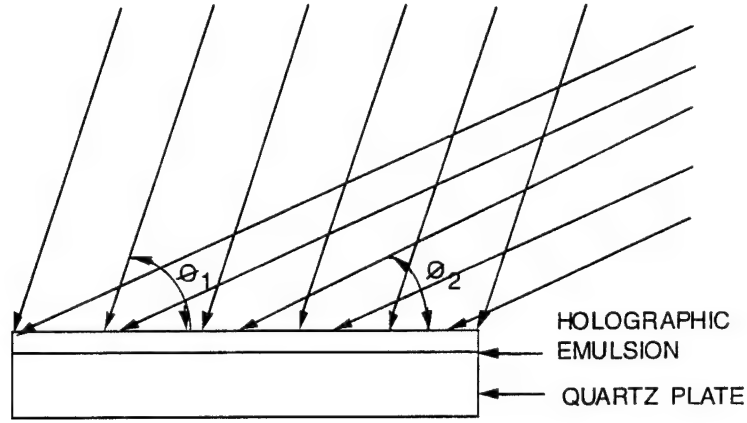


Figure 2-13
Definition of Recording Angles for Slanted Holographic Gratings

The above two-grating optical backplane is chromatic-sensitive to changing wavelength in the area of beam movement and chromatic insensitive in the area of output beam direction. To examine chromatic sensitivity, we start with the holographic Bragg diffraction, as schematically shown in Figure 2-14. The well-known Bragg grating dispersion equation is written in general form as

$$\sin \alpha = \sin \theta \pm \frac{\lambda}{n\Lambda} \sin \phi \quad (2-9)$$

where \pm is used when $\phi - \theta \neq 90^\circ$, λ is the free-space laser wavelength, n is the refractive index of the bulk holographic material, L is the grating fringe spacing, and θ , α , and ϕ are the incident, diffracted, and grating slant angles, respectively, as shown in Figure 2-14. All of these angles are in the medium of the diffraction grating, and Fresnel equations can

be used to translate these angles to those outside of the emulsion area. Eq. (2-9) can account for both transmission and reflection holograms.

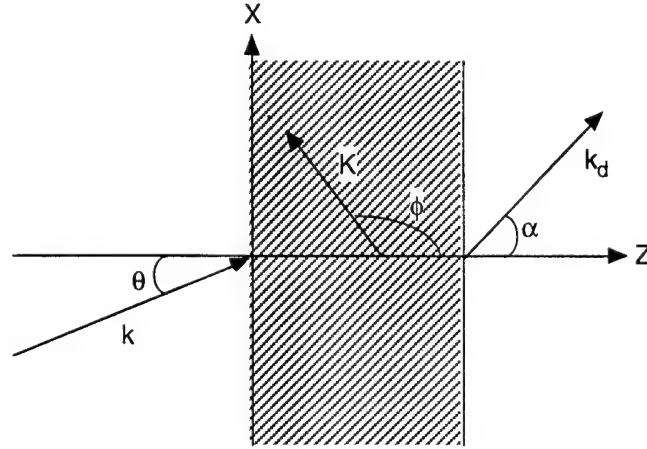


Figure 2-14
Schematic of a Holographic Bragg Diffraction

Taking the differentiation on Eq. (2-9), we have

$$\Delta\alpha \cos\alpha = \Delta\theta \cos\theta \pm \frac{\Delta\lambda}{n\Lambda} \sin\phi \mp \frac{\lambda}{n^2\Lambda} \sin\phi \frac{dn}{d\lambda} \Delta\lambda \quad (2-10)$$

Here, the third term on the right-hand side of Eq. (2-10) (which is due to material dispersion), can be ignored since its ratio to the second term is typically less than 2% for soda-lime glass, BK7, DCG, and a variety of other optical materials near the application wavelength with 80 nm wavelength variations. Using Eq. (2-9), Eq. (2-10) becomes

$$\Delta\alpha \cos\alpha = \Delta\theta \cos\theta + \frac{\Delta\lambda}{n\Lambda} (\sin\alpha - \sin\theta) \quad (2-11)$$

This equation can be used to describe the sensitivity of the diffraction angle α on incident angle misalignment $\Delta\theta$ and incident wavelength variation $\Delta\lambda$. $\Delta\theta$ includes both external beam alignment error and material dispersion-related misalignment. Owing to the interest in chromatic sensitivity, we consider only material dispersion-related misalignment at boundary incidence. Hence, $\Delta\theta$ can be expressed as

$$\Delta\alpha \cos\alpha = \Delta\theta = -\frac{\tan\theta}{n(\lambda)} \frac{dn}{d\lambda} \Delta\lambda \quad (2-12)$$

derived from the Fresnel equation

$$\sin\theta_i = n(\lambda)\sin\theta \quad (2-13)$$

where θ_i is the incident angle in free-space. Under normal incidence, $\theta = \theta_i = 0^\circ$, $\Delta\theta = 0^\circ$, and the material dispersion is again ignored. The chromatic sensitivity of the diffraction is now given by

$$\Delta\alpha = \frac{\Delta\lambda}{\lambda} \tan\alpha \quad (2-14)$$

For a given laser wavelength shift, the diffraction angle is sensitive to chromatic variation under large absolute values of α in $(-90^\circ, 90^\circ)$ and small free-space wavelength. For substrate coupling applications, as shown in Figure 2-15, the small α can cause diffracted beam position shift Δl in the substrate by

$$\Delta l = \left| 1 - \frac{\tan(\alpha + \Delta\alpha)}{\tan\alpha} \right| l \quad (2-15)$$

where l is the substrate beam planar propagation distance. Small laser wavelength shifts can produce significant optical spot shifts at the output coupling hologram. For example, under a normal and collimated incidence on an optical backplane, a 1 nm laser wavelength shift at 1300 nm center wavelength can change the diffracted beam angle in the backplane substrate by as much as 0.0763° near 60° . This can translate to about a $246.7 \mu\text{m}$ spatial beam spot shift at the output coupling hologram, after an 80 mm planar propagation in the backplane substrate. Increasing $\Delta\lambda$, l and angle α will further increase the spot shift values, possibly to several mm.

With the help of a holographic grating pair, as mentioned above, normal incidence will result in normal beam output at the output holographic coupler. To focus the backplane output beam for end-fire coupling to a channel waveguide, it is necessary to have a high numerical aperture lens and wide beam width, before focusing. For example, to generate a focused Gaussian beam spot of $5 \mu\text{m}$ width, from a Gaussian beam of 1 mm width, the

calculated focusing distance in free-space is about 5 mm. A spatial beam shift of $246.7 \mu\text{m}$ to 1 mm can result in focusing beam angles of $\sim 3^\circ$ to 11.3° , which may jeopardize the waveguide coupling and thus affect the performance of the proposed holographic backplane. Therefore, achromatic couplers that can preserve the normal output coupling angle and eliminate the spatial spot shift at the output coupling hologram are required for holographic backplane applications.

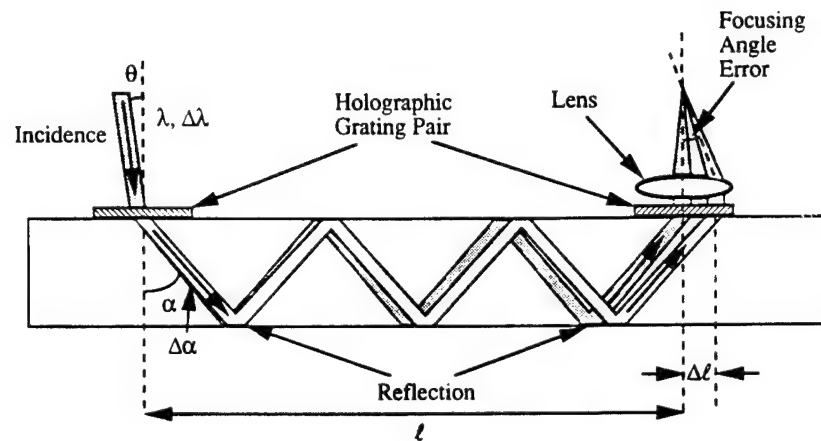


Figure 2-15
Wavelength Variation Causes Substrate Beam Spot Shift at the Output Coupling Hologram in a Two-Grating Structure. The beam spot position shift can be hundreds of μm , or even several mm, depending on the planar propagation distance l and angle α .

2.2.6 Design of Achromatic Holographic Grating Couplers

From the above analysis, it is apparent that the dispersion of the holographic gratings can cause significant substrate beam shifts. A two-grating system is not suitable for spatial shift compensation because the second grating has no effect at all on the shift. Because of this, at least a three-grating system is required. Figure 2-16 shows the three-grating system, all on the backplane surface, in order to provide stable output diffraction angle γ and output beam position. Three local coordinate systems, at corresponding gratings, are used to define the beam incidence and diffraction angles.

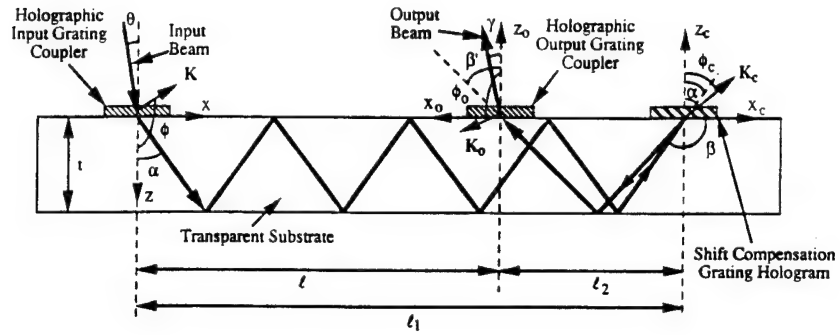


Figure 2-16

Three-grating system for backplane substrate interconnects, providing stable output diffraction angle γ and output beam position over the entire laser diode wavelength shift ranges

The dispersion relationships for the shift compensation grating and the output coupling grating are

$$\Delta\beta \cos \beta = \Delta\alpha \cos \alpha + \frac{\Delta\lambda}{\lambda} (\sin \beta - \sin \alpha) \quad (2-16)$$

and

$$\Delta\gamma \cos \gamma = \Delta\beta' \cos \beta' + \frac{\Delta\lambda}{\lambda} (\sin \gamma - \sin \beta') \quad (2-17)$$

respectively, where β is in the third quarter and $\beta' = \beta - 180^\circ$ is in the first quadrant of their corresponding coordinates. From Eqs. (2-16) and (2-17), a simple derivation results

$$\Delta\beta = \frac{\cos \alpha}{\cos \beta} \Delta\alpha + \frac{\Delta\lambda}{\lambda} \frac{\sin \beta - \sin \alpha}{\cos \beta} \quad (2-18)$$

$$\Delta\gamma = \frac{\cos \beta'}{\cos \gamma} \Delta\beta' + \frac{\Delta\lambda}{\lambda} \frac{\sin \gamma - \sin \beta'}{\cos \gamma} \quad (2-19)$$

When the output coupling angle is designed at $\gamma = -\theta$, the holographic backplane will be insensitive to laser wavelength variations despite the output grating's difference from that

of the aforementioned grating pair structure. Under normal incidence, with $\Delta\theta = 0^\circ$, the achromatic output coupling requires $\gamma = 0^\circ$; i.e., normal output coupling.

The spatial location of the beam spot at the output coupling hologram is calculated by the expression

$$l = l_1 - l_2 = 2m_1t \tan \alpha - 2m_2t \tan \beta \quad (2-20)$$

where t is the backplane substrate thickness and m_1 and m_2 are the numbers of the propagation bounces from the input grating to the shift compensation grating, and from the shift compensation grating to the output grating, respectively. Both l_1 and l_2 are positive in value for the designated angles shown in Figure 2-16. The physical spot shift in this case can be written as

$$\begin{aligned} \Delta l &= 2m_1t \frac{\Delta\alpha}{\cos^2 \alpha} - 2m_2t \frac{\Delta\beta}{\cos^2 \beta} \\ &= \left(2m_1t \frac{\sin \alpha - \sin \theta}{\cos^3 \alpha} - 2m_2t \frac{\sin \beta - \sin \alpha}{\cos^3 \beta} \right) \frac{\Delta\lambda}{\lambda} \\ &\quad + \left(2m_1t \frac{1}{\cos^3 \alpha} - 2m_2t \frac{1}{\cos^3 \beta} \right) \cos \theta \Delta\theta \end{aligned} \quad (2-21)$$

Under small incident angles, the effect of material dispersion can be neglected. Thus, $\Delta\theta \approx 0^\circ$. The spatial spot shift can be compensated by finding β and β' that satisfies

$$m_1 \frac{\sin \alpha - \sin \theta}{\cos^3 \alpha} = m_2 \frac{\sin \beta - \sin \theta}{\cos^3 \beta} = m_2 \frac{\sin \beta' + \sin \theta}{\cos^3 \beta'} \quad (2-22)$$

and makes Eq. (2-21) equal to zero. For normal incidence, $\theta = 0^\circ$, Eq. (2-22) simplifies to

$$m_1 \frac{\sin \alpha}{\cos^3 \alpha} = m_2 \frac{\sin \beta}{\cos^3 \beta} = m_2 \frac{\sin \beta'}{\cos^3 \beta'} \quad (2-23)$$

Since both sides of Eqs. (2-22) and (2-23) are monotonic increasing functions with respect to angles within the angular range of interest, single value solutions for β and β' can always be found for $m_1 \neq m_2$.

Results and Discussion

As can be seen from Eq. (2-23), angle β' depends only on m_1 , m_2 , and angle α . Since the ratio g of the two integers m_1 and m_2 ($g = m_2/m_1$) is a variable set, the relationship between β' and α for $m_1 > m_2$ is calculated and plotted in Figure 2-17 for a normal incidence case. In this case, we allow α to be less than the total internal reflection angle, to account for applications that use reflection coatings on both the top and bottom substrate surfaces. As is seen in Figure 2-17, a single value solution for β' is found, and β' is always larger than α for $m_1 > m_2$ as predicted from Eq. (2-23). The relationship between β' and α is obviously nonlinear for small g and α , while at larger α angles, such as $\alpha > 50^\circ$ (which is found for the total internal reflection condition in a soda-lime glass substrate with glass/air boundaries), the relationship approaches linearity, with slopes and axial intercepts which depend on the value of g . By extending the curves, all curves should eventually intercept at the origin and at the point of $\alpha = \beta' = 90^\circ$. Due to the symmetry in expression on both sides of Eq. (2-23), for $m_1 < m_2$, the β' and a relationship can be found (see Figure 2-17) by simply switching the coordinate axes and setting g equal to m_1/m_2 .

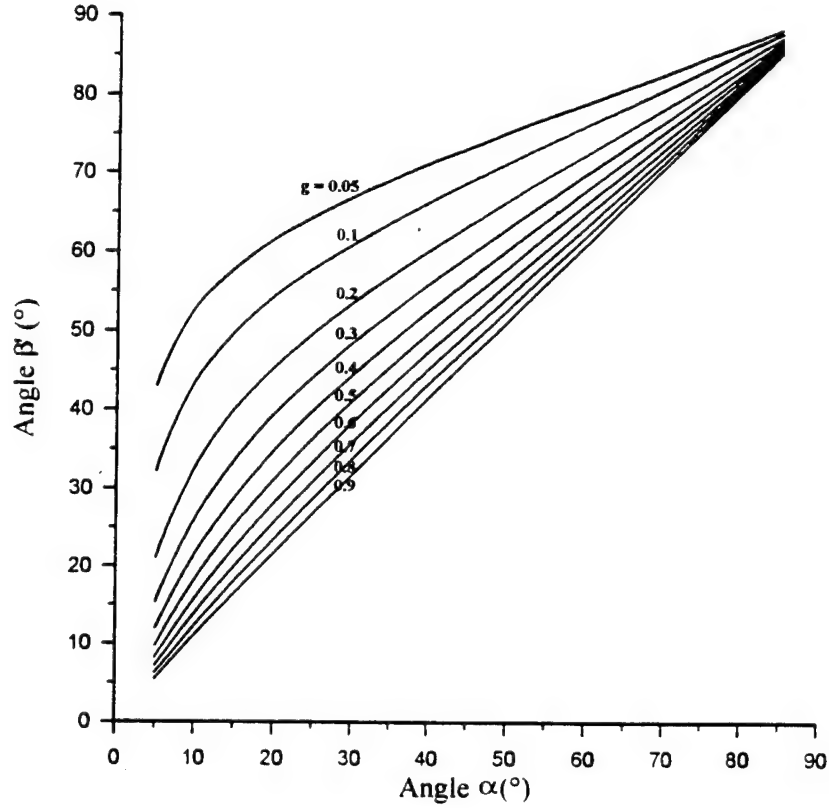


Figure 2-17
Relationship Between angle β' and Angle α for Different Ratios $g = m_2/m_1$ Satisfying the Achromatic Coupling Condition

In principle, any combination of m_1 , m_2 , α , and β' that satisfy Eq. (2-23) can provide a stable optical beam spot at the output coupling hologram. However, in practical applications, the total beam propagation length in the substrate must be minimized under a given planar propagation length l , in order to reduce substrate propagation and scattering losses. In other words, the shift compensation grating should be placed as close to the output grating as possible, for a given l . This can be achieved by minimizing f of Eq. (2-24) under the conditions of Eq. (2-23).

$$f = \frac{l_2}{l} = \frac{m_2 \tan \beta'}{m_1 \tan \alpha - m_2 \tan \beta'} \quad (2-24)$$

Figure 2-18 shows the calculated f numbers for different g and α values. f decreases with decreasing g and decreases with increasing α , at small α . For a large α angle, the relatively flat curve indicates that the α dependence is weak, especially for $\alpha > 70^\circ$. Therefore, for a large angle α , α should be determined by other design requirements, such as the achromatic wavelength range, which is discussed later. Additionally, holographic coupler designs for easier hologram recording and better energy efficiency are further design criteria. Although l and l_2 are not physical propagation lengths in the substrate, and f cannot account for possible angular dependent surface scattering losses, minimizing f should, in general, provide reasonable guidelines for selecting the ratio g .

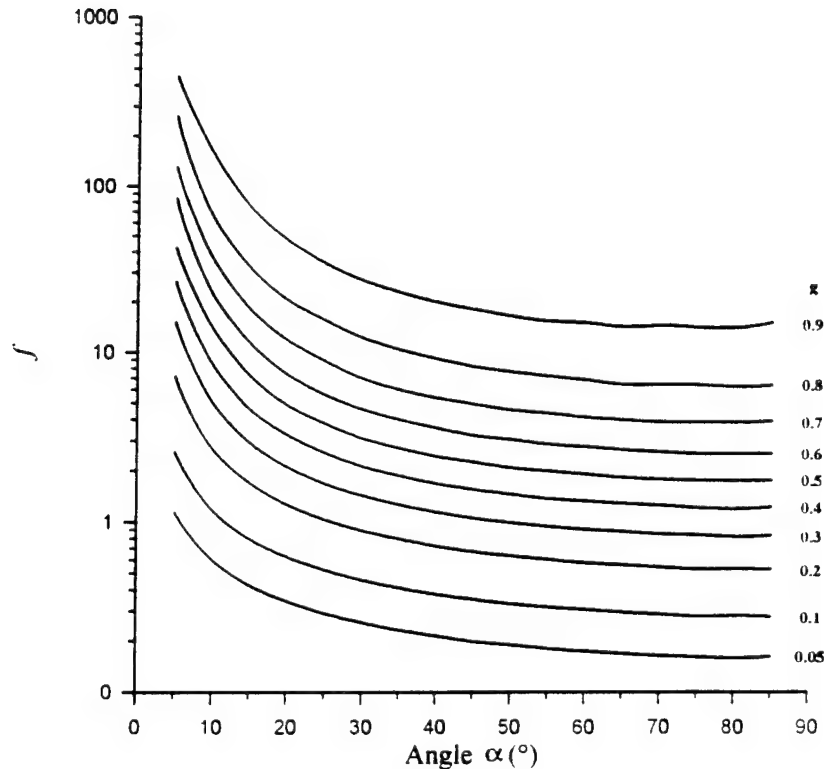


Figure 2-18
The Ratio f as a Function of Angle α Under Different g Values. Minimizing f is important for reducing total substrate beam propagation length and thus propagation and scattering losses.

To calculate the width of the achromatic wavelength range, we have

$$\frac{d\alpha}{d\lambda} \cos \alpha = \frac{d\theta}{d\lambda} \cos \theta \pm \frac{\sin \phi}{n\Lambda} \quad (2-25)$$

$$\frac{d\beta}{d\lambda} \cos \beta = \frac{d\alpha}{d\lambda} \cos \alpha \pm \frac{\sin \phi_c}{n\Lambda_c} \quad (2-26)$$

$$\frac{d\gamma}{d\lambda} \cos \gamma = \frac{d\beta'}{d\lambda} \cos \beta' \pm \frac{\sin \phi_o}{n\Lambda_o} \quad (2-27)$$

Likewise, the $dn/d\lambda$ term is again ignored. Knowing that

$$\cos \beta' = -\cos \beta \text{ and } \frac{d\beta'}{d\lambda} = \frac{d\beta}{d\lambda} \quad (2-28)$$

we can thus obtain the second derivative

$$\frac{d^2\gamma}{d\lambda^2} = \tan \gamma \left(\frac{d\gamma}{d\lambda} \right)^2 + \frac{\sin \theta}{\cos \lambda} \left(\frac{d\theta}{d\lambda} \right)^2 - \frac{\cos \theta}{\cos \gamma} \frac{d^2\theta}{d\lambda^2} \quad (2-29)$$

The first term on the right-hand side of Eq. (2-29) equals zero, due to the achromatic coupling condition, and the second and third terms, depending on the material dispersion relationship, are also zero due to normal incidence or are negligible for small angles of incidence. Therefore, the achromatic wavelength range for angle γ , defined by ^[10]

$$R_{\lambda,\gamma} \approx 2 \left(\frac{2\Delta\gamma_{tol}}{\left| \frac{d^2\gamma}{d\lambda^2} \right|} \right)^{1/2} \quad (2-30)$$

will mathematically approach infinity. Here, the $\Delta\gamma_{tol}$ is the allowed output coupling angular tolerance which can assume a finite value of 0.005° for $0.5 \mu\text{m}$ focused spot shift at the waveguide. This implies that achromatic coupling for angle θ has at least an 80 nm wide wavelength range, which is set by the condition used to ignore the material dispersion, and thereafter similar equations. Furthermore, the achromatic coupling is also limited by the Bragg diffraction condition for the input grating, and similar forms for other

gratings, which require real solutions for angles. This limitation can be determined from the wavelength selectivity curves of the Bragg diffractions. Our experiments on a slanted Bragg transmission hologram indicated that the wavelength selectivity bandwidth is about 54 nm under normal incidence, with a 50° diffraction angle, and a 12 μm holographic emulsion thickness. For a slanted reflection hologram, the wavelength selectivity bandwidth can be about 60 nm for an emulsion thickness of again 12 μm. These selectivity bandwidths are much larger than laser diode wavelength shift ranges which are typically less than 7 nm for 30°C temperature variations.

The other concern for achromatic wavelength ranges is on the beam spot shift. We may write the Δl equation by considering Taylor series expansion

$$\Delta l = \frac{dl}{d\lambda} \Delta\lambda + \frac{d^2l}{d\lambda^2} \frac{\Delta\lambda^2}{2!} + O[\Delta\lambda^3] \quad (2-31)$$

The first-order term on the right-hand side of Eq. (2-31) equals zero under the achromatic coupling condition of Eqs. (2-22) and (2-23). Keeping the second-order term, we therefore obtain the equation for the achromatic wavelength range for spot shifts

$$R_{\lambda,1} \approx 2 \left(\frac{2\Delta\gamma_{tol}}{\left| \frac{d^2l}{d\lambda^2} \right|} \right)^{1/2} \quad (2-32)$$

In Eq. (2-32), we have double the value due to focusing angle error symmetry in both positive and negative angular directions. Δl_{tol} is the spot shift tolerance allowed by the waveguide input coupling. Assuming the maximum allowed focusing angle error is 3°, for a focusing distance of 5 mm, the Δl_{tol} is therefore 262 μm, as calculated from the geometrical relationship of Figure 2-15. The second derivative in Eq. (2-32) can be obtained from Eq. (2-21). Under the condition of normal incidence, which eliminates θ and its derivatives, we have

$$\frac{d^2l}{d\lambda^2} = 6m_1t \frac{\sin\alpha}{\cos^3\alpha} \frac{\tan^2\alpha}{\lambda^2} - 6m_2t \frac{\sin\beta}{\cos^3\beta} \frac{\tan^2\beta}{\lambda^2} \quad (2-33)$$

Substituting Eq. (2-33) into Eq. (2-32) using Eqs. (2-23) and (2-24), we obtain

$$R_{\lambda,l} = 2 \left(\frac{2\Delta l_{\text{tol}} \lambda^2 \cos^2 \beta}{3fl |\tan^2 \alpha - \tan^2 \beta|} \right) \quad (2-34)$$

Here, $R_{\lambda,l}$ is inversely proportional to the square root of f and l . Minimizing f , and using a short distance l , can reduce total propagation distance in the substrate and, therefore, widen the achromatic wavelength range. Figure 2-19 shows the calculated achromatic wavelength range for α between 5° and 85° at $\gamma = 0.05$. A large achromatic wavelength range occurs at small angle α . Decreasing $R_{\lambda,l}$ with increasing α can be explained by the $\cos \beta$ term in Eq. (2-34), since $\beta = 180^\circ + \beta'$ increases with α , as shown in Figure 2-17. $R_{\lambda,l}$ approaches zero as ψ approaches 90° , while $R_{\lambda,\gamma}$ approaches zero. In the given α range in Figure 2-19, $R_{\lambda,l}$ is smaller than $R_{\lambda,\gamma}$, which assumes the value of 80 nm mentioned earlier, and is also smaller than the wavelength selectivity bandwidths, calculated based on the Bragg diffraction theory [7,8], at typical emulsion thicknesses of less than 25 μm . Therefore, $R_{\lambda,l}$ can be considered as the achromatic wavelength range of the three-grating system. For laser diode wavelength shifts of less than 7 nm, we should choose α to be less than or equal to 60° in order to provide chromatic compensations over the entire laser diode wavelength shift ranges. For a given set of substrate parameters; i.e., the board-to-board distance l , substrate thickness t , and integers m_1 and m_2 , exact α values can be determined from Eq. (2-20) with Eq. (2-23) or Figure 2-17.

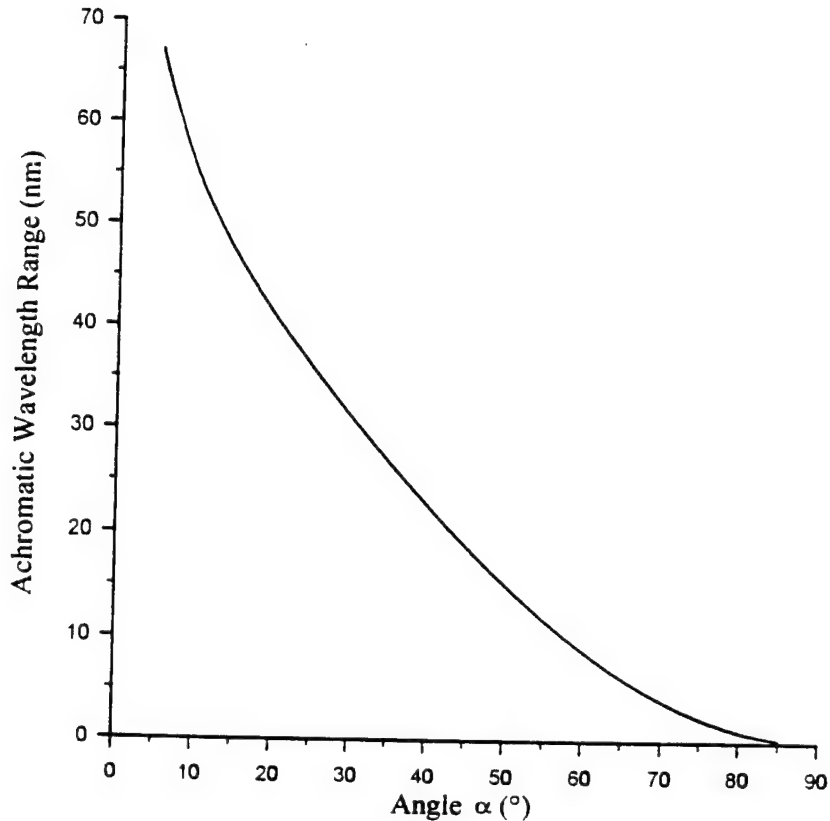


Figure 2-19
Calculated Achromatic Wavelength Range $R_{\lambda,1}$ for Beam Spot Shift Compensation at
 $g = 0.05$

2.2.7 Achromatic Prism-Glass Optical Backplane

The achromatic holographic grating couplers with three coupler elements designed above are excellent for the proposed backplane interconnect concept. However, it requires extensive engineering effort to implement it, since the hologram fabrication may involve film shrinkage which will change the hologram diffraction angles. The development time could be very long and is not practical to the Phase II program; but it does provide a way to optimize the holographic backplane.

Another way of providing achromatic coupling to the backplane is a simple prism-glass based optical backplane. This concept is shown in Figure 2-20. The incident beam is coupled to the total internal reflection beam in the backplane glass by a prism attached at the back surface. It simply reflects the incident light beam by its mirror treated surface. The

output coupling is based on the same prism coupling principle. There is no prism refraction involved; thus, it is an achromatic coupling.

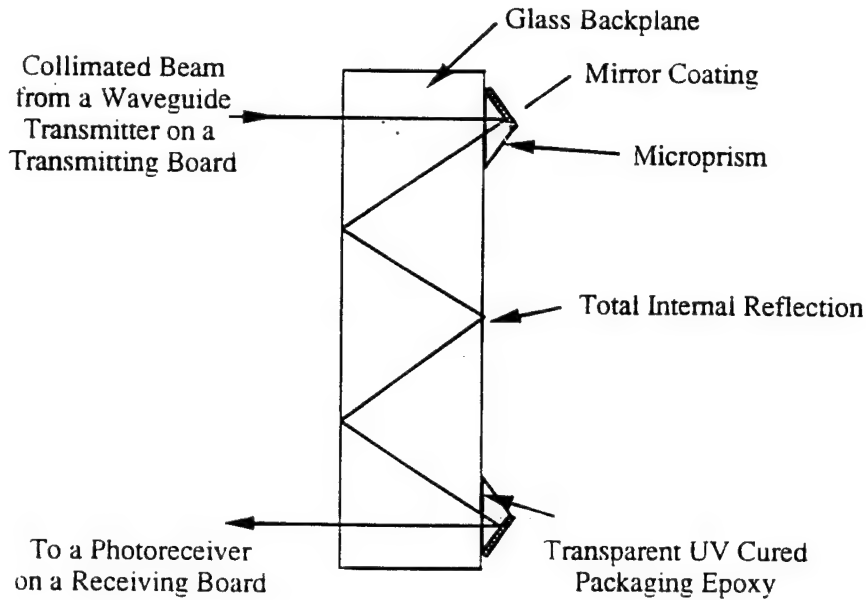


Figure 2-20
Prism-Based Optical Backplane

The prism size can be large or small. The smallest prism achievable is 100 μm in size. It is fabricated by fiber polling technology. In considering practical beam size, the prism size can be a few mm. The refractive index of the prism must be the same as the backplane glass in order to eliminate the boundary reflection which is responsible for part of the backplane loss. The index of the adhesion epoxy should also be the same as the glass backplane and the prism.

2.2.8 Guided Beam Receiver Array Design and Consideration

As was seen in Figure 1-1, the originally proposed guided beam receivers include channel waveguide arrays and waveguide photodetector arrays. The photodetector elements can be integrated with the interconnecting channel waveguides using evanescent field detection. These types of waveguide detectors have been demonstrated by a number of institutions. In order for this type of photodetector to operate effectively, the waveguide should be

single-mode, so that the add-on photodetector's absorption area can have significant interaction with the guided mode. This requirement conflicts with the backplane beam-to-waveguide input coupling requirement, where multimode waveguides are preferred. Multimode waveguide with large waveguide cross-section is much easier for backplane beam coupling, and also has larger alignment tolerance. This conflict thus calls for another type of guided beam photodetector, namely conventional PIN photodetectors, to be placed at the output ends of the receiving channel waveguides. This is a butt-coupling structure as shown in Figure 2-21. This type of photodetector is commercially available, and can be configured in single-element or array structure. The key issue is the packaging of the waveguide arrays with the photodetector arrays.

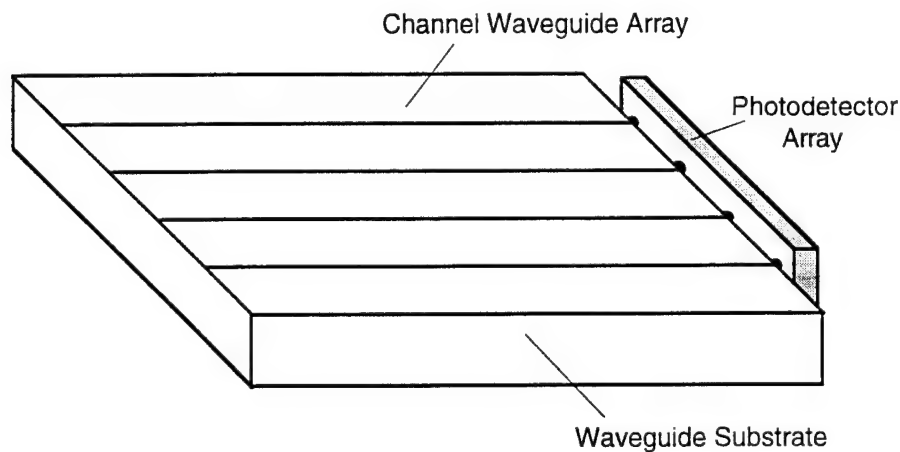


Figure 2-21
Butt Coupling of Receiving Waveguides and PIN Photodetectors

For many applications, each chip has one or a few single high data-rate I/O ports. The photodetectors may not be in close proximity for array packaging; most of the time they are quite separated from each other.

Using channel waveguide arrays to deliver optical signals to several different locations on a common board requires bending of the channels; but sharp bending of channel waveguides (with small bending curvature radii) results in significant waveguide bending loss. The technology is not yet mature for this type of waveguide interconnect.

There is a simple technique which can facilitate guided beam bending, efficient coupling of the backplane beam, and easy packaging with PIN photodetectors at different locations on a

common board. It is based on commercially available multimode fibers. The positioning of the fibers for on-board optical signal delivery is shown schematically in Figure 2-22. 100 μm diameter multimode fiber can be used to facilitate easy backplane beam coupling. It can also be easily butt coupled with a PIN photodetector using Fermionic photodetectors with ceramic fiber guides as shown in Figure 2-23. Once we fix the input array location (by silicon V-groove, with fiber spacing matched to backplane beam spacing), and the location of photodetectors, the fibers can be bent easily, allowing them to be placed and grooved on the board. The interconnecting fibers can lie between chips or on top of chips. A rugged fiber package, as shown in Figure 2-23, is thus possible.

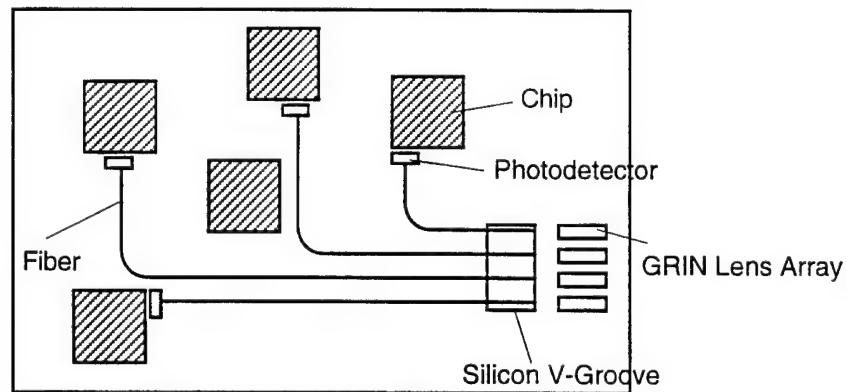


Figure 2-22
Fiber Based Guided Beam Receiver Arrays

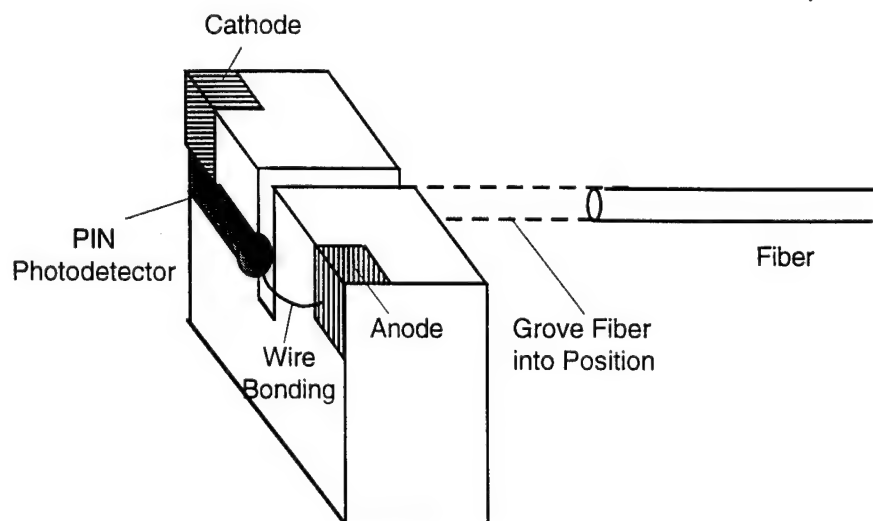


Figure 2-23
Rugged Fiber/Photodetector Packaging Using Fermionic Photodetectors with Fiber Guides

2.2.9 Advantages and Disadvantages of the Waveguide-Backplane Interconnect Concept

By now, we have covered most of the major structural issues of waveguide-backplane optical interconnects. The final prototype structure is given in Section 2.4. The advantages and disadvantages of the waveguide-backplane interconnect are summarized below.

Advantages

1. New achromatic holographic backplane interconnect concept.
2. Easy achromatic prism-backplane interconnect concept.
3. High-data-rate signal transmission based on miniaturized waveguide modulator arrays. Modulation is performed by chip output voltage not current.
4. Wide bandwidth data modulation by waveguide modulators.
5. Large fanout on the backplane with the use of multiplexed fanout holograms. This has been demonstrated with 1-to-59 fanouts and better than 55% overall efficiency.
6. Low power consumption at high-data-rate operation. Based on the comparison performed by Feldman et al, the point where optical interconnects are preferred over electrical interconnects is 100 MHz for interconnect distances longer than 4 mm, and 700 MHz for longer than 1 mm.
7. Low clock skew based on high-speed optical signal propagation.
8. Reduced capacitive and inductive loading effects.
9. Speed and bandwidth independent of interconnection distance.
10. Improved immunity from electromagnetic interference (EMI) due to reduced electrical interconnect length.
11. Low optical crossover crosstalk and excellent interconnect parallelities.
12. Low-loss signal transmission in waveguide and backplane.
13. No laser heating effect on chip performance; the laser diode can be outside the board.
14. Easy laser diode replacement. There is no stringent requirement on laser wavelength, to the use of achromatic backplane couplers.

Disadvantages

1. Requirement for careful backplane optical beam alignment. Alignment must be performed by an experienced engineer.
2. Increased alignment complexity with the increased number of I/O ports and boards.
3. Difficulty in developing an achromatic backplane holographic input/output coupler (although the technique for such development has been developed in Sec. 2.2.7).
4. High power loss due to backplane coupling. High power laser sources are required.

2.3 Fiber Ribbon Based Board-to-Board Optical Interconnect Structure

The major disadvantage of the waveguide-backplane interconnect structure stated above is the critical optical alignment. Alignment can become easier with good mechanical board and backplane packaging hardware, but even so, when misalignment occurs, repair requires an experienced engineer.

The fiber ribbon-based board-to-board optical interconnect structure to be covered in this section offers easier alignment packaging. It is not the interconnect concept originally proposed; we researched this in addition to the waveguide-backplane interconnect, owing to its near-term commercial potential. The fiber ribbons can work as jumpers with excellent alignment stability. The gain in easier alignment is at the expense of loss of the backplane's flexibility, some laser heating problems when directly modulating laser diode arrays, and limited data rate (to a few Gbits/s; the above waveguide modulators can be much faster). Some related component and structural issues are addressed below.

2.3.1 Laser Transmitter Arrays

It is possible to use waveguide modulator arrays as signal transmitters for high-data-rate applications. For the near term, most application data rates are within a few Gbits/s. It is

thus possible to use direct laser diode modulation with a built-in current-based laser diode driver array.

Laser diode arrays are presently under development at many research firms, but they are not yet commercially available. Physical Optics Corporation therefore established a CRDA (cooperative research and development agreement) program with Jet Propulsion Laboratory (JPL) in Pasadena, California, to generate laser diode arrays for board-to-board interconnect applications. JPL has successfully delivered a number of laser diode arrays to POC for experimentation and interconnect prototype packaging.

The device under development is a distributed-feedback laser array with four laser elements. The laser spacing is $250\text{ }\mu\text{m}$, matched with the spacing of the ribbon fibers. The lasing wavelength is $1.55\text{ }\mu\text{m}$. The operation threshold current is about 15 mA, and maximum operating current per laser is about 50 mA. Typical maximum output optical power per laser is about 2 mW. Figure 2-24 is a photograph of the laser array delivered by JPL to POC.

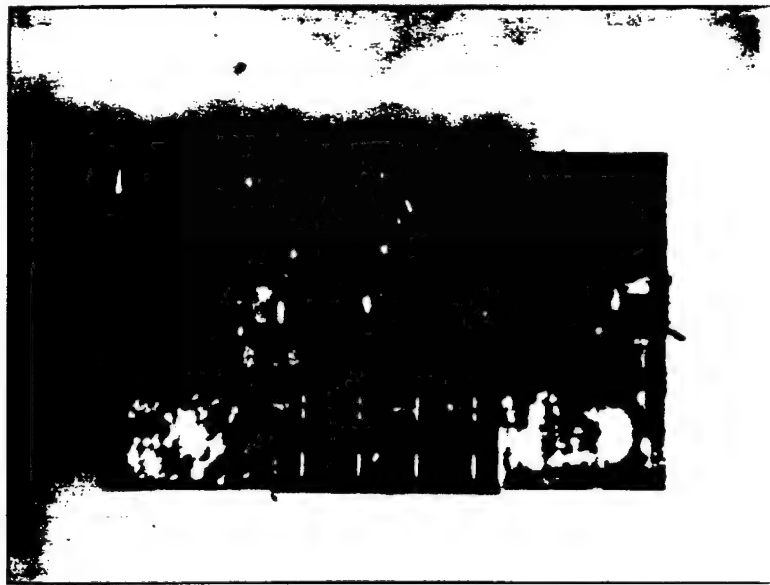


Figure 2-24
Photograph of the DFB Laser Diode Array Delivered by JPL to POC. It is suitable for fiber ribbon-based board-to-board optical interconnect applications.

2.3.2 Photodetector Receiver Arrays

To facilitate effective delivery of optical signals from one board to another, a photodetector array with identical element spacing is required. Commercially available photodetectors working at 1.55 μm wavelength are all single-element devices. Existing array devices are mostly found in the near-IR, as those at 830 nm wavelength for imaging applications. It is hard to find commercially available photodetectors array at 1.55 μm wavelength and with correct 250 μm spacing. We believe this is not due to technical limitations but to the present low market demand. The call for fiber ribbon array communication will stimulate the production of such photodetector arrays.

Currently, JPL also supplies POC with photodetector arrays for experimentation and prototype packaging. The InGaAsP PIN photodetector array shown in Figures 2-25 is first fabricated in the conventional way, but is then packaged on a specially designed ceramic packaging submount with wire bonding. It consists of four photodetector element. The whole unit can be mounted on an electronic board by epoxy-and-wire bonding. An electronic preamplifier, a post-amplifier and signal conditioning circuit, and the photodetector constitute the complete photoreceiver unit. More detail on the circuit design is given in Section 3.4.

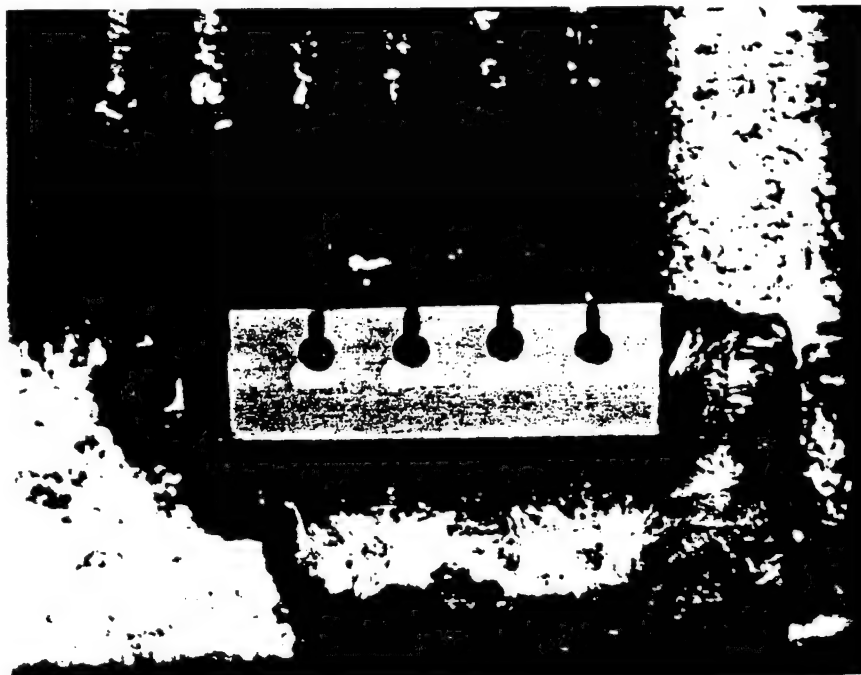


Figure 2-25
Photodetector Array Delivered by JPL to POC. The array element spacing is identical to the fiber ribbon spacing.

2.3.3 Fiber Ribbons and Ribbon Connectors

Fiber ribbons are now commercially available from AT&T and US Conec. Both companies offer single-mode ribbons and multimode ribbons. Typical fiber-to-fiber spacing is 250 μm . Standard ribbon arrays have four fibers, eight fibers, or twelve fibers. For our demonstration, we chose the array with four fibers, due to the available laser and photodetector array size. Since the board-to-board interconnect distance is relatively short, compared to long-distance fiber communications, the effects of material and modal dispersion on the data rate can be ignored. Multimode fiber ribbons can facilitate easy laser array-to-fiber-ribbon pigtailing and easy fiber-ribbon-to-photodetector-array pigtailing. The coupling power loss can also be reduced as compared to that associated with using single-mode fiber ribbons.

Figure 2-26 shows a photograph of the fiber ribbon purchased from US Conec. The schematic of the ribbon connector is given in Figure 2-27. With this design, handling of the array connector is quite simple, and can be done by any inexperienced engineer after a simple demonstration.

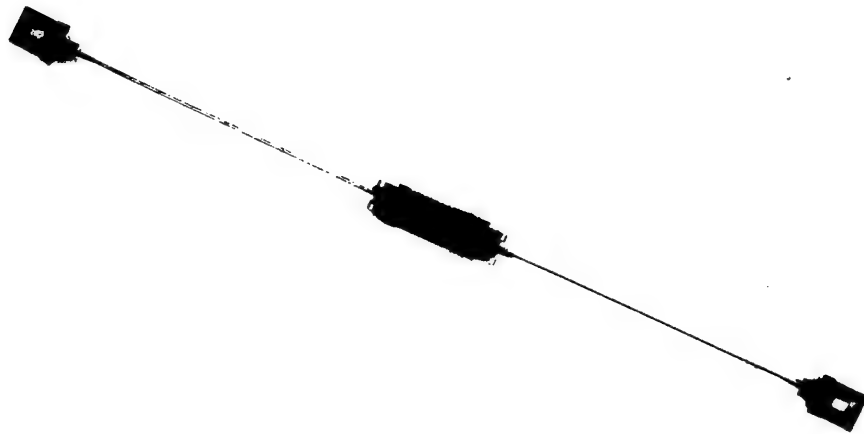
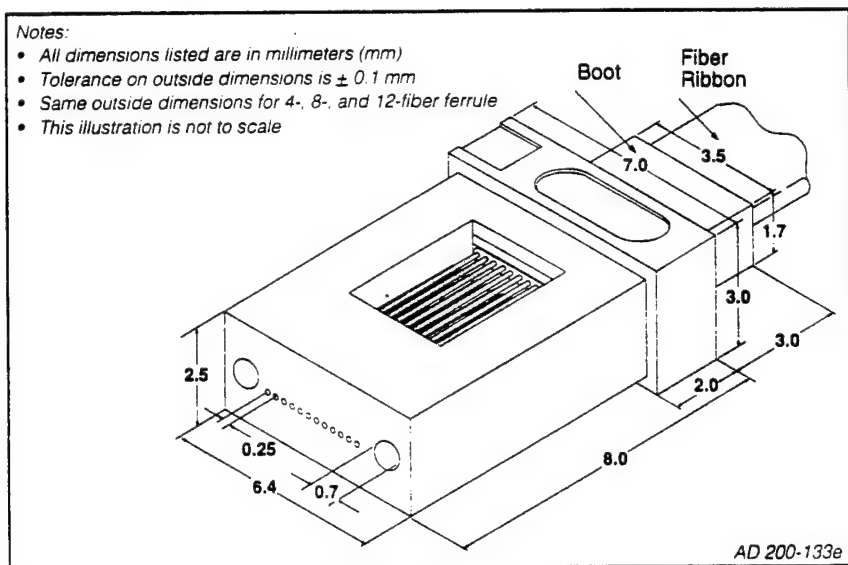


Figure 2-26
Multimode Fiber Ribbon



Above: 12-Fiber Ferrule

Below: Ferrule Alignment Using Guide Pins

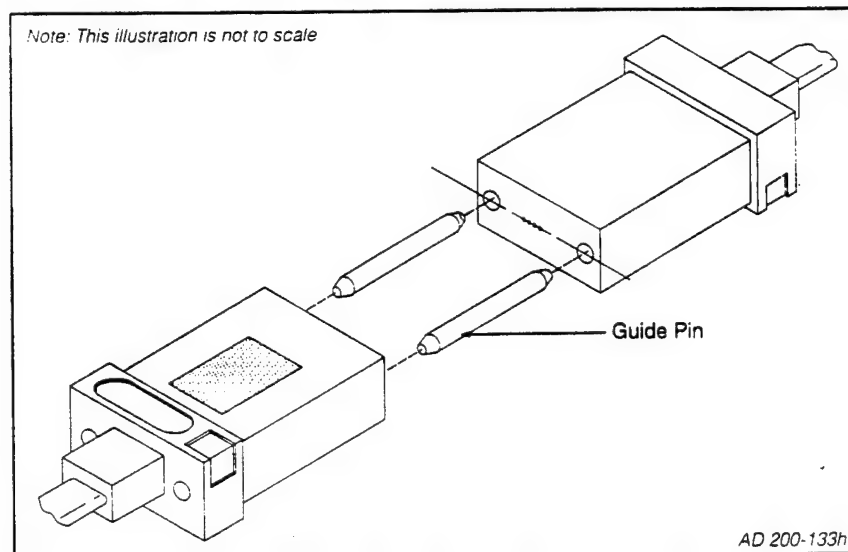


Figure 2-27
Schematic of the Fiber Ribbon Connector

2.3.4 Advantages and Disadvantages of the Fiber Ribbon Based Interconnect Concept

We have now covered most of the key component issues of fiber ribbon-based board-to-board optical interconnects. The advantages and disadvantages of the fiber ribbon interconnect are summarized below. Detailed designs of drivers and receivers are given in Section 3.3.

Advantages

1. The fiber ribbon interconnect is achromatic; it is not sensitive to laser wavelength variations.
2. The array packaging interconnect can save extensive packaging effort in conventional one-by-one fiber packaging.
3. The fiber ribbon can be multimode with a large core cross section; hence pigtailling with laser arrays and photodetector arrays is much easier.
4. The unit has excellent power budget from one board to the other, since power loss is minimal in fiber and input/output coupling.
5. Data rate can be up to several Gbits/s.
6. Power consumption is low at high-data-rate operation.
7. Clock skew is low, based on high-speed optical signal propagation.
8. Capacitive and inductive loading effects are reduced.
9. Speed and bandwidth are independent on the interconnection distance.
10. Reduced electrical interconnect length improves immunity from electromagnetic interference (EMI).
11. There is no optical crossover, and thus no optical crosstalk.

Disadvantages

1. Direct placement of laser arrays on a circuit board may result in heating the circuit board. Demand for heat handling is increased.
2. No optical fanout is possible with presently available fiber ribbons.
3. It is difficult to achieve optical signal distribution from one port to several port because no ribbon fanout component is available.
4. The data rate is limited, mostly by laser diode array, to a few Gbits/s.
5. The fiber ribbons can not be sharply bent, so extra space is required to facilitate large bending radii.

2.4 Revised Phase II Prototype Structure

Both waveguide-backplane optical interconnects and fiber-ribbon optical interconnects have their advantages and disadvantages, as described above. Both interconnect schemes are

important, and we will demonstrate both in one prototype even though only the waveguide-backplane concept was proposed in the Phase II.

Because of the addition of fiber ribbon interconnects and changes in the backplane structure, the interconnect structure as shown in Figure 1-1 has been modified. The revised schematic of the interconnect prototype is given in Figure 2-28.

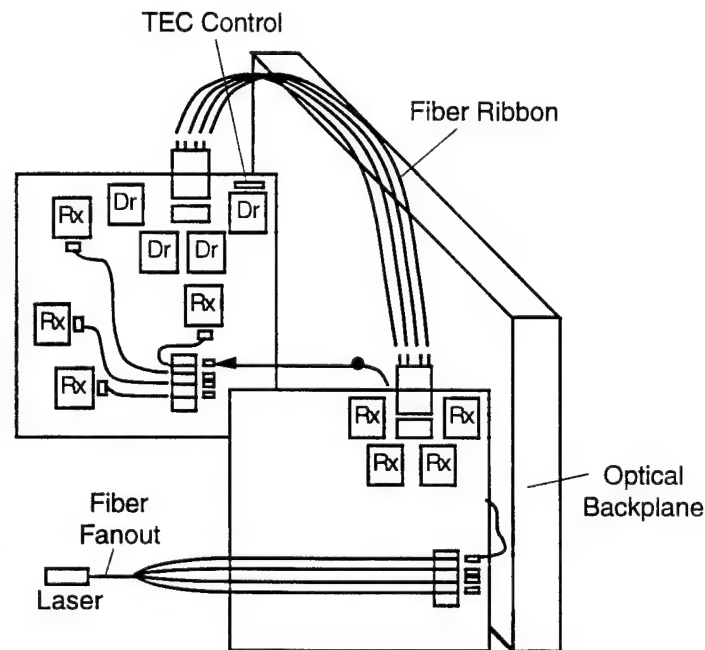


Figure 2-28
Revised Schematic of the Board-to-Board Optical Interconnect Prototype

Figure 2-29 shows the block diagram arrangement for board No. 1. It consists of a waveguide modulator array, a GRIN lens array, a fiber ribbon with connector, a photodetector array, and four receiver circuits. Figure 2-30 shows the block diagram arrangement for board No. 2. It consists of a silicon V-groove for fiber packaging, a GRIN lens array, four receiver circuits, four laser diode driver circuits, a laser diode array, and a fiber ribbon with connector.

The interconnect prototype shown in Figure 2-28 operates as follows. A high-power laser diode provides a CW light beam to a fiber fanout. The outputs of the fiber fanout are coupled into the waveguide modulator array. An external electrical driving signal

simulating the chip output drives the waveguide modulator array on board No. 1. The modulator array outputs are collimated by the GRIN lens array to the optical backplane, where light beams are coupled by a prism and are bounced between backplane surfaces. They are then coupled again by another prism to the receiving board and are focused by the GRIN lens array on board No. 2 into multimode fibers. The optical signals are then delivered by the fibers to different locations on board No. 2. The signals are received by four individual photodetectors which are butt-coupled to the fibers. The receiver circuits amplify the signal to correct digital format. The signal outputs from board No. 2 can be used for comparison with the input driving signal. The signal outputs from receivers on board No. 2 are also used as inputs to laser driver circuits on the board. The laser driver circuits convert the received voltage signals to correct current signals with proper laser biases. The modulated laser array outputs are fed into a multimode fiber ribbon with low coupling loss. The fiber ribbon delivers the optical signals back to board No. 1, where the signals are received by the photodetector arrays and are amplified and conditioned by the receiver circuits. The outputs of board No. 1 can also be used to compare with the original waveguide modulator driving signal.

Both interconnect concepts will be demonstrated by this single prototype. Two-way board-to-board optical interconnection will be achieved. The following section shows in detail the experimental processes leading to the final prototype packaging and interconnect demonstration.

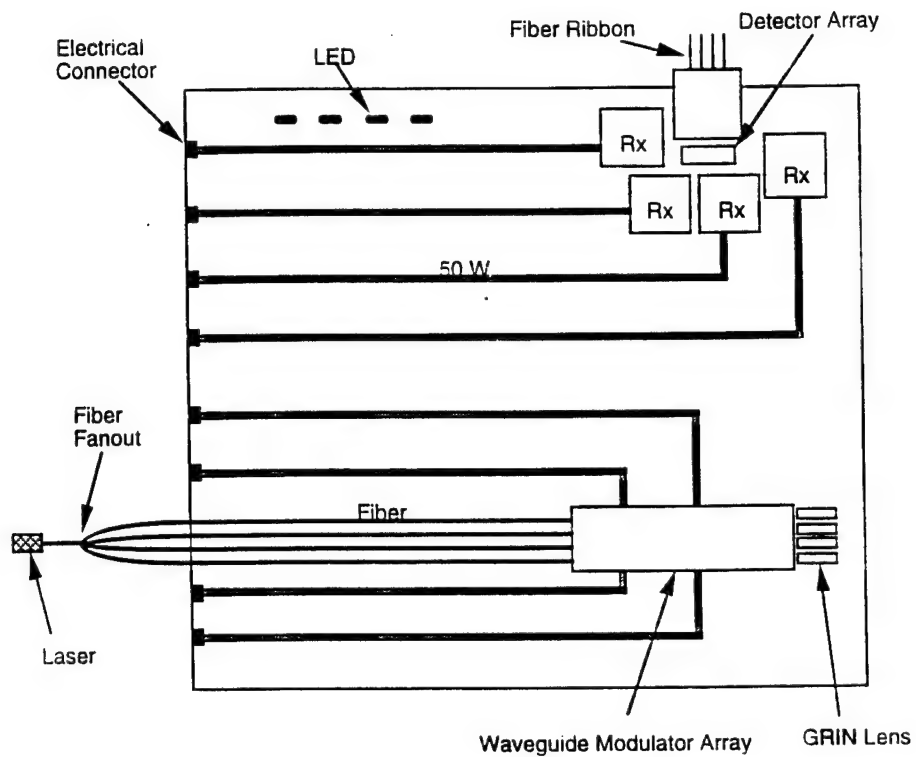


Figure 2-29
Schematic of the First Circuit Board

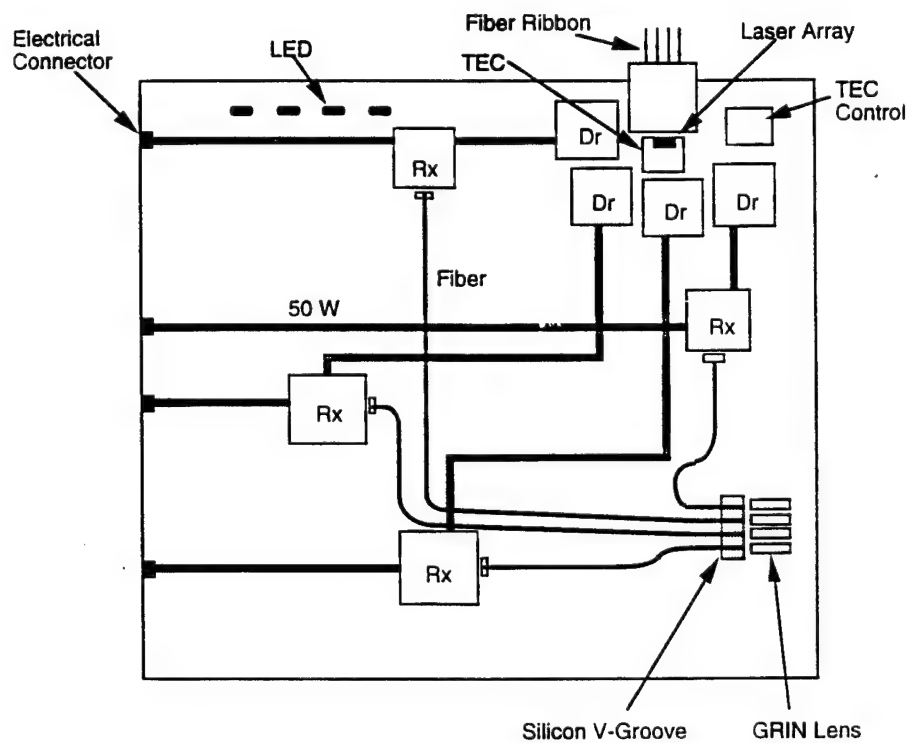


Figure 2-30
Schematic of the second circuit board.

3.0 PROTOTYPE DESIGN, FABRICATION, PACKAGING, AND PERFORMANCE

3.1 Design and Fabrication of Waveguide Modulator Arrays

3.1.1 Design and Fabrication of Waveguide Modulator

We have designed and fabricated waveguide modulator arrays to meet the requirements for optical interconnection. Since the modulator will be fabricated on an X-cut LiNbO_3 substrate, the electrical field introduced by the modulation signal will be applied along the optical axis (z direction), and the optical signal will propagate in the y direction so that the maximum electro-optic coefficient of LiNbO_3 can be used. A lumped electrode structure is used for flip-chip or wire bonding packaging, since the target working speed is between 100 MHz and 5 GHz. Before going on to the modulator array design, we first designed a miniaturized single modulator structure. Figure 3-1 shows the design layout of POC's single-unit Mach-Zehnder waveguide modulator. The overall size from y-junction to y-junction is about 5 mm.

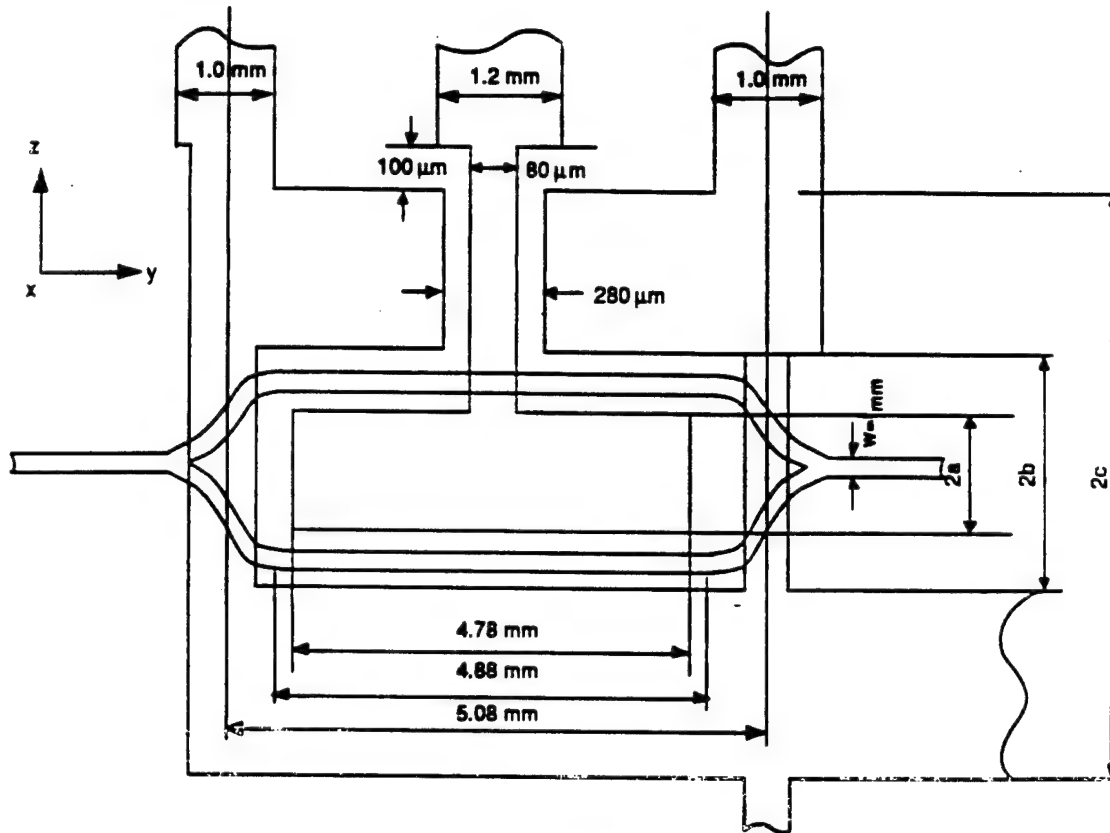


Figure 3-1
Design Layout of POC's Single-Unit Mach-Zehnder Waveguide Modulator

The selection of the device dimensions given in Figure 3-1 was based on a consideration of the relevant device factors, such as compactness, magnitude of the modulation voltage, working speed, optical interference from the two adjacent channels, and convenience for future packaging.

It is well known that waveguide bending at a y-junction causes losses, such as radiation loss due to curvature, and discontinuity and transition loss due to mode profile mismatching. In order to reduce bending loss at the y-junction, either coherent coupling bending or best-fit S-bending should be utilized. In this design, a sine function, whose first and second derivatives at the transition points are both zero, has been selected to provide the best possible waveguide bending and transition:

$$z = S(y) = \frac{h}{\ell} y - \frac{h}{2\pi} \sin\left(\frac{2\pi}{\ell} y\right) \quad (3-1)$$

where h and ℓ denote, respectively, the z -direction offset and the y -direction separation between the two waveguides to be connected by the s-bend. In the y -junction waveguide part of the Mach-Zehnder modulator, shown in Figure 3-2, h and ℓ are 19 and 800 μm , respectively, and the estimated bending loss at each y junction is less than 0.5 dB.

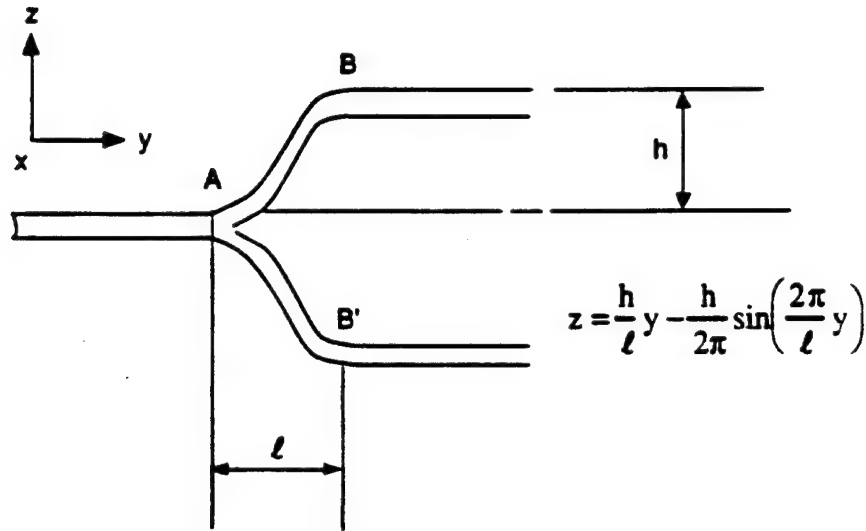


Figure 3-2
S-Bending at the y -Junction of the Mach-Zehnder Waveguide Modulator

Fabrication of the Waveguide Modulator

The designed waveguide modulator was fabricated on an X-cut LiNbO_3 substrate. The waveguide and electrode masks were fabricated at Photo Science, Inc. Figure 3-3 shows partial views of the waveguide mask. The mask includes an array of four Mach-Zehnder modulators.

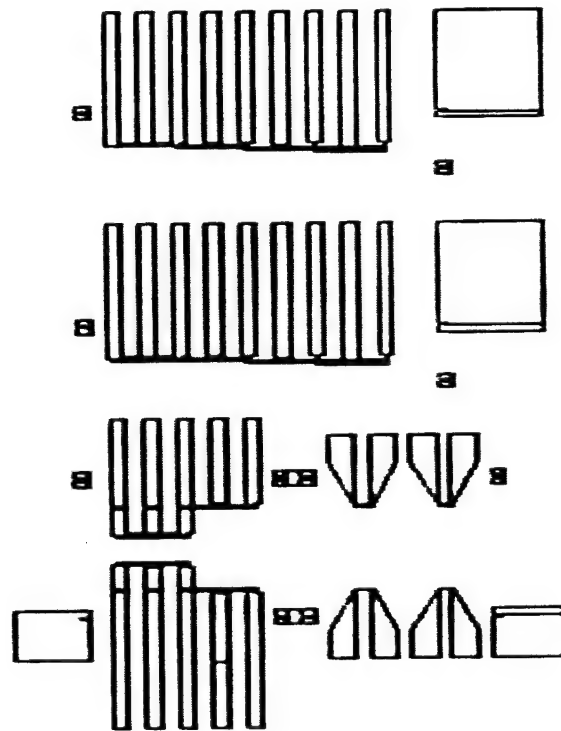


Figure 3-3
Mask Pattern of the Waveguide Mach-Zehnder Modulator

The waveguide fabrication procedure is shown in Figure 3-4. X-cut LiNbO_3 was purchased from Crystal Technology, Inc. and cut into $20 \times 11 \times 1 \text{ mm}^3$ pieces, using a diamond wire saw. Cleaned LiNbO_3 samples were then spin-coated with Shipley 1813 photoresist at 3500 RPM for 40 seconds. After prebaking at 90°C for 30 minutes, a waveguide pattern was transferred onto the samples using POC's Solitec mask aligner. The exposed pattern was developed in Shipley MF319 developer. To fix the pattern for further processing, the samples were baked for an additional 20 minutes at 120°C . We then coated on a typical Cr masking layer for proton exchange. This layer was 800 \AA thick, and was deposited using a thermal evaporator. A subsequent lift-off process produced the Cr mask pattern on the LiNbO_3 sample surfaces. The Cr layer protects the samples against proton exchange while the uncoated region allows proton exchange for waveguide fabrication.

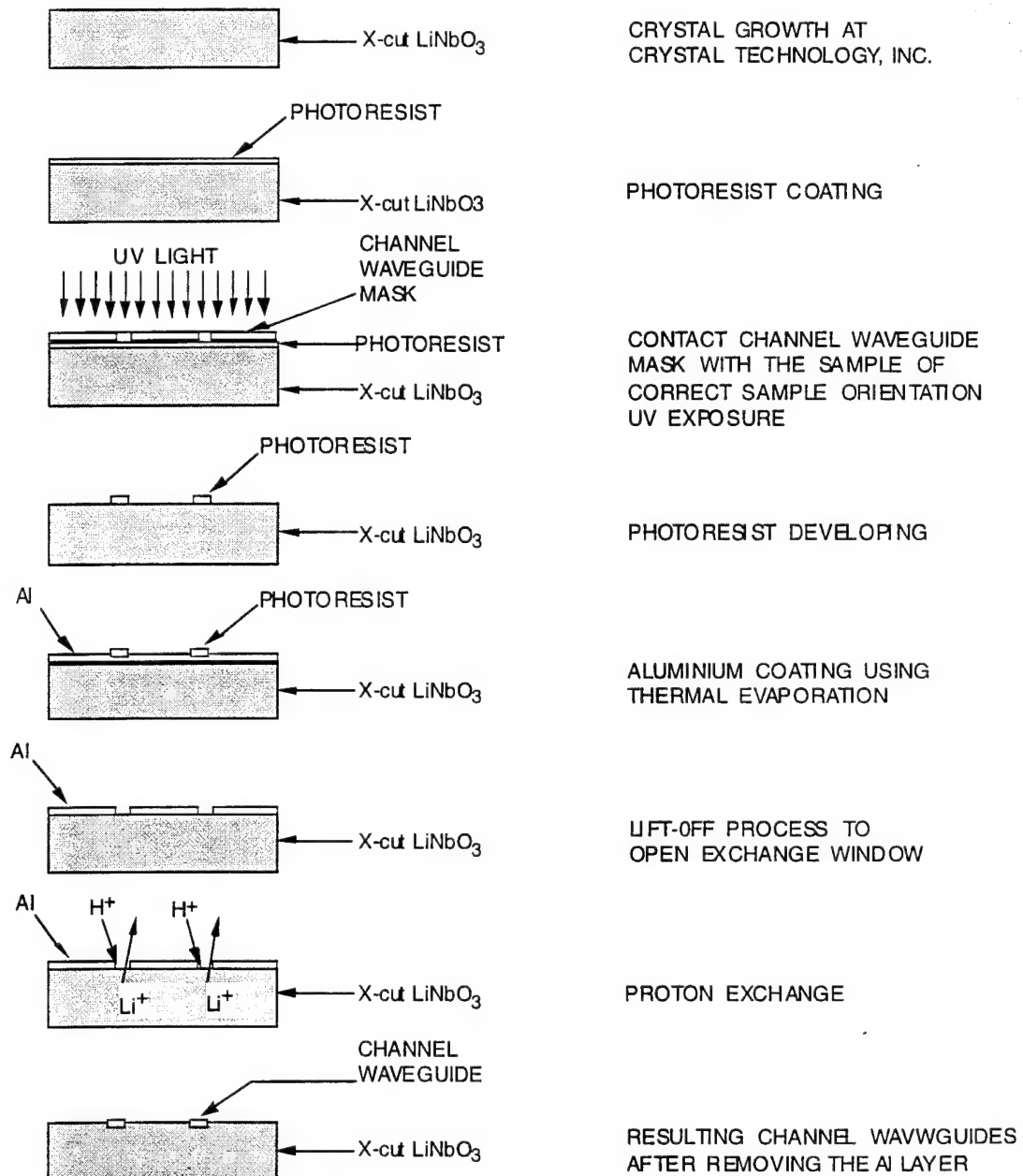


Figure 3-4
Process for Channel Waveguide Fabrication on an x-Cut LiNbO₃ Substrate

The proton exchange process was performed by immersing the samples in molten benzoic acid, which can be either pure or diluted, at a temperature of from 200°C to 220°C. The proton ions in the melt exchange with the Li ions in the LiNbO₃ crystal through the exchange window in the Cr mask. The substrate portion which receives the increased proton concentration experiences a locally increased optical refractive index. This higher index portion forms the optical waveguide. A channel waveguide 5 μm wide and 0.2 to

0.5 μm deep can easily support optical guided modes; the number of modes supported depends on the above proton exchange process and optical wavelength used.

The resulting waveguide cross section was not circular, as assumed above. This causes difficulty in mode profile matching for efficient fiber/waveguide pigtailling. A thermal annealing process can be introduced, however, to allow mode profile tailoring. The annealing is performed at 300° to 400° C for 1.5 to 3 hours to increase the depth of the waveguide and to modify the waveguide mode profile. Waveguide fabrication is completed by cleaning the samples and removing the Cr masking layer.

More Details on Proton Exchange and Thermal Annealing

During the PE process, the patterned LiNbO_3 substrate is immersed in a protonic source, i.e., an acid (e.g. benzoic acid, palmitic acid, stearic acid, cinnamic acid, and mixtures) or a hydrate melt (e.g., $\text{Mg}(\text{NO}_3)_2 \times 6 \text{H}_2\text{O}$), at the appropriate temperature for a given length of time. The lithium ions in the substrate are first depleted, and then replaced, partially or completely, by the hydrogen protons in the protonic source. In this way, the refractive index of the LiNbO_3 substrate is increased in the area where the PE process takes place, and the specified waveguide is thus formed. The overall PE process can be described, using typical benzoic acid as the source, by the following equation:



where x determines the extent of the process. When $x < 0.12$, there is only a single rhombohedral phase, the so-called α phase, in equilibrium. The lattice constants in the α phase are approximately the same as in the undoped LiNbO_3 , and thus the waveguide region is structurally matched to the substrate. Therefore, input light can be guided without harmful scattering. As x is increased further, some complicated phases start to appear. First, at $x > 0.12$, a second rhombohedral phase, the so-called β phase, is in equilibrium. Secondly, at $x > 0.65$, the third rhombohedral phase (γ) is in equilibrium. Finally, at $x > 0.77$, some cubic HNbO_5 occurs.

Unlike the α phase, the β and γ rhombohedral phases and the cubic HNbO_5 have considerably different lattice constants from the undoped LiNbO_3 . Thus, they result in a great deal of scattering at the boundaries between regions, and even in some structural

damage. Because of these different lattice constants, the resulting waveguide is not only lossy, but unstable.

Based on the foregoing study and analysis, both dilute PE (DPE) and annealed PE (APE) have been used in the process of improving our modulator. The general purpose of both DPE and APE is to control the proton exchange ratio, x , to a suitable value. This x value should be large enough to produce good guided mode confinement and, at the same time, should be small enough to prevent the unwanted β and γ phases in equilibrium, and even cubic HfNbO_5 , from appearing. Although both DPE (plus annealing) and APE worked well in our investigation, the APE method is preferred for the following reasons:

1. APE is simpler: only pure benzoic acid is used, so there is no need for very accurate dilution.
2. APE is faster: the PE process can be completed in only a few or tens of minutes with APE, compared to the several hours needed by DPE.
3. APE is easier to control: we found that with proper PE, the subsequent annealing can control both the exchange ratio (x) and the waveguide depth. Thus, a single-mode waveguide with optimal mode confinement and mode profile is easier to fabricate by APE than by DPE.

3.1.2 Modulator End-Face Polishing and Optical Coupling

To facilitate the device butt coupling, shown in Figure 3-5 (necessary for fiber/waveguide pigtail, and output beam collimation and focused input beam coupling by GRIN lenses), the device's end faces were polished to optical quality. The polished devices were tested with a HeNe laser at a wavelength of 632.8 nm. The incident laser beam was first coupled in by an optical fiber. A sizeable portion of the laser energy was thus coupled into the channel waveguide, and exited at the other end of the device. A microscope objective placed near the device end functioned as an imaging lens, and the near-field image of the output device was focused on a screen. A bright spot located at the center of the device designates the channel throughput light while the upper and lower background light is the uncoupled portion of the incident beam in air and substrate, respectively. Similar experimental testing was performed in Phase II, first using a HeNe laser at 632.8 nm, and

again using a laser diode at $1.3\text{ }\mu\text{m}$. When the modulator is properly thermally annealed, the spot on the screen looks circular and is very bright.

Figure 3-7(a) shows the near-field view of a light spot when the laser wavelength is $1.3\text{ }\mu\text{m}$. In this picture, it can be seen that the spot is well separated from both the substrate mode and the air mode light. This verifies that the mode confinement in the channel waveguide is indeed satisfactory.

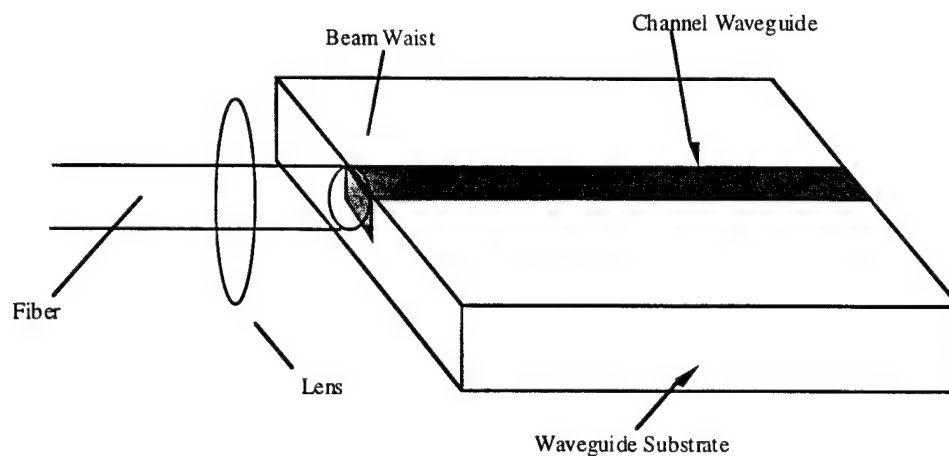


Figure 3-5
Schematic of Butt-Coupling From Fiber to Channel Waveguide

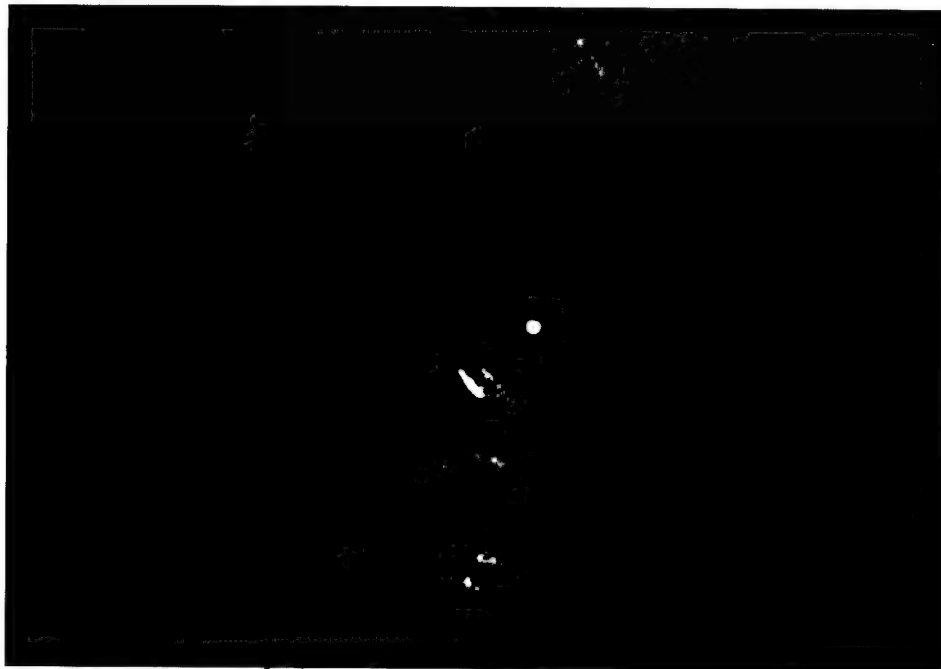


Figure 3-6
Near Field View of the Output Spot from a Mach-Zehnder Modulator

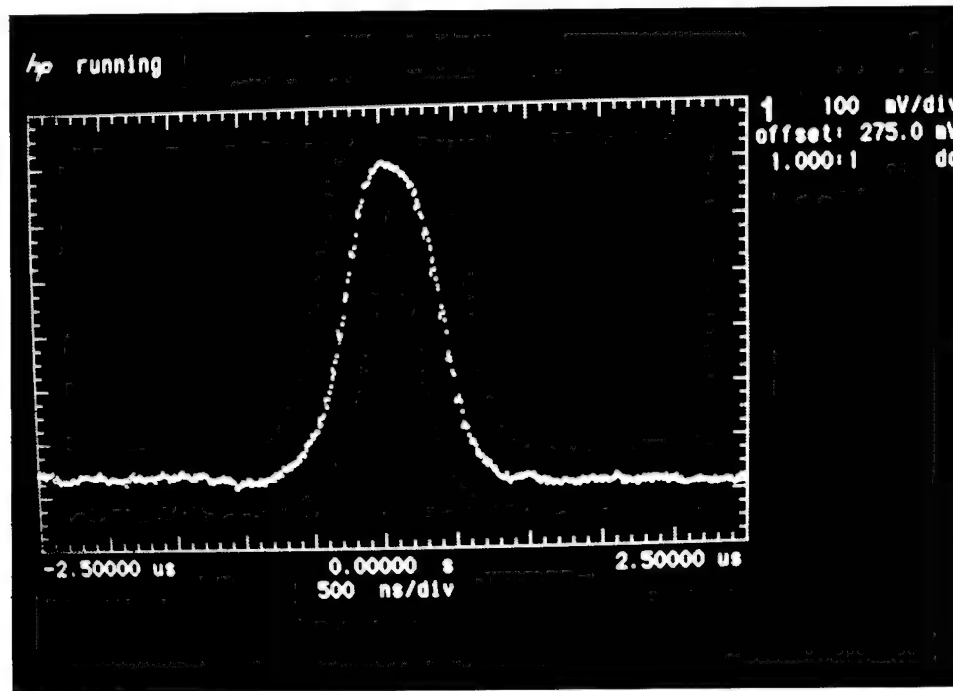


Figure 3-7
Mode confinement in the Mach-Zehnder modulator mode profile of the guided light.

In addition, checking the degree of symmetry of the spot shape confirms that the waveguide aspect ratio, the ratio of width to depth, is well within the design value of $(5 \text{ mm}/3 \text{ mm}) = 1.67$. Figure 3-7(b) shows the mode profile measured by a video camera and a sampling oscilloscope. This profile tells us that the channel waveguides are, indeed, working in a single mode regime at $1.3 \mu\text{m}$ wavelength and that the light confinement is good enough to provide a satisfactory mode profile with $1/e$ widths close to the waveguide width.

3.1.3 Electrode Pattern Design and Fabrication

After the demonstration of channel waveguide arrays with polished end-faces, electrode patterns had to be deposited on the channel waveguide arrays to facilitate electro-optic intensity modulation. Figure 3-8 shows our electrode mask design. Figure 3-9 shows the cross section view of electrodes on the channel waveguides that provide the required E_z tuning fields.

Typically, the electrodes used in conventional electro-optic modulators are made of Cr/Al or Pt/Au fabricated by thermal evaporation or sputtering. In this experiment, Cr/Al electrodes were chosen for ease of thermal evaporation and their low cost. The fabrication process for the Cr/Al electrodes on LiNbO_3 substrate is illustrated in Figure 3-10. The lengthy

experimental procedures involved sample surface cleaning in a clean room environment; photoresist spin coating; a baking treatment; contact printing of the electrode pattern on the channel waveguide sample with μm alignment accuracy; photoresist developing; Cr/Al metal deposition; and lift-off processing.

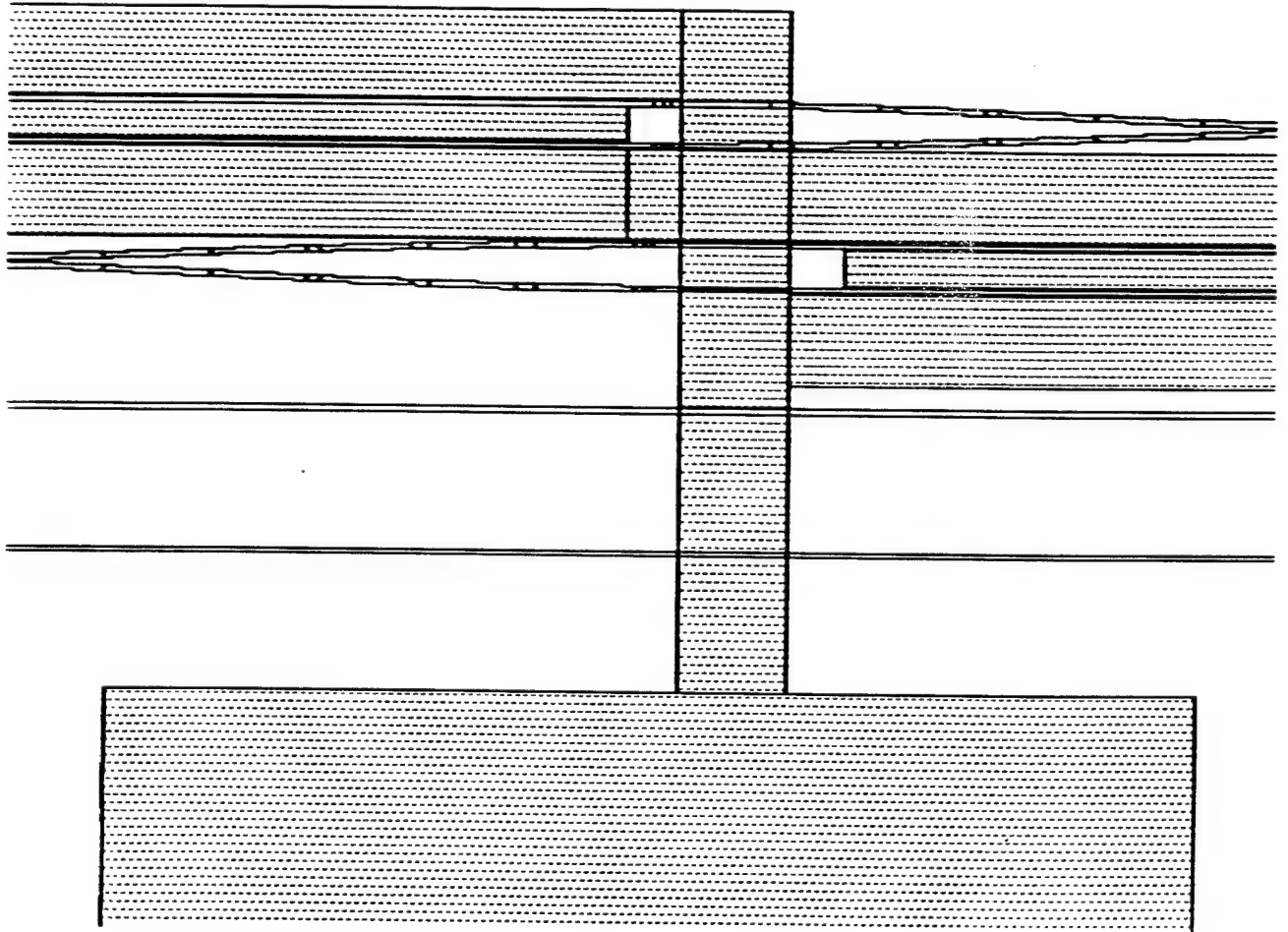


Figure 3-8
Electrode Mask Pattern

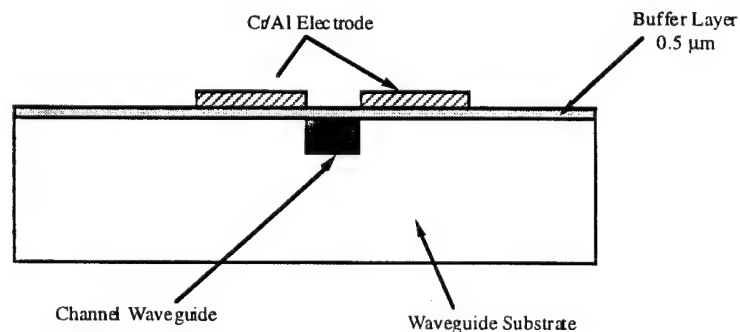


Figure 3-9
Cross sectional view of electrodes on channel waveguides.

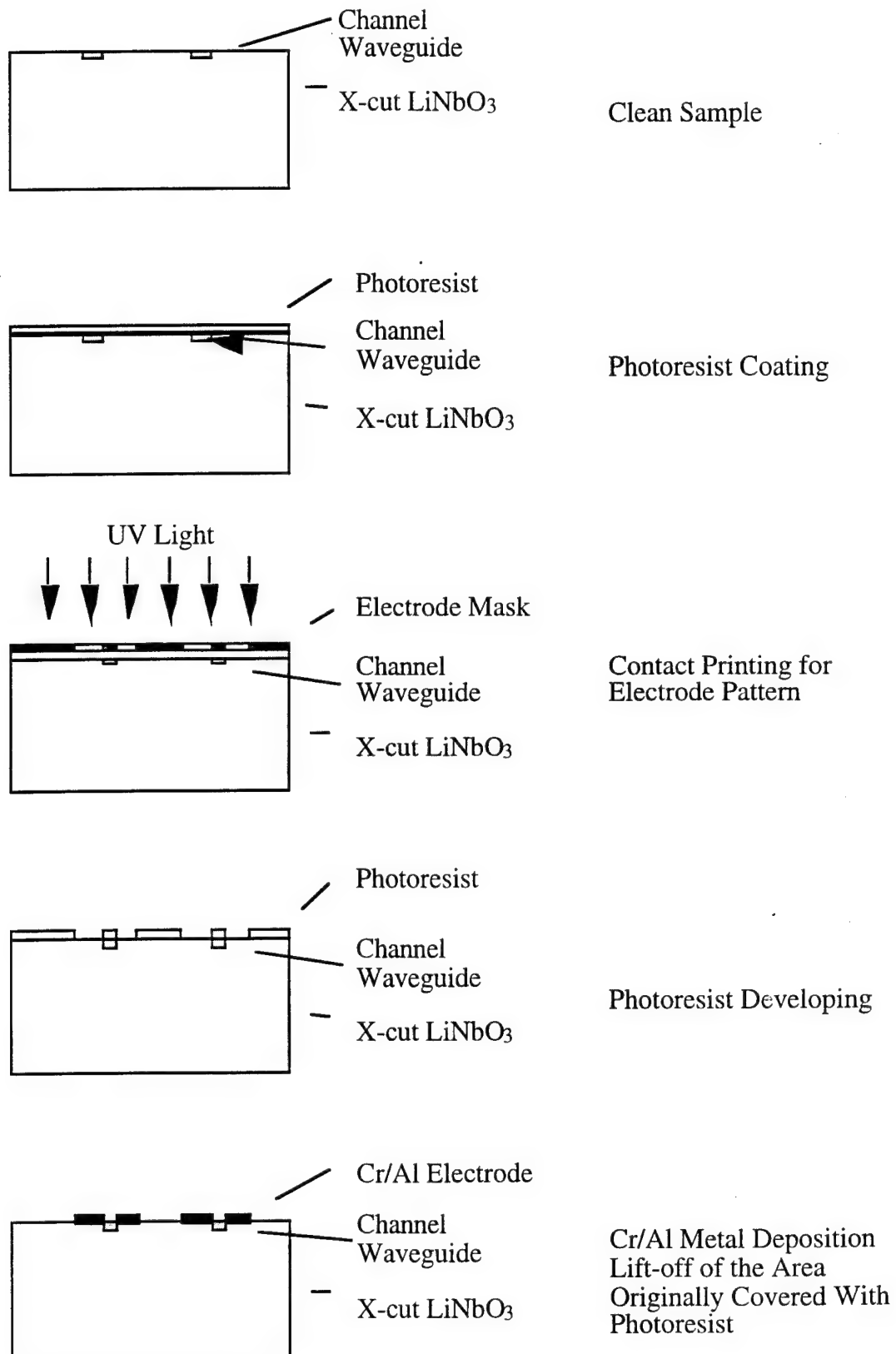


Figure 3-10
Fabrication process for electrode pattern deposition on a channel waveguide sample.

3.1.4 Modulator Testing

Following waveguide and electrode fabrication, the modulator samples were mounted on an optical alignment stage to facilitate optical coupling. The optical mode spot as described in Section 3.1.3 was positioned on a PIN photodetector with 1 M Ω termination load at the oscilloscope input. A driving electrical signal from a function generator, as an initial low frequency test, was placed on the electrode pair by a pair of electrical probes (see Figure 3-11). This facilitated initial electro-optic testing without forming a complicated electro-optic testing module. The reason for this initial testing was to help determine the modulation performance, from which we would be able to determine whether the device was single-mode or not, and whether the two arms of the Mach-Zehnder waveguide modulator were symmetric or not. A good modulation performance enables us to proceed further for fiber/waveguide pigtailling or forming a complete modulator module with wire bonding and MS input electrical connector. When a poor modulation is identified, further thermal annealing treatment can be performed to improve the modulations. A bare device is suitable for thermal annealing treatment.

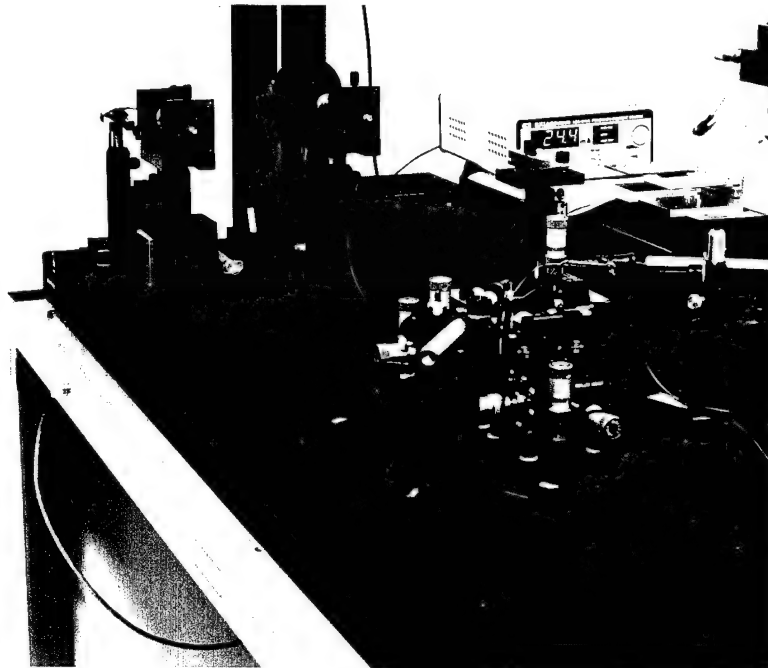


Figure 3-11
Probe testing of waveguide modulator array

Through careful control of proton exchange and follow-on thermal annealing processes (discussed in Section 3.1.5), our waveguide modulators have demonstrated a modulation depth of over 99% at 13 VP-p driving voltage. Figure 3-12 shows the modulation depth measurement on an oscilloscope. Similar depth has been observed below 4Vp-p (not shown). The upper trace is the driving signal used for the modulation measurement, the lower trace is the modulated optical signal detected by a photo diode, and the straight line at the bottom is the reference zero optical power line. Excellent modulation depth is clearly observable.

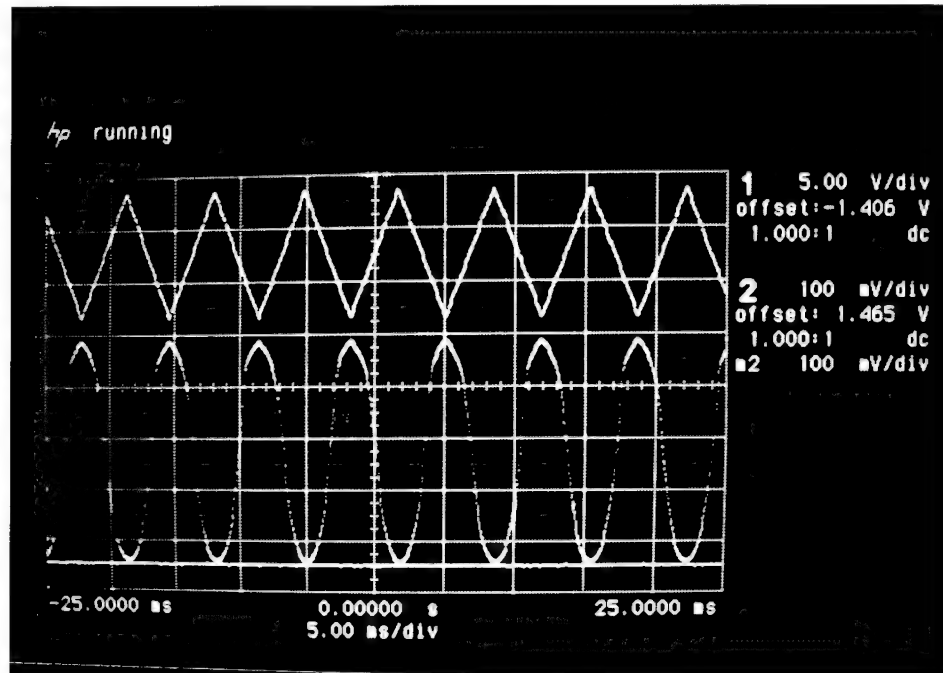


Figure 3-12
Over 99% modulation depth produced by POC waveguide modulator.

3.1.5 Summary of Design and Fabrication Parameters

In this section, we summarize the design and fabrication parameters. The design parameters listed in Table 3-1 show good agreement with our actual device parameters. The estimated modulation bandwidth is about 1.06 GHz. It is in agreement with the frequency response simulation shown in Section 3.1.7.

Table 3-1. APE Parameters Used By POC

Channel waveguide width	5 μm
Gap between internal and external electrodes	6 μm
Length of internal electrode	5.08 mm
Width of internal electrode	31 μm
Width of external electrodes	28.5 μm
Type of Y-function	S-bending type
Length of each Y-function	800 μm
Electrode material	Cr/Al layer
Average length of bonding lines	5 mm
Average width of bonding lines	300 μm
Total electrode capacitance	4.1
Total electrode inductance	6.5 NH
Total resistance electrode	9.8 Ω
Calculated	5.1 V
Calculated bandwidth	1.06 GHz

Here, the half wave modulation voltage, V_P , is calculated using the formula

$$V_P = \frac{pG\lambda}{2n^3\gamma_{33}\Gamma\ell}, \text{ where } p \approx 1 \text{ is the electrode coefficient, } G = 6 \mu\text{m} \text{ is the gap between}$$

internal and external electrodes, $\lambda = 1.3 \mu\text{m}$ is the optical wavelength, $n = 2.2024$ is the extraordinary refractive index of LiNbO_3 , $\gamma_{33} = 30 \times 10^{-12} \text{ m/V}$ is the electro-optic constant of LiNbO_3 in the crystal orientation used, $\Gamma \approx 0.5$ to 0.6 is the overlap integral between the electric field and the optical mode, and $\ell = 5.0$ is the effective length of the electrode. The working bandwidth was analyzed by using the RLC equivalent circuit, with the R, L, and C parameters in Table 3-1 considered.

Table 3-2 summarizes the fabrication parameters of POC's modulator.

Table 3-2. Fabrication Parameters of POC's Integrated Mach-Zehnder Modulators

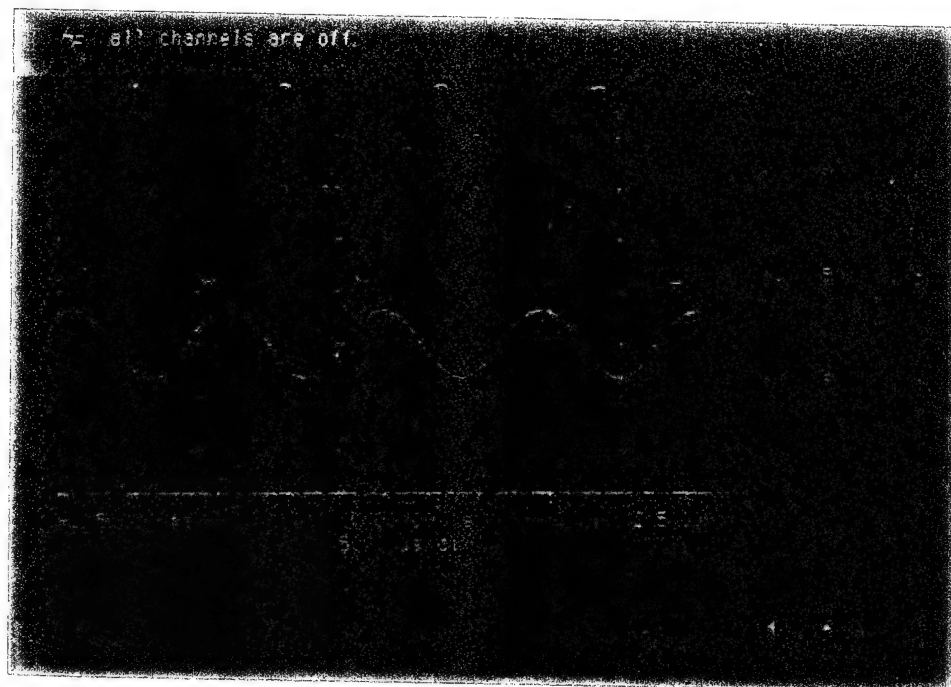
Substrate Material	X-cut LiNbO ₃
Protection Layer	Cr Layer of 800 Å Thickness
Working Wavelength	1.3 μm
Protonic Source	Pure Benzoic Acid (C ₆ H ₅ COOH)
PE Temperature	200°C
PE Time	23 Minutes
Annealing Temperature	350°C
Annealing Time	3 Hours, 30 Minutes
Annealing Atmosphere	Ambient Atmosphere
Modification Annealing Temperature	350°C
Modification Annealing Time	10 Minutes

By using the processing described, satisfactory Mach-Zehnder modulators have been fabricated. These modulators show good mode profiles and optical throughput.

3.1.6 Thermal Annealing for Modulator Performance Optimization

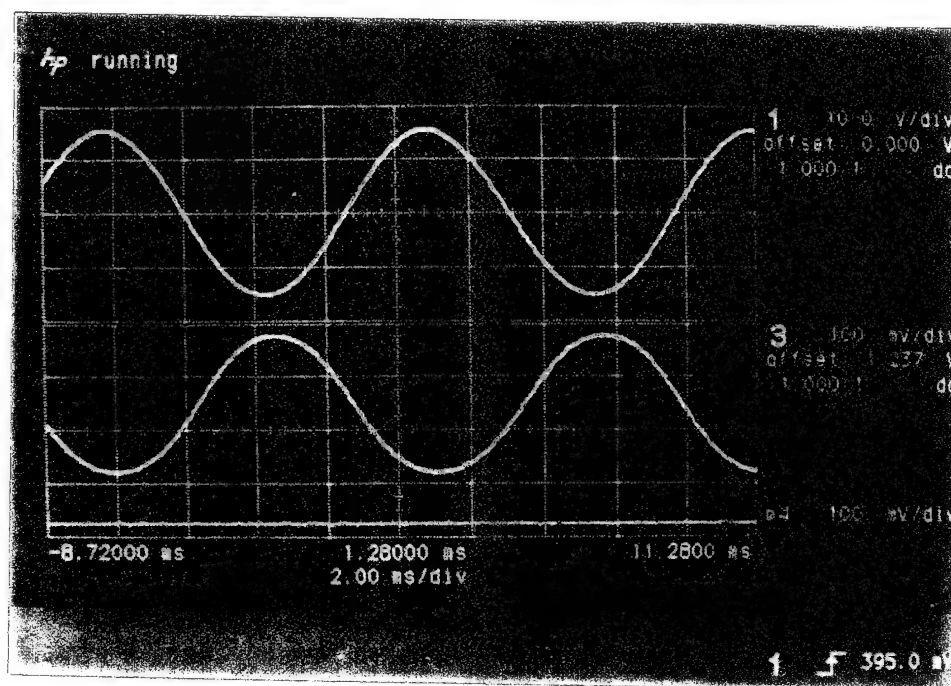
Usually, the first run modulator fabrication does not result in the modulation performance of Figure 3-12. Initial testing sometimes sees only a 20% to 30% modulation depth. Improvement in the performance of the waveguide modulator was attained through better-controlled waveguide and electrode fabrication, and the use of thermal annealing to tailor the waveguide mode profile and to change the waveguide to a single mode condition. The latter is essential to attain better performance from the Mach-Zehnder waveguide modulator structure.

Refined device fabrication and the subsequent thermal annealing at a temperature of 350°C has resulted in improved device performance. Figure 3-13 shows a 36% modulation depth measured before annealing; Figure 3-14 shows the 70% device modulation depth measured after annealing, under a driving voltage of 15 V. In both figures, the upper trace is the drive signal, the lower trace is the modulated signal, and the bottom straight line is the reference zero light level. The modulation depth is about double after annealing. Further annealing resulted the aforementioned 99% modulation depth shown in Figure 3-12.



36%

Figure 3-13
Measured waveguide modulator modulation depth of about 36% under a driving voltage of 15 V. This measurement was taken before thermal annealing.



70%

Figure 3-14
Measured waveguide modulator modulation depth of about 70% under a driving voltage of 15 V. This measurement was taken after thermal annealing.

Due to the low speed nature of the simple probe testing approach, the present modulators were measured at low signal speeds. For example, the result in Figure 3-12 was attained at a speed of about 110 Hz. A PIN photodetector was used for the measurement. The input to the oscilloscope had an input impedance of 1 M Ω rather than 50 Ω . This high load impedance caused the measured speed to be low. After the modulator device is packaged with a 50 Ω SMA connector for signal input, a 50 Ω load impedance is used and high-speed measurements can then be implemented. Despite the initial measurement speed limitations, we measured the modulator electrode capacitance to be 6 pF. Using a termination resistance of 50 Ω , the anticipated modulation bandwidth is estimated to be 1.06 GHz.

3.1.7 Fabrication of Modulator Arrays

Based on optimization studies of modulator arrays, we continued our effort on the fabrication of the waveguide modulator array with waveguide fanouts. We anticipated that the waveguide bending structure may degrade the modulator throughput due to coupling from the guided mode to the substrate mode, and that the optimization of the fabrication process may need considerable attention.

Thus far, three types of Mach-Zehnder modulator array devices have been designed and fabricated. The first type is an array device with four Mach-Zehnder modulators integrated in a single piece of X-cut LiNbO₃ substrate in parallel, with a separating distance of 2 mm between adjacent modulators. The size of the device is 22 x 20 x 1 mm. The advantages of this array type are: (1) each of the modulators can be used independently, (2) the separation between the modulators is large enough to accept 1.8 mm GRIN lenses as the output collimating units, and (3) the optical power from each of the laser diodes can be fully applied to each modulator. This device is the most practical array device for our optical interconnection application, and the device has been successfully fabricated. In fact, the following mode profile and throughput measurement were measured on this type of array device.

The second type is an array device with four Mach-Zehnder modulators integrated in a single piece of X-cut LiNbO₃ substrate 40 x 20 x 1 mm in size. The distinguishing feature

of this device type is that a one-to-four fan-out channel waveguide tree is designed and employed to feed all four modulators from one single laser diode light source. The advantages of this array type are: (1) only one light source is required for all four modulator units; (2) the entire device is more compact; and (3) commercial 1.0 mm GRIN lenses can still be used to accept and collimate the output light.

The measurement results of the second type modulator array show that all of the functional portions work. The input light from our single-mode fiber was successfully fanned-out to each modulator. From each modulator, a certain level of modulation depth, from 30 to 50%, was measured. However, the overall performance of this array device is not satisfactory; the mode confinement in each modulator is not good enough because the output spot cannot be completely separated from the substrate or air modes. Also, the overall optical throughput is much poorer than we expected.

After careful study and analysis, the following factors have been found to be the most likely sources of the observed performance degradation.

First, the large waveguide bends employed in this array device make it more critical to fulfill the single-mode well-confined guiding condition, and thus may degrade mode confinement and throughput. As shown in Figure 3-15, we have designed six types of bends that produce the required y-junctions and fanin and fanout bending. According to the propagation of light in the corresponding bend area, between 2.7 degrees and 12.1 degrees in this large bending device. These types of offset angles make the guided wave deviate from its best confined propagation direction, the y-direction, for this particular X-cut LiNbO₃ device (because the TE mode propagating in the y-direction "sees" the largest index change, Δn_e , in the proton-exchanged waveguide). As a result, mode confinement becomes more and more critical as the bending angle gets larger and larger. In other words, when the offset angle increases, more and more guided light tends to be lost due to guided-mode-to-leaky-mode transformation. Some literature states that the bending angle should be smaller than 7 degrees for well-confined guiding.

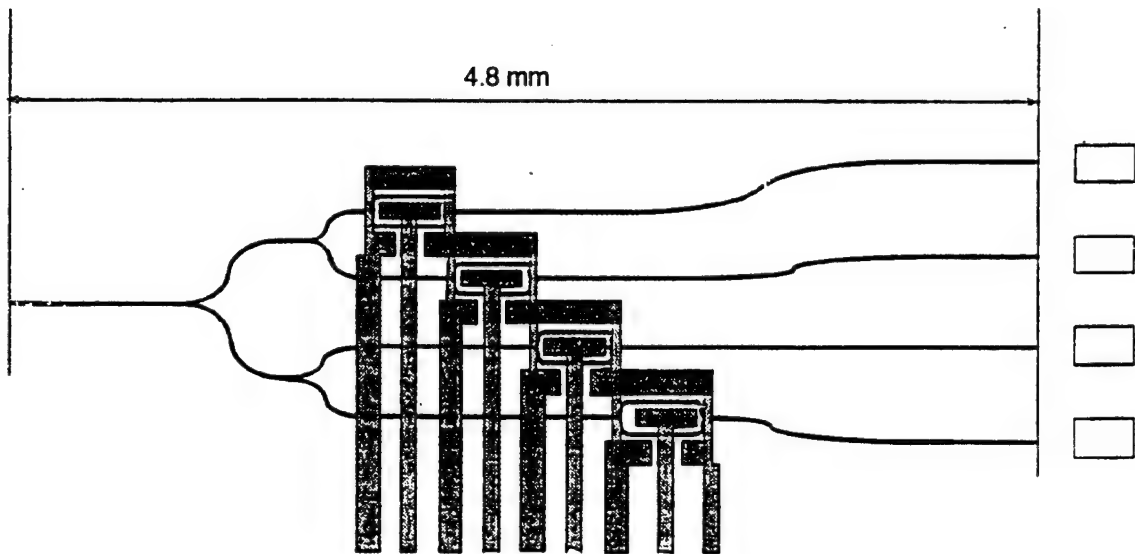


Figure 3-15
Waveguide layout of a fanout Mach-Zehnder modulator array device.

The second reason for the poor guiding in this device may be temperature changes during the fabrication process. The furnace used to implement the APE process was replaced, but the fabrication data used were collected with the previous furnace. Any temperature difference might cause some changes in waveguide parameters.

The last reason is that the fan-out array pattern covers a large area of the substrate. The slight temperature gradient in the processing equipment might prevent both the waveguides and bends from achieving simultaneous optimization.

The third type of array device is similar to the second one, but with the modulator separation distance reduced to $125\text{ }\mu\text{m}$. The purpose of designing this device model is: (1) to connect with an optical fiber ribbon with $125\text{ }\mu\text{m}$ fiber separation; and (2) to achieve satisfactory mode confinement. According to our calculations, the largest possible bending offset angle is 3.3 degrees, well below the quoted 7 degrees for good mode confinement.

Figure 3-16 shows the second and third types of waveguide modulator arrays. Each has four modulator elements. The waveguide fan-outs have been incorporated into the

structure. The modulation depths for these devices have been measured to be near 40%. The relatively low modulation depth in the present modulator array is possibly due to the unsatisfactory overlap of the modulated signal with the background signal, which was in turn caused by poor isolation of the mode spot and background light. Future device optimization will take this effect into consideration, and a better waveguide should result. Based on the considerations of optical throughput and modulation, the first Mach-Zehnder modulator device was selected for the final interconnect prototype packaging.

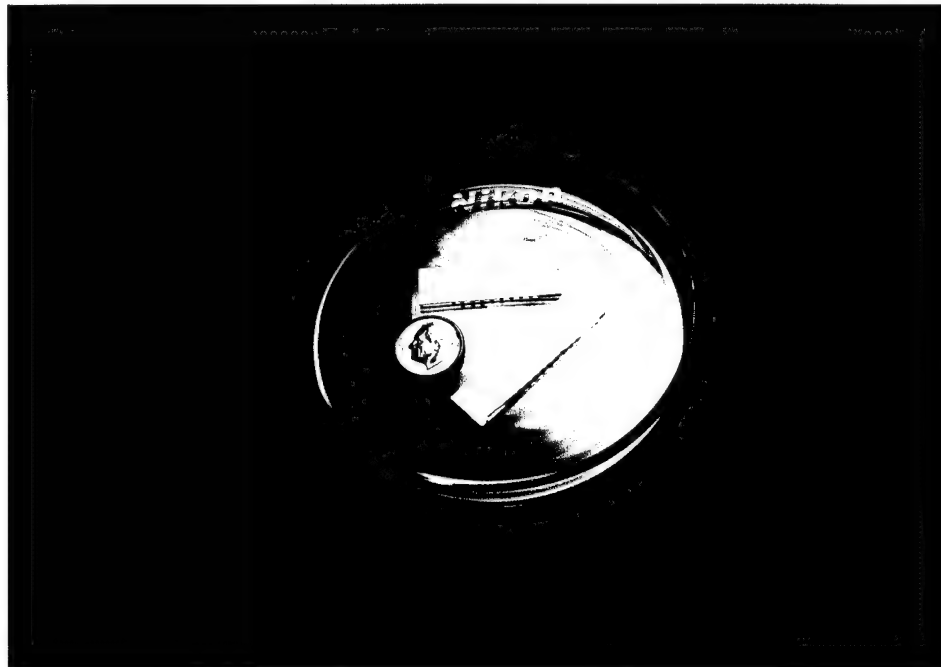


Figure 3-16
Developed waveguide modulator array with four element modulators and channel waveguide fanouts.

3.1.8 Optical Throughput and Loss Analysis

Figure 3-17 shows a block diagram of the experimental setup for optical throughput measurement.

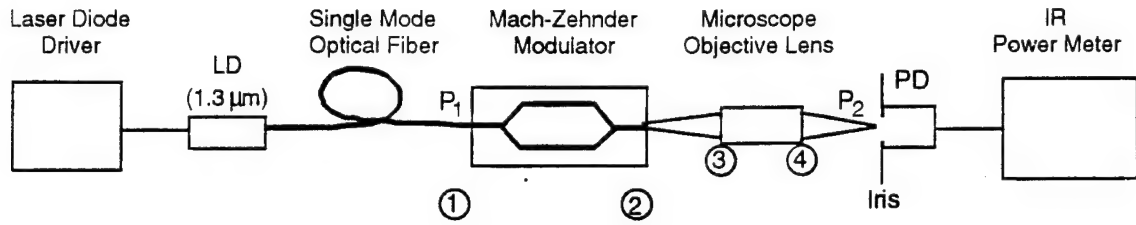


Figure 3-17
Block diagram of the experimental setup for optical throughput measurement

Here, an InGaAsP/InP laser diode (OK1 OL327C) was used as the light source for a wavelength of 1.3 μm . The output light of this laser diode was first coupled into a regular single-mode optical fiber. The output light from the fiber was then coupled to the Mach-Zehnder modulator through an end-face contact. Next, the output light from the modulator was picked up by a 10x microscope objective lens, and subsequently transferred to an attached photodiode. All measured optical powers were read out through a 1.3 μm IR power meter. As shown in Table 3-3, the measured optical power P_1 from the fiber was 0.9 mW, and the output power P_2 measured from the objective lens was 150 μW . Note that in the measurement, the output spot of the guided light was well separated from both substrate and air mode light by finely adjusting the position of the microscope objective lens. Further separation was attained by using an adjustable iris. Therefore, the overall optical throughput can be calculated as $T = 900/155 @ 5.81 @ 7.64$ (dB). This value includes the throughput of the modulator, the contributions of the Fresnel reflection from all interfaces' and the mode profile mismatch between the optical fiber and the channel waveguide. As shown in Table 3-3, the Fresnel losses come from two air/LiNbO₃ interfaces, each involving a loss of 0.76 dB (16%), and two air/lens interfaces, each involving a loss of 0.18 dB (4%). The fiber waveguide mismatch loss can be estimated by using the following equation:

$$\alpha_2 = \frac{3.6}{\left(\frac{W}{a} + \frac{a}{W}\right)\left(\frac{d}{a} + \frac{a}{d}\right)} \quad (3-2)$$

where W and d denote, respectively, the $1/e$ mode width and the depth of the channel waveguide, and a denotes the $1/e$ size of the optical fibers. With $W = 5 \mu\text{m}$, $d = 3 \mu\text{m}$, $a = 9 \mu\text{m}$, we obtain

$$\alpha_2 \cong \frac{3.6}{\left(\frac{5}{9} + \frac{9}{5}\right)\left(\frac{3}{9} + \frac{9}{3}\right)} \cong 3.39 \text{ dB} \quad (3-3)$$

By subtracting the above external losses from the overall throughput, the optical throughput of the modulator is

$$7.64 - (2 \times 0.76 + 2 \times 0.18 + 3.39) = 2.37 \text{ dB} \quad (3-4)$$

After taking the polarization factor (usually 1.5 to 2 dB) into account, the real throughput is thus on the order of 1 dB. The measurement and analysis data are summarized in Table 3-3.

Table 3-3. Optical Throughput and Related Losses

Input Optical Power from Fiber P1	0.9 mW
Output Optical Power from Modulator P2	155 μW
Overall Optical Throughput	7.64 dB
Fresnel Loss $0.76 \times 2 + 0.18 \times 2$	1.88 dB
Loss from Fiber-Waveguide Mismatch	3.39 dB
Laser Diode Polarization Factor	1.5 to 2 dB
Total Loss	6.77 to 7.27 dB
Real Optical Throughput of Modulator	0.87 to 1.37 dB

The total optical throughput can be improved in the future by taking the following measures:

1. Using polarization maintaining fiber with a core size of 5 to 6 μm to reduce mismatching and polarization loss.
2. Butt-coupling the fibers to the waveguides at both the input and output ends using a refractive-index-matching optical adhesive to reduce Fresnel

reflection losses. The optical throughput from fiber-to-fiber is expected to be approximately 3 dB.

3.1.9 Modulator Frequency Response

High-speed modulation is desirable. With the aid of a high-speed signal generator, a signal amplifier, and a spectrum analyzer, we have measured the operating bandwidth of our waveguide modulator with a lumped center-tapped modulation electrode. The measured bandwidth is over 1 GHz. (This measurement was limited by the available 1 GHz signal generator.) In order to better access the performance bandwidth, we present a frequency response model for the waveguide electro-optic modulator. This will help in the estimation of the bandwidth, and will guide future device design.

In the first section, an RLC lumped-element modulator circuit is reviewed. While simple in concept, it does allow the inclusion of parasitic inductance and frequency-dependent electrode resistance. In the next section, methods for determining the values for the R, L, and C circuit elements are discussed and numerical values are determined for the circuit elements. The last section presents the simulation results for the modulators.

3.1.9.1 RLC Lumped-Element Modulator Circuit Model

In this section, the RLC lumped-element modulator circuit is reviewed. Based on the paper, "Broad-Band Guided-Wave Electro-Optic Modulators" (R. A. Becker, IEEE J. Quantum Electron. QE-20, 723-727 (1984)), this model was shown to be quite accurate for modulators whose measured frequency response ranged from DC to more than 6 GHz.

The model consists of the simple RLC circuit as shown in Figure 3-18. Here, V is the generator voltage; R_s is the generator's source resistance (typically 50Ω); R_t is the source termination resistance (often 50Ω); R_e is the effective electrode resistance and can be frequency-dependent; L is the inductance of the electrode and bonding wires; and C is the electrode capacitance. Obviously, the important parameter is the voltage that one can develop across the electrode capacitance as a function of frequency. Note that the use of a 50Ω source termination resistance reduces the effective source resistance to 25Ω , which will enhance the frequency response; but to achieve the same voltage across the electrode

capacitance, the generator voltage must be doubled. Nevertheless, the $50\ \Omega$ source termination resistance is often used to provide an impedance match to the generator (at least at low frequency) and essentially double the frequency response.

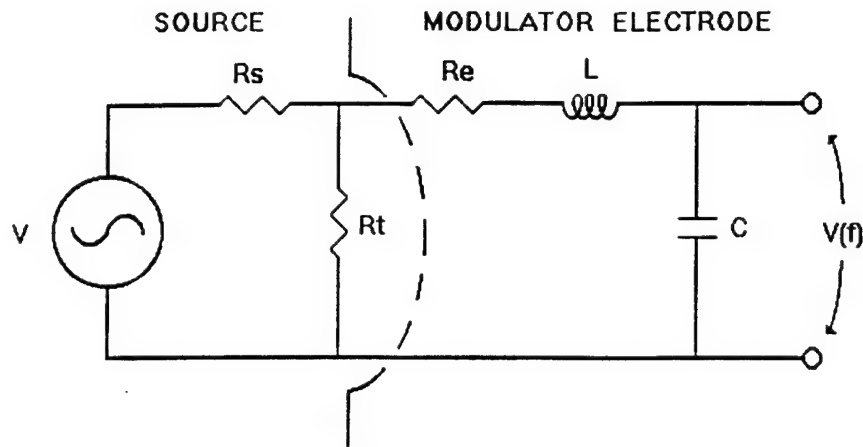
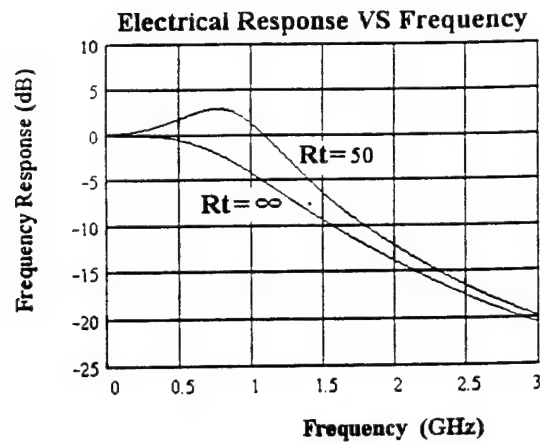


Figure 3-18
RLC Circuit Model for Grating Coupler Modulator

To see how circuit element values affect frequency response, it is useful to run several simulations varying the different elements. The first simulation will explore the difference between a modulator with and without a source termination resistance. The rest of the circuit elements are shown on the plot. The results are shown in Figure 3-19(a). Notice that the $50\ \Omega$ termination resistance increases the bandwidth by roughly 100%. However, significant peaking is visible due to the relatively large 6 nH parasitic inductance. Figure 3-19(b) shows the result when the parasitic inductance is halved, to 3 nH. Note that the peaking is reduced and the bandwidth is increased further by about 35%. In Figure 3-19(c), the capacitance is halved. The result is a 3 dB bandwidth that exceeds 2.5 GHz. However, significant peaking is again seen even for the 3 nH parasitic inductance.



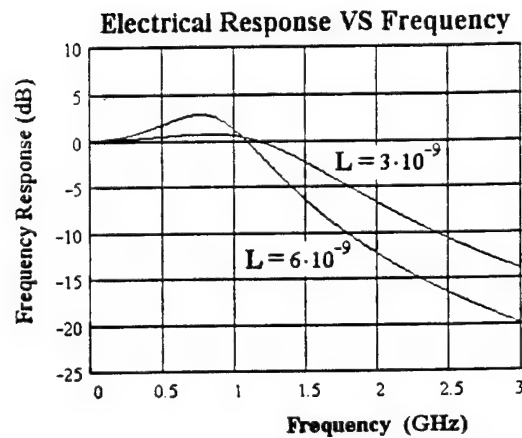
$$C = 5 \cdot 10^{-12} \text{ F}$$

$$L = 6 \cdot 10^{-9} \text{ H}$$

$$R_s = 50 \text{ Ohms}$$

$$R_o = 2 \text{ Ohms}$$

(a)



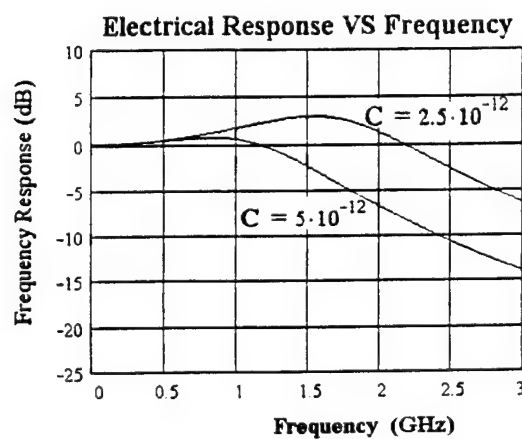
$$C = 5 \cdot 10^{-12} \text{ F}$$

$$R_s = 50 \text{ Ohms}$$

$$R_t = 50 \text{ Ohms}$$

$$R_o = 2 \text{ Ohms}$$

(b)



$$L = 3 \cdot 10^{-9} \text{ H}$$

$$R_s = 50 \text{ Ohms}$$

$$R_t = 50 \text{ Ohms}$$

$$R_o = 2 \text{ Ohms}$$

(c)

Figure 3-19
Circuit Model Simulations. (a) with and without 50- Ω termination resistance; (b) 3nH and 6nH inductance; and (c) 2.5pF and 5pF capacitance.

Up to this point, the assumption has been that the electrode resistance is a constant. However, as the frequency of operation rises, this is no longer accurate, because of skin depth effects. The frequency dependence of the electrode resistance can be expressed as

$$R_e = R_o + R_f \cdot \sqrt{f} \quad (3-5)$$

where the coefficients R_o and R_f can be empirically fit. For example, for a coplanar waveguide electrode with length equal to 4 mm, center-electrode width equal to 35 μm , a 4 μm wide gap, and a 1 μm thick Au metallization, the coefficients were determined to be

$$R_o = 2 \quad (3-6)$$

$$R_f = 2 \cdot 10^{-4} \quad (3-7)$$

Figure 3-20 shows the frequency response for a device when the frequency-dependent resistance is taken into account. Note that the effect of the inductive peaking is reduced by the additional resistance and that the frequency response is flatter, but the bandwidth is reduced somewhat.

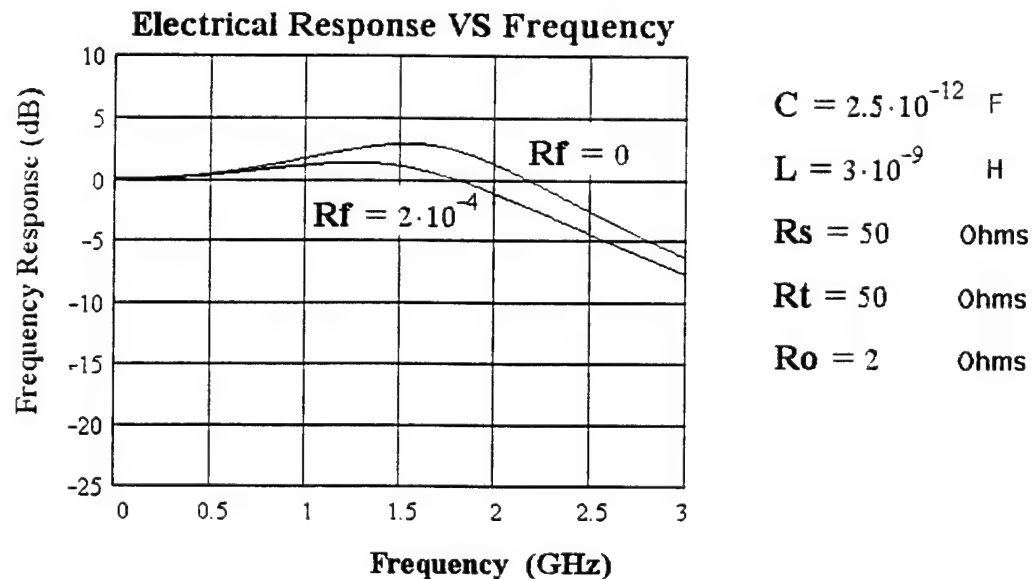


Figure 3-20
Circuit Model Simulation with and without Frequency-Dependent Electrode Resistance

From Figures 3-19 and 3-20, the following conclusions can be drawn:

1. The use of a 50 Ω source termination resistance may double the bandwidth in comparison to that obtained when no termination resistance is used.
2. The lower the effective source resistance, the more the peaking is increased due to parasitic inductance. However, some inductive peaking can be useful in flattening the response over some bandwidth at the expense of a more rapid roll-off beyond it.
3. The smaller the capacitance the better. However, again the parasitic inductance results in more peaking.
4. The electrode resistance is a function of frequency and will affect the measured frequency response.

An understanding of this circuit model allows the device (and package) designer to enhance the frequency response by judiciously choosing the correct values for the circuit elements.

3.1.9.2 Determination of Circuit Element Values

This section presents equations that estimate the circuit values attributable to the electrode structure.

Capacitance

The capacitance of the grating electrode structure can be estimated to the first order by using the simple design equations found in Microstrip Lines and Slotlines by K. C. Gupta, R. Garg, and I. J. Bahl. The capacitance per unit length of the coplanar strip electrode can be expressed as

$$C = (\epsilon_r + 1) * \epsilon_0 * b/2a \quad (3-18)$$

where $b/a = K'(k)/K(k)$; $k = S/(S+2W)$; $\epsilon_r = 35$ for LiNbO_3 ; S = electrode gap; W = electrode width; and $K(k)$ = complete elliptic integrals.

Inductance

The inductance of the grating electrode can also be estimated using coplanar strip analysis. Here the following approximation will be used:

$$Z_c = \sqrt{L/C} \quad (3-19)$$

thus

$$L = \epsilon_0 (120\pi)^2 (K(k)/K'(k)) \quad (3-20)$$

where L and C are both per-unit length. In addition, the inductance of 1-mil diameter bond wire is 1.2nH/mm.

Resistance

The resistance of the electrode can be calculated from its dimensions, given that the resistivity of the deposited metal, is known. A typical range for evaporated Au is $2.0 \times 10^{-6} \Omega\text{-cm}$ to $5.0 \times 10^{-6} \Omega\text{-cm}$. The handbook value for Al is $2.8 \times 10^{-6} \Omega\text{-cm}$. The best way to determine the resistivity of a deposited metal is to measure it. The electrode resistance is given by the expression

$$R = \rho L/A \quad (3-21)$$

where L is the electrode length and A is the electrode cross-sectional area. The frequency dependence of the resistance can be determined empirically, as described in the previously cited papers. Typically, R_0 is the DC resistance that is either measured or calculated and R_f is a "fit" parameter.

Based on the equations, we estimate that the capacitance is 4.1 pF, the inductance is 11.5 nH, and the DC resistance is 13 Ω .

3.1.9.3 Modulator Simulations

Based on the RLC circuit model developed in the first section, frequency response simulations can be run for the circuit element values determined above. The elements can be modified to determine how the frequency response is affected.

Figure 3-21 shows the simulated frequency response for the LiNbO_3 modulator for the calculated capacitance value. A 3 dB bandwidth in excess of 1 GHz is attained.

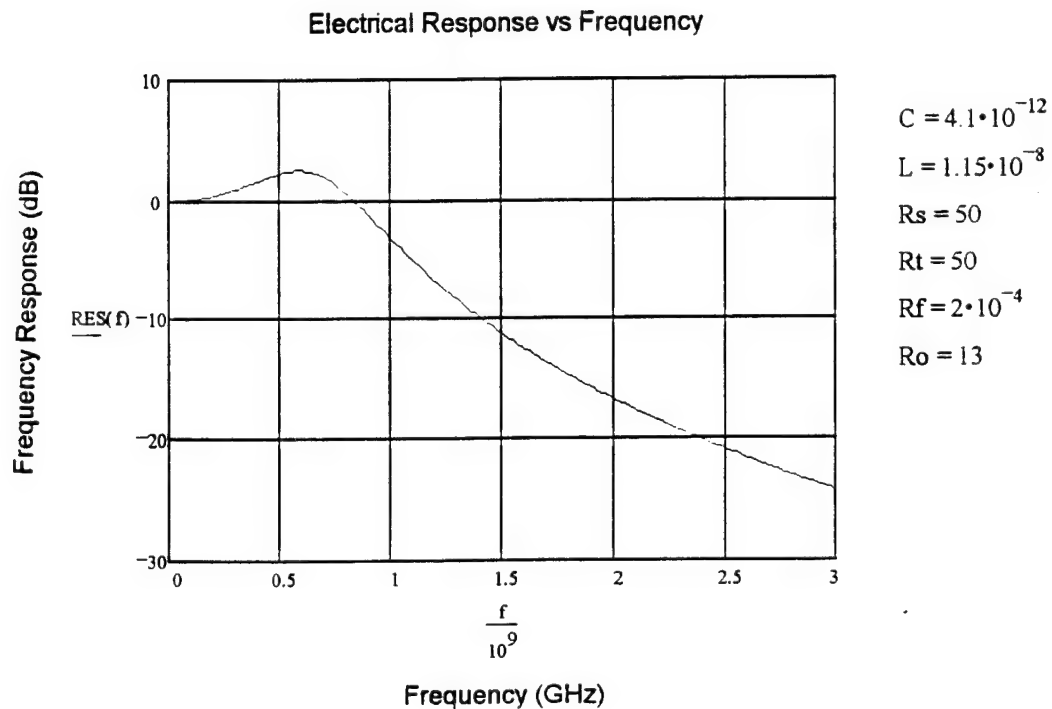


Figure 3-21
Frequency Response of POC Waveguide Modulator

3.1.10 **Fiber/Waveguide Pigtailling**

In order to implement the waveguide modulator arrays in the board-to-board interconnect prototype, the input portion of the waveguide must be pigtailed to a fiber which delivers laser light to the waveguide from a packaged laser diode. Currently, the laser diode is packaged with an FC-type fiber connector. Figure 3-22 shows the laser coupling and waveguide pigtailling. Experimental emphasis is on the fiber-to-waveguide pigtailling,

where interface loss must be reduced to allow more modulator output for backplane interconnects. Minimizing the pigtailing loss requires good optical alignment and good optical mode size matching between the fiber and the waveguide. The alignment is performed through a high-precision optical alignment stage, which provides five axes (three translational and two angular axes) of alignment control. Figure 3-23 shows a pigtailing alignment stage, where a fiber is pigtailed to a waveguide. UV-cure epoxy is used to fix the fiber and waveguide in position. In the future, a more stable and accurate soldering approach can be used.

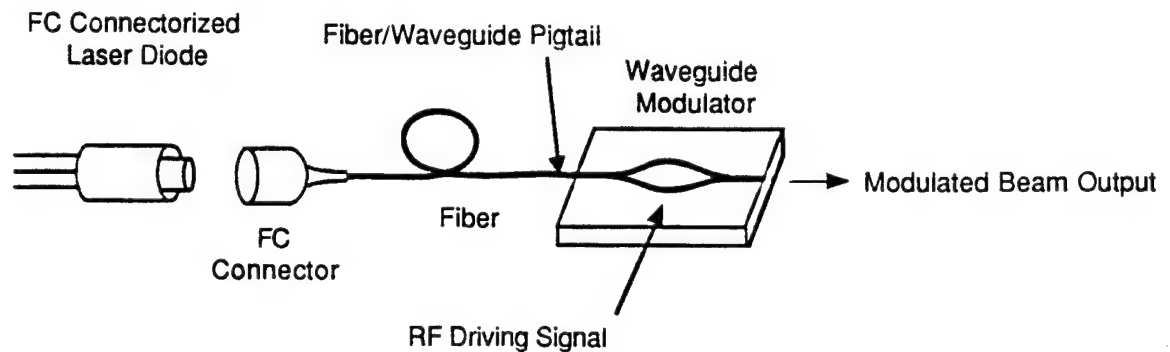


Figure 3-22
Laser, Fiber, and Waveguide Coupling

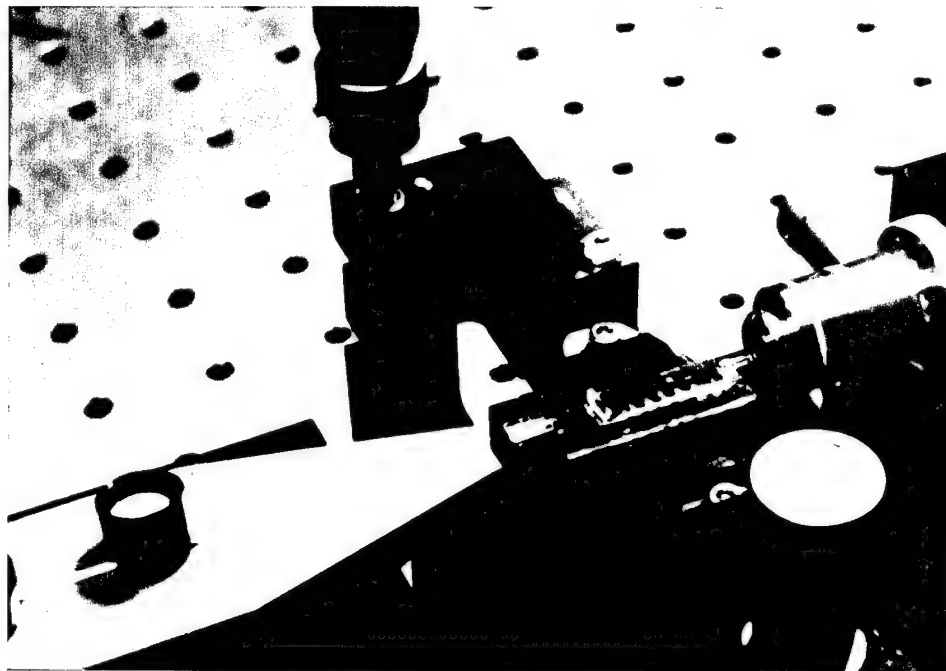


Figure 3-23
Optical Pigtailing Alignment Setup. Both the fiber and the waveguide are seen.

The optical output from the waveguide modulator is highly angular-divergent. A collimation lens is required to facilitate optical backplane coupling and interconnection. The use of a gradient index (GRIN) lens provides the easiest packaging and handling approach, and its small dimension is also attractive for array packaging. Figure 3-24 shows a packaged modulator unit with a fiber pigtail and an output collimation GRIN lens. Array packaging can be similarly done. Figure 3-25 shows the pigtailed modulator array.

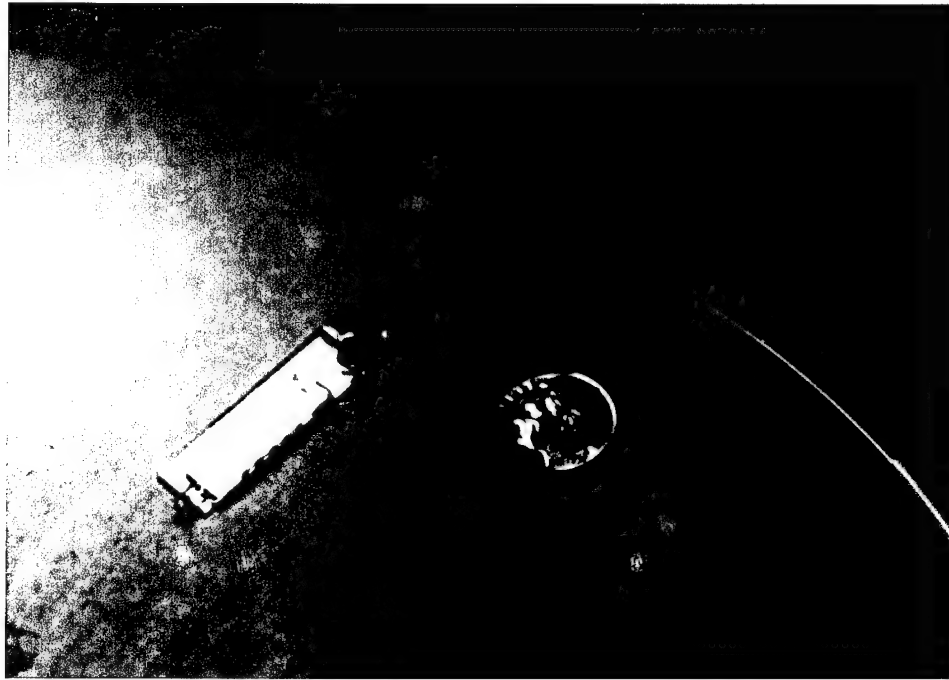


Figure 3-24
Packaged Modulator Unit with an Input Fiber and an Output Collimation GRIN Lens

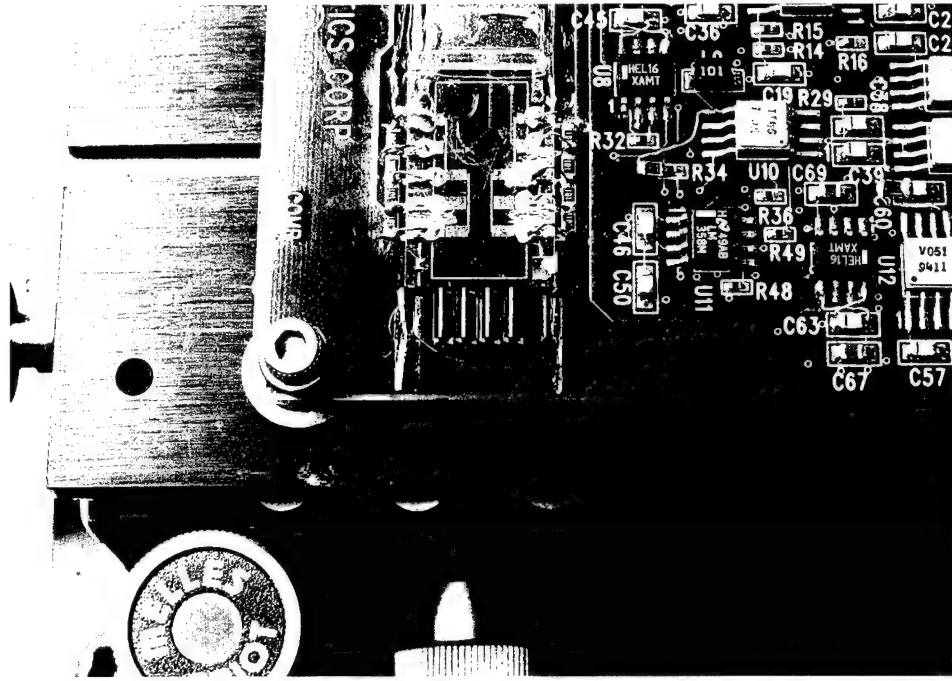


Figure 3-25
Pigtailed modulator Array with GRIN Lens Array

3.2 Receiver Fabrication for Mid-Program Prototype

The receiver is used to detect the light incident upon it and convert that to an electrical signal containing the information carried by the light. It contains a photodetector, a transimpedance amplifier, a post-amplifier (optional), and a signal conditioning circuit that recovers a digital signal; for example, back to the ECL level.

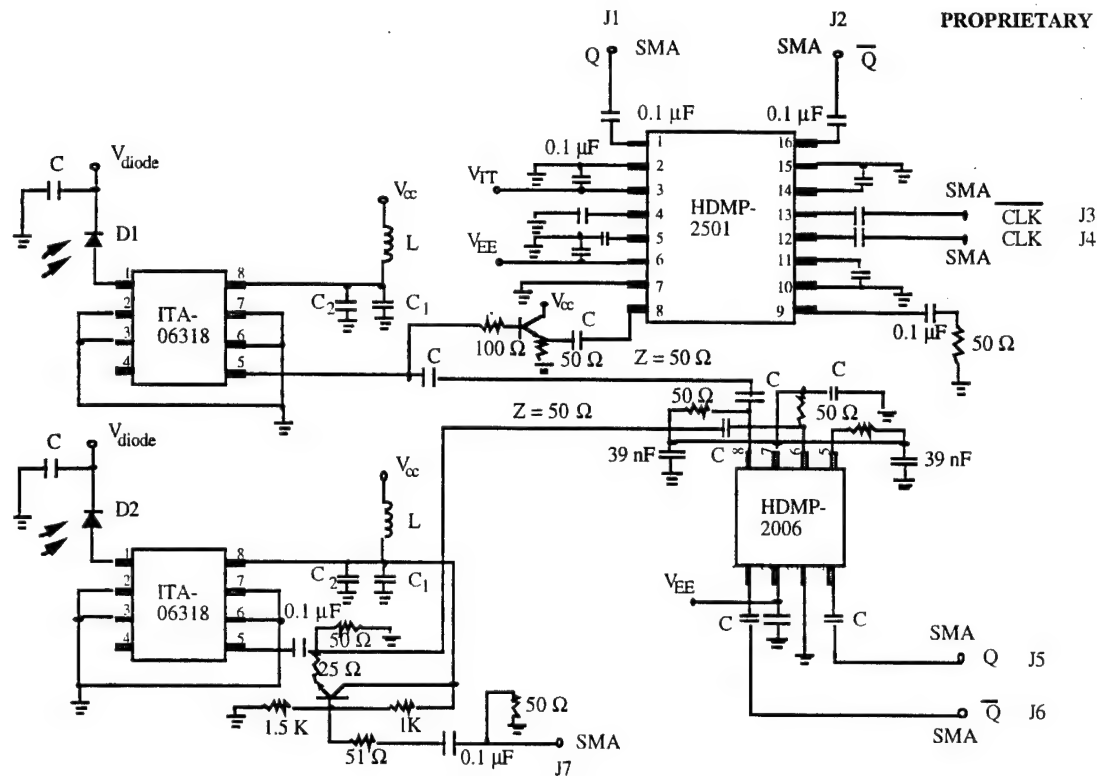
Surface mount photodetectors are commercially available. The rise and fall times can be about 0.15 ns and the operating speed can be greater than 2 GHz. Two commercial vendors can deliver ceramic packaged photodetectors: EG&G Optoelectronics, Canada and Fermionics Opto-Technology in California.

Transimpedance amplifiers for high-speed applications are manufactured by a number of companies, including Hewlett Packard, TriQuint Semiconductor, Anadigic, and AT&T Microelectronics. On the basis of speed, gain, packaging, and the number of external components, the HP transimpedance amplifier has been identified as better suited for our application. This transimpedance amplifier is the ITA-06318, with a hermetic glass/metal surface mount package. It can be used for 1.5 Gb/s applications. The transimpedance gain is 2800 Ω . An optical power of 1 μW can generate over 0.8 μA of detector current. At this high gain, the amplifier output can be over 2.24 mV. With 50 μW optical power, the

output can be 112 mV. Based on the sensitivity of a decision circuit (or comparator), the minimum optical power required can be between 1 μ W and 50 μ W to generate ECL digital output level. If the sensitivity of the decision circuit does not meet the requirement, a high-speed post-amplifier will be required. For example, the TriQuint amplifier TQ9122BN can serve as a post-amplifier, delivering a 25 dB small-signal gain at 1.575 GHz.

Since we have over 50 μ W of optical power after backplane beam propagations and couplings, we chose not to use a post amplifier for the mid-program prototype. Waveguides were not used at the receivers. The receiver design is shown in Figure 3-26. Of the two photodetectors (D1 and D2) in this design, D1 receives optical data from the backplane interconnect and D2 receives the optical clock signal from the same backplane interconnect. Both signals will be amplified by ITA-06318 transimpedance amplifiers. The amplified signals will be compared by a high-speed comparator (HDMP-2006 manufactured by HP) to recover the ECL logic level. In case no optical clock signal is available, an SMA (J7) connector allows the comparator clock signal to be provided electrically through a 50 Ω coaxial cable.

If only an optical data signal is available and no optical or electrical clock signal is provided, a clock and data recovery circuit (HDMP-2501) can function well at a frequency of 622 MHz. This chip is included for testing purposes, and may be useful for commercial communication applications, since in fiber communications only a data signal will be sent through the fiber.



$C = 0.1 \text{ mF}$ $C_1 = 0.01 \text{ mF}$ $C_2 = 1 \text{ mF}$ $L = 100 \text{ mH}$ $V_{IT} = -2 \text{ V}$ $V_{EE} = -5.2 \text{ V}$ $V_{CC} = +5 \text{ V}$
 L size 1206, $C = 0.1 \text{ mF}$ size 1206, C size 805, C_2 size 1206, 39 nF capacitor size 1206, and all resistors size 805.
 Detector size is 4.03 mm (0.16") long by 2.03 mm (0.08") wide. Surface mount type.
 Board size is 2" x 2".
 Transistor: NE68533 SOT 23 style.
 All capacitors not specified assume the value of 0.1 mF. Long interconnect lines for high frequency signals use 50 W transmission lines (thicker lines shown above).

Figure 3-26
A High-Speed Receiver Design

This optical receiver for the mid-program was fabricated and assembled. The overall board size is 2" x 2". Figure 3-27 shows the fabricated receiver module. Using a 1 Gb/s Bit-Error-Rate Generator, fabricated by POC in another program, we were able to test the receiver module. Based on the rise and fall time measurements, we determined that our receiver module can successfully operate at ~ 2 Gb/s, slightly exceeding the 1.5 Gb/s specified by the chip manufacturers. In conclusion, this first receiver prototype fabrication effort was very successful. The data rate meets the design specifications, and the knowledge gained from the Gb/s receiver design and fabrication proved useful for the fabrication of final program prototypes.

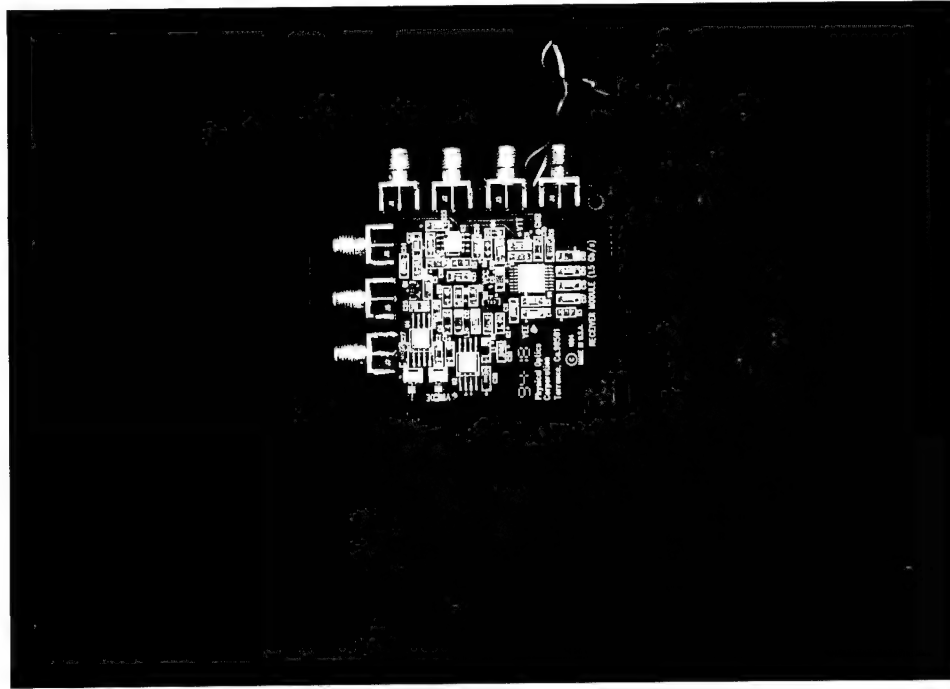


Figure 3-27
Fabricated 1.5 Gbits/s Optical Receiver Module

3.2.1 Design Guidelines Established from the Mid-Program Prototype

The overall sensitivity of the receiver is limited by the comparator. In order to achieve the minimum comparator input voltage level of 100 mV, the required input current at the transimpedance amplifier is 36 μA . Assume that the photodetector has a responsivity of 0.85 A/W; the required optical power at the detector is then 42 μW . If we can identify a better comparator, the overall sensitivity of the receiver can be significantly improved. For example, if we have a comparator requiring only a 20 mV input signal, the required optical power will become 8.4 μW , rather than 42 μW . Furthermore, a post-amplifier can be added to increase the overall sensitivity of the receiver. In general, we prefer a simple architecture without a post-amplifier, for compact packaging considerations. This improvement effort has been considered in the Phase II final prototype design.

3.2.2 Mid-Program Board-to-Board Optical Interconnect Prototype

In order to achieve the ultimate goal of demonstrating a successful board-to-board optical interconnect, we assembled a mid-program interconnect prototype for learning and testing purposes. The prototype consists of a transmitter board, an optical backplane, and a receiver board. The transmitter board is made of a PC board packaged with two waveguide modulators, both of which are fiber-pigtailed to the laser sources. The modulator outputs are packaged with GRIN lenses for light beam collimation for backplane interconnect purposes. Figure 3-28 shows the packaged waveguide modulator/transmitter. SMA connectors are used to connect the external drive signals to the modulators. In the present design, there are no amplifying electronics. This architecture can facilitate modulator packaging with multichip modules (MCMs) without complicating the MCM design.

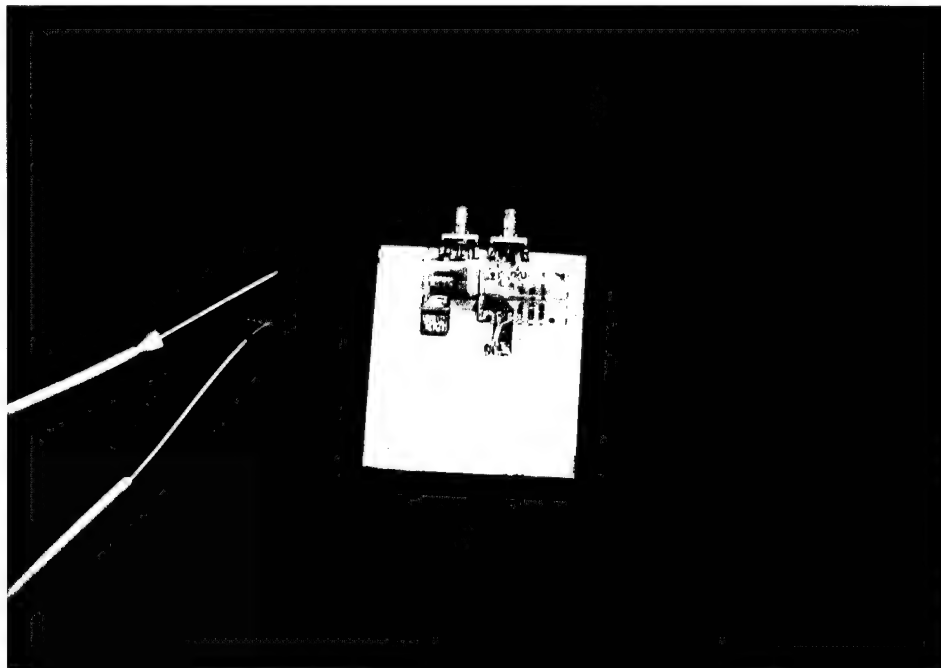


Figure 3-28
Packaged Waveguide Modulator Transmitter

Currently, the optical backplane consists of a piece of optical glass with its surface polished to optical quality. The thickness of the glass backplane is 5 mm, size is 2" by 2". In order to excite the backplane propagating beam with a normally incident beam from the transmitter board, we can either use a holographic diffraction grating (as shown in the

Phase I interconnect prototype), or a pair of optical prisms. Holographic diffraction has the advantage of compact packaging, but it suffers from chromatic sensitivity. When the laser wavelength is changed by environmental temperatures or by electrical bias, the backplane beam diffraction (or bouncing) angle will be affected. The effect can be significant when the backplane propagation distance is long (over several cm). The spatial shift of the optical beam near the receiver board can cause the backplane interconnect beams to miss the detectors at the receiver boards. This problem was addressed in Sections 2.2.5 and 2.2.6. Three holographic diffraction gratings are required in order to compensate for the effects of wavelength changes on the output diffraction angle and output beam position in the backplane. The fabrication of such a backplane is experimentally complicated, in that precise control of the holographic recording and hologram processing is required. Furthermore, hermetic protection is necessary to ensure the stability of the constructed holograms in a high-humidity environment.

There is a simple technique that can produce an achromatic coupling without holograms, based on a pair of prisms. The coupling structure was shown schematically in Figure 2-18. Here, a normally-incident beam from a transmitter interacts with the input prism. This excites the backplane propagating beam through surface reflection, which is wavelength-insensitive. Therefore, changes in laser wavelength will not affect the backplane beam angles and positions. An identical output prism vertically couples the substrate beam out to the receiver board. The position of the prisms will be adjusted in the prototype fabrication effort. Automatic packaging of prism positions for future automatic assembly of commercial optical backplanes is possible using advanced industrial tools. Figure 3-29 shows the packaged optical backplane for the present prototype demonstration. The overall backplane optical loss is about -3 dB.

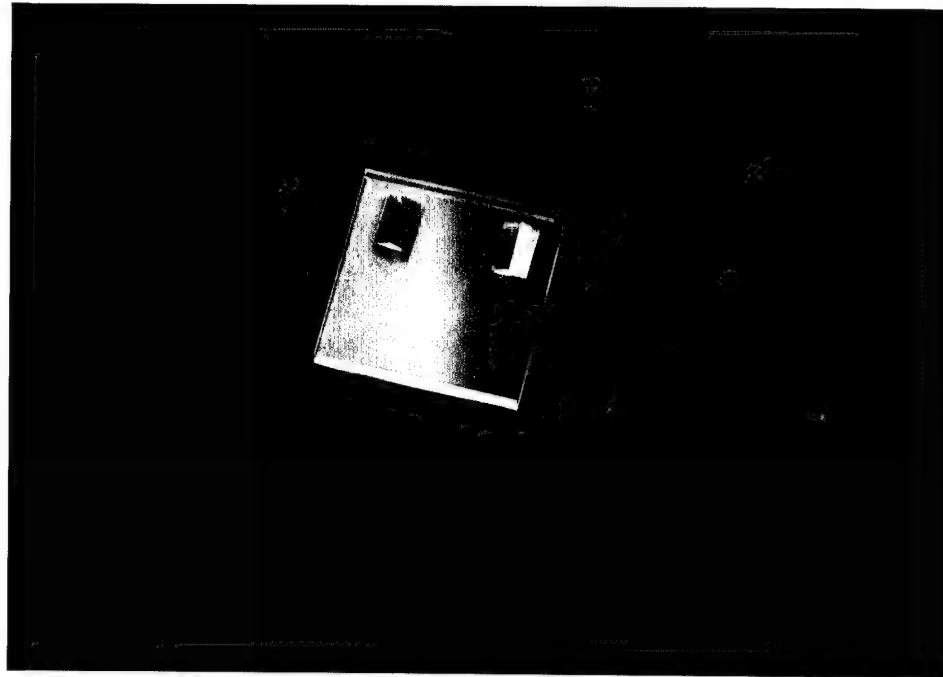


Figure 3-29
Photograph of the optical backplane constructed by a piece of polished optical glass and a pair of prisms.

The high speed optical receiver board has been discussed above. The goal of the interconnect prototype assembly process is to integrate the three system components (transmitter board, optical backplane, and receiver board) with good optical alignment, to achieve the desired optical interconnect performance. This alignment work has been carefully performed. Packaging hardware was fabricated to allow fine adjustments while at the same time achieving good mechanical strength. Figure 3-30 shows the fabricated mechanical hardware. Three board-holding slots are clearly observable. For each slot, there are three side adjustment screws and two vertical adjustment screws. The three side adjustment screws provide a lateral movement of the board and an angle adjustment. Note that the board can be slid in or out, providing another degree of lateral movement. The two bottom screws provide height and angle adjustments. Therefore, there are a total five degrees of adjustment freedom – three translational and two angular. By carefully controlling the combination of these adjustments, we can achieve the required board-to-board optical alignment. Figure 3-31 shows the packaged board-to-board optical interconnect prototype. When a modulation signal is applied to the transmitter, a similar signal is received at the optical receiver board. Figure 3-32 shows the interconnect performance. The received signal is tapped from the output of a transimpedance amplifier.

Direct reconversion of the digital signal to ECL is not possible in the present design, due to the relatively poor comparator sensitivity. Sensitivity improvement is considered in the final prototype.

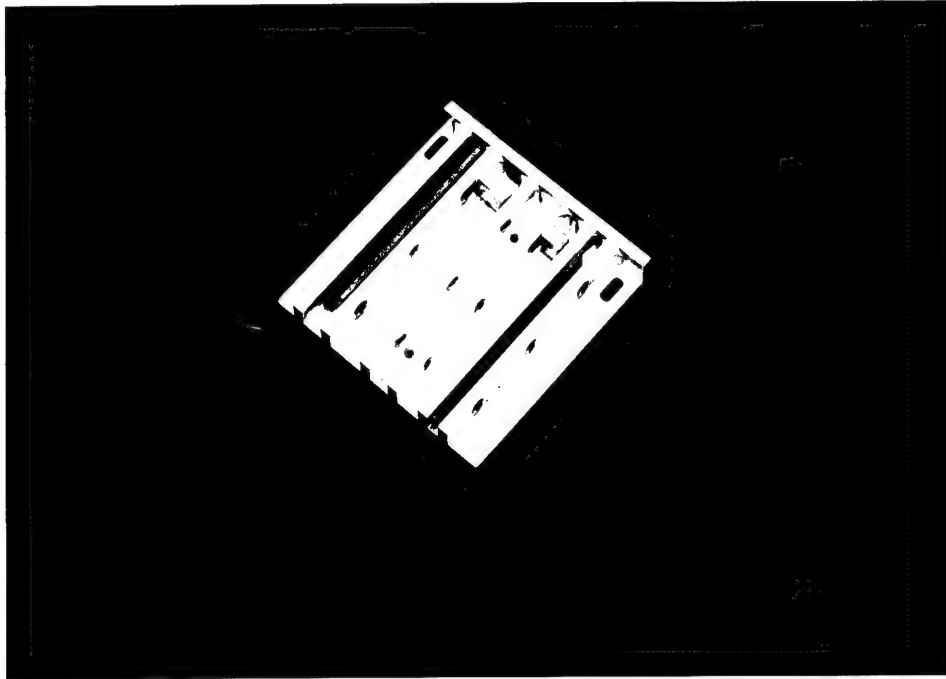


Figure 3-30
Packaging Hardware

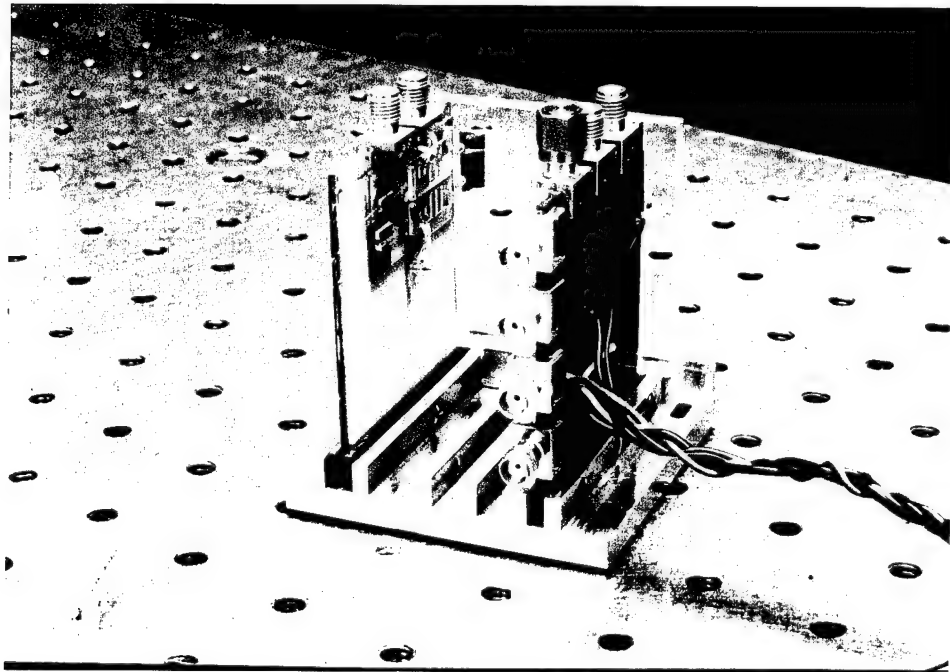


Figure 3-31
Packaged Board-to-Board Optical Interconnect Prototype

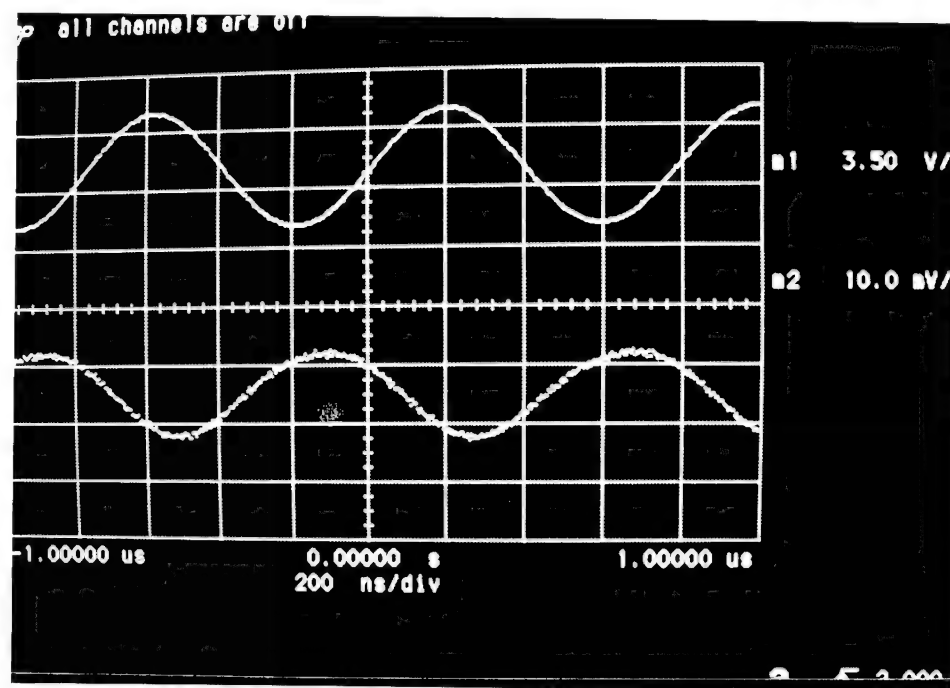


Figure 3-32
Photograph of the Interconnect Performance. The upper trace is the modulation signal applied to the transmitter board. The lower trace is the signal received at the receiver board through the backplane interconnect.

This mid-program prototype demonstrated an interconnect bandwidth of about 400 MHz. This bandwidth is limited by the transmitter packaging. Better transmitter packaging is considered in the Phase II final prototype.

3.3 Design and Fabrication of Final Prototype

The final Phase II prototype was fabricated to meet the approved revised contract requirements in Section 2.4. It consists of two electronic boards with optical components, laser diodes, an optical backplane, and packaging mechanical hardware. Figure 2-28 shows the schematic of the interconnect concept. The optical backplane is the same as the mid-program prototype demonstrated in the first year of the program. Optical prisms are used to deflect backplane interconnect light beams. The propagating light beams in the backplane are confined in the backplane glass by total internal reflection. The use of prisms instead of diffraction gratings can eliminate the chromatic sensitivity of the backplane light coupling.

The first circuit board consists of the following components: a waveguide modulator array chip, four GRIN lenses; a fiber ribbon with connector; a detector array, four receiver circuits; and four LED signal receiving indicators. Figure 2-29 showed a schematic of the first circuit board arrangement. External signal is used to drive the waveguide modulator array. The modulator outputs are coupled to the GRIN lens array. The beams are collimated and normally incident to the optical backplane. The prism on the backplane deflects the light beams to the total internal reflection condition of the glass, where the beams are confined in the backplane and are directed to the output prism location. The backplane output beams propagate again normal to the plane and are picked up by the GRIN lens array at the second circuit board.

The second circuit board consists of a GRIN lens array, a silicon V-groove, four multimode fibers, four detectors, four receiver circuits, four laser diode drivers, a TEC cooler, a laser diode array, a fiber ribbon and four LED signal receiving indicators. The schematic of the second circuit board is shown in Figure 2-30. When the signals are received at the GRIN lens array, they are coupled into the multimode fibers, which direct them to the appropriate receiver locations. The receiver circuits convert the optical signals back to electrical ones and send them out of the circuit board for comparison with original driver signals, and also to the laser diode drivers to drive the laser diode array for ribbon fiber communication. Another signal from each receiver circuit is sent to an LED driver to turn-on the LED, indicating the reception of the backplane signal. The laser diode outputs are modulated by the driver circuits. The cooling of the laser diodes is performed by a TEC control circuit. The modulated laser signals are coupled to the fiber ribbon. They are picked up by the detector array at the first circuit board through the ribbon fiber connection between the boards. Again, the received signals are converted back to electrical ones for comparison with the original driving signals. LEDs at the first board also are turned on, indicating the reception of the interconnect signals.

3.3.1 Design and Fabrication of Transmitter and Receiver Boards

The above description of the operating principle shows the completeness of the two backplane optical interconnects. Both circuit boards consist of transmitters and receivers. Figure 3-33 shows the receiver circuit schematic. The laser diode driver schematic is

shown in Figure 3-34. The laser cooling circuit for the second board is shown in Figure 3-35.

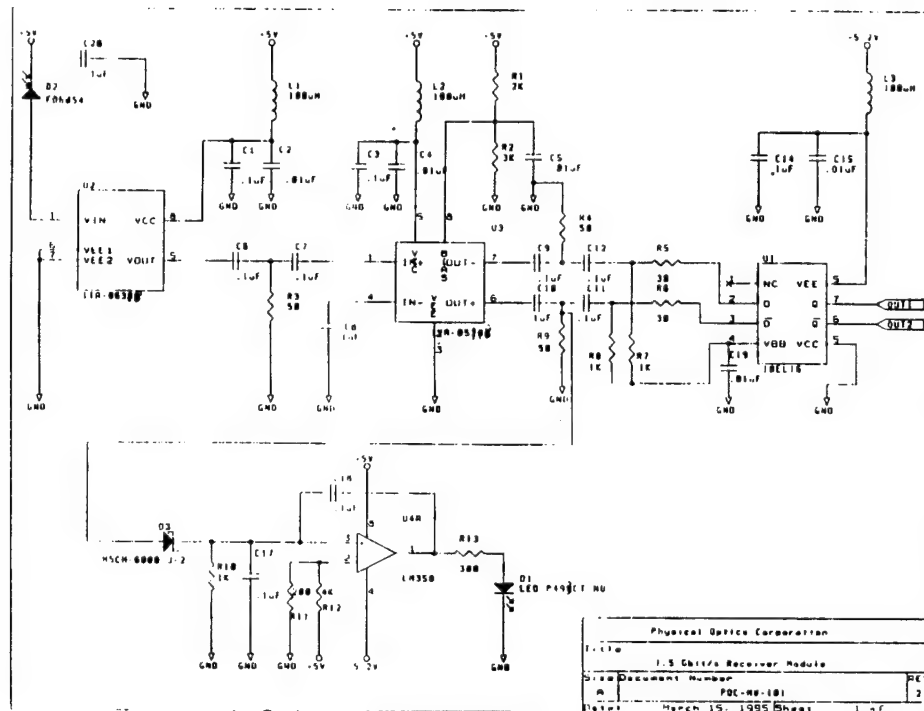


Figure 3-33
Schematic of the Receiver Circuit

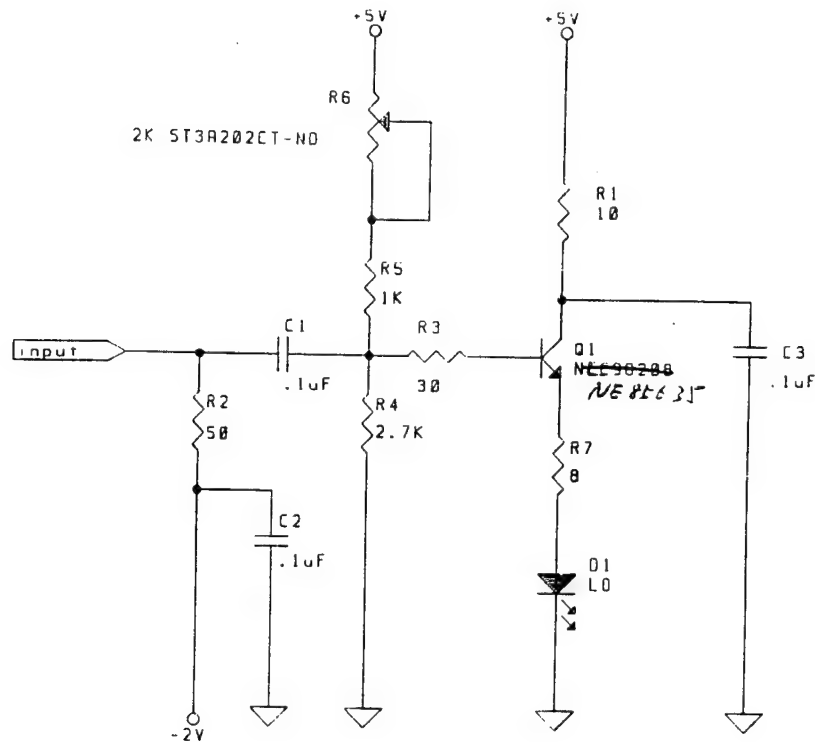


Figure 3-34
Schematic of Laser Driver Circuit

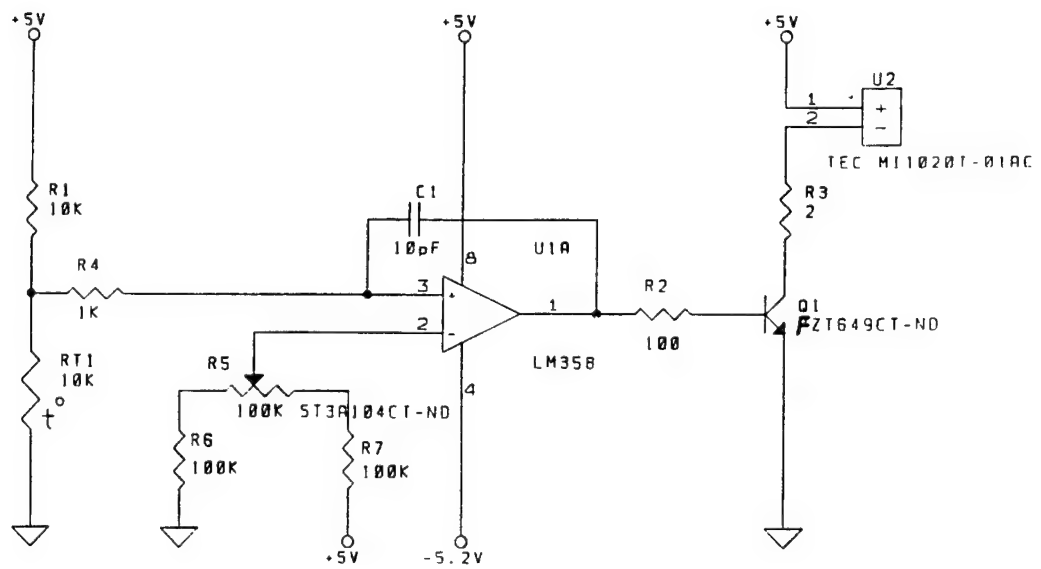


Figure 3-35
Schematic of Temperature Control Circuit for Laser Diode Array

3.3.2 Design and Fabrication of Prism-Glass Optical Backplane

The prism-glass optical backplane consists of two prisms and a 2" x 2" 5 mm thick BK7 glass substrate. It is the same as that of the mid-program prototype shown in Figure 3-29, except for the location of the prism pair.

3.3.3 Prototype Packaging Assembly and Interconnect Demonstration

Both the transmitter and receiver boards for the final prototype were fabricated using surface mount technology. This was for the demonstration; when actual MCM technology is used, all of electronic parts will be much smaller, and the boards can be smaller.

3.3.3.1 Assembly of the Phase II Interconnect Prototype

The final Phase II prototype consists of two electronic boards with optical components, laser diodes, an optical backplane, and a mechanical hardware package. A photograph of the interconnect prototype during assembly is shown in Figure 3-36. The optical backplane is the same as the initial prototype that was demonstrated in the first year of the program. Optical prisms are used to deflect any backplane interconnect light beams. The propagating light beams found in the backplane are confined by total internal reflection to the backplane glass.

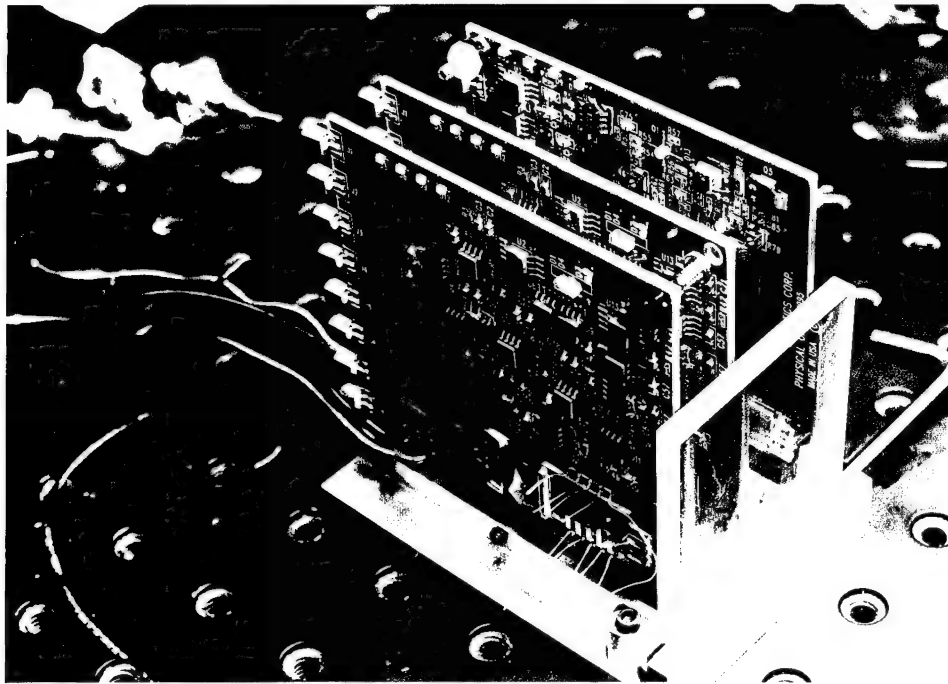


Figure 3-36
Final Prototype During Assembly

Figure 3-37 is a photograph of the first circuit board, which consists of a fiber pigtailed waveguide modulator chip, four GRIN lenses, a fiber ribbon, a photodetector array, four receiver circuits, and four LED signal receiving indicators. The current board size is 3.25" by 3.125". The board size can be smaller by close to one order of magnitude when hybrid circuit and MCM technology are used. According to the board design, the operating speed can be about > 1 Gbit/s.

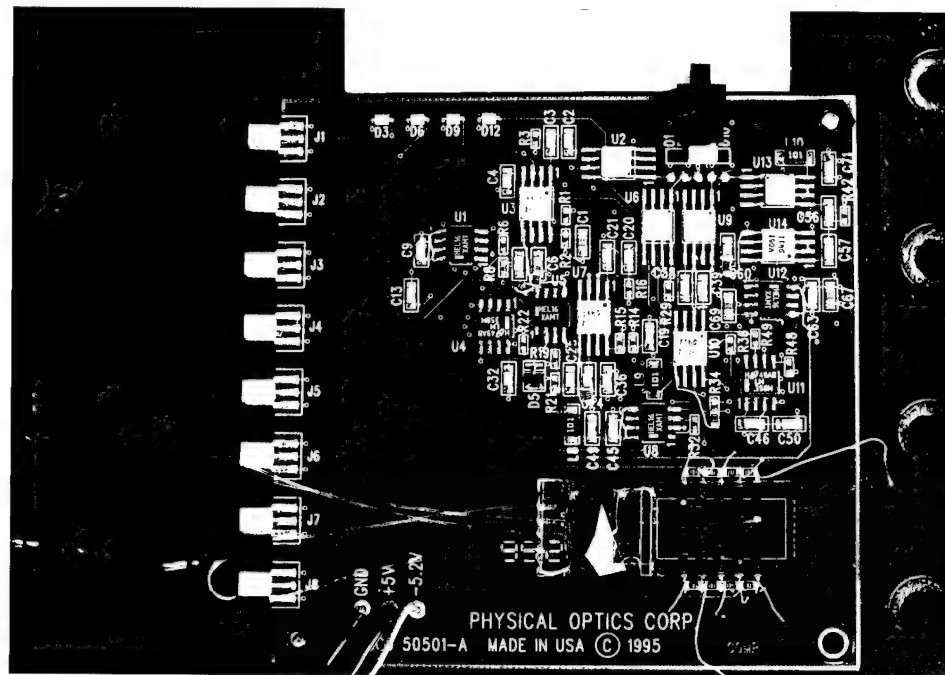


Figure 3-37
First Circuit Board in Assembly

The second circuit board consists of a GRIN lens array, a silicon V-groove, a TEC cooler, a laser diode array, a fiber ribbon, and four each of multimode fibers, detectors, receiver circuits, laser diode drivers, and LED signal receiving indicators. This board in assembly is shown in Figure 3-38. The multimode fibers for the receivers have a core diameter of about $100\text{ }\mu\text{m}$. The use of a large core diameter facilitates better signal reception from the backplane. Note that a high optical loss as demonstrated in the Phase I program comes from free-space beams coupling to single-mode waveguides. Using a large core diameter can significantly reduce this coupling loss. High speed photodetectors manufactured by Fermionics Opto-Technology, Inc. have an active area with a diameter of about $60\text{ }\mu\text{m}$. Optical coupling from a $100\text{ }\mu\text{m}$ diameter fiber to a $60\text{ }\mu\text{m}$ diameter photodetector has about -4.4 dB of optical loss. However, it greatly increases the tolerance on the fiber/detector packaging alignment. (The optical alignment is now simpler than coupling a $62.6\text{ }\mu\text{m}$ fiber to a $60\text{ }\mu\text{m}$ photodetector in which a major loss comes from the misalignment. In such a case, a small misalignment on the order of $20\text{ }\mu\text{m}$ can result in a coupling loss of about -10 dB .)

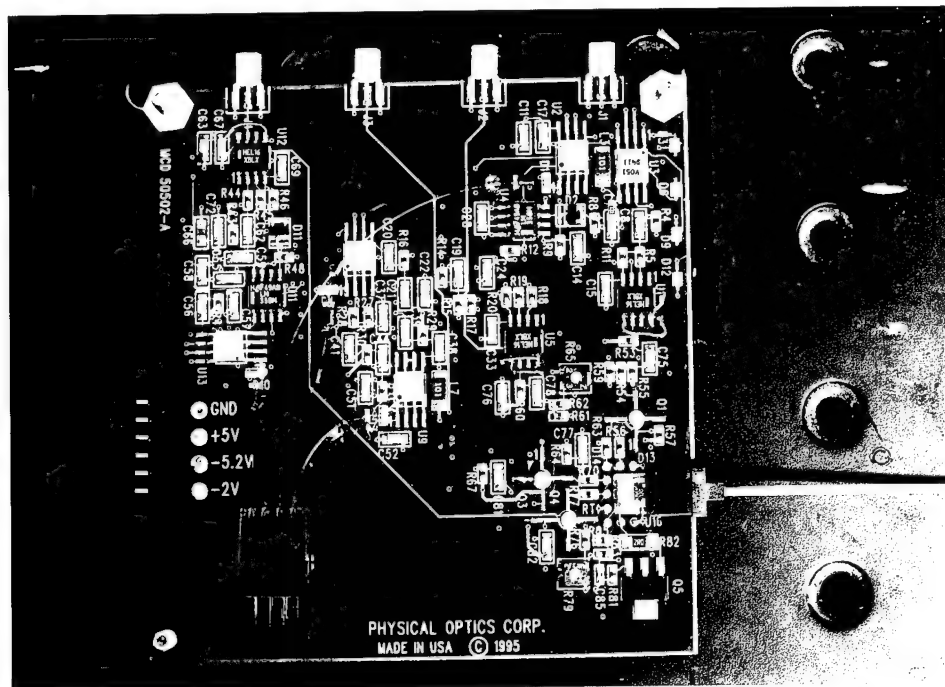


Figure 3-38
Second Circuit Board in Assembly

3.3.3.2 Other Phase II Delivery

The above circuit board demonstrated interconnection using an optical backplane and fiber ribbons. This was just one of the prototype delivered for the Phase II. Other deliveries include: 1) a fiber pigtailed 4-element modulator array chip (see Figure 3-39); 2) a single-fiber pigtailed modulator chip (see Figure 3-40); and 3) two additional un-pigtailed modulator chips (see Figure 3-41).

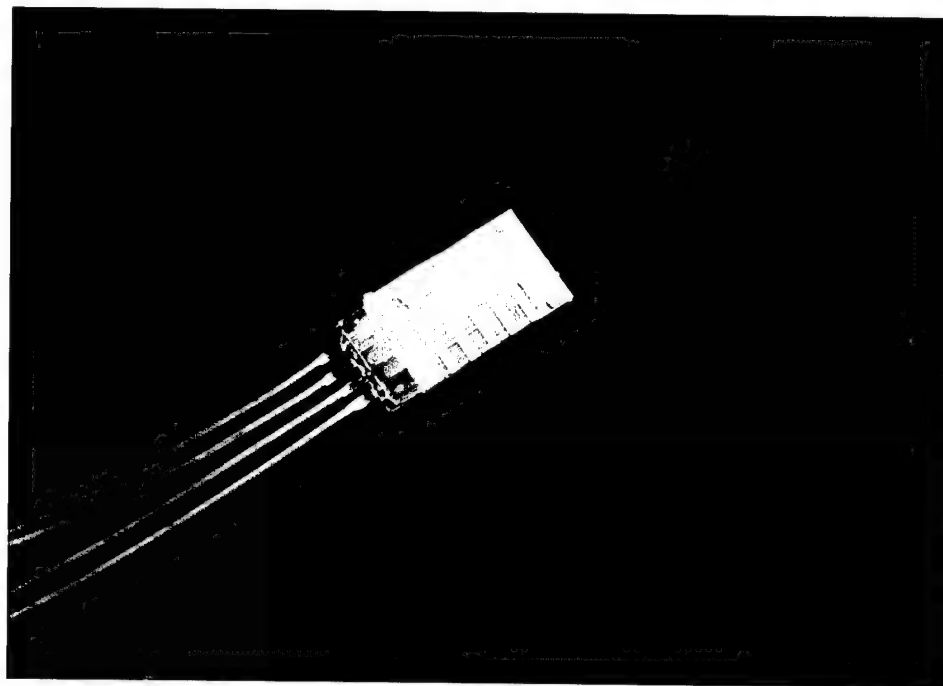


Figure 3-39
Fiber Pigtailed Four-Element Modulator Array Chip

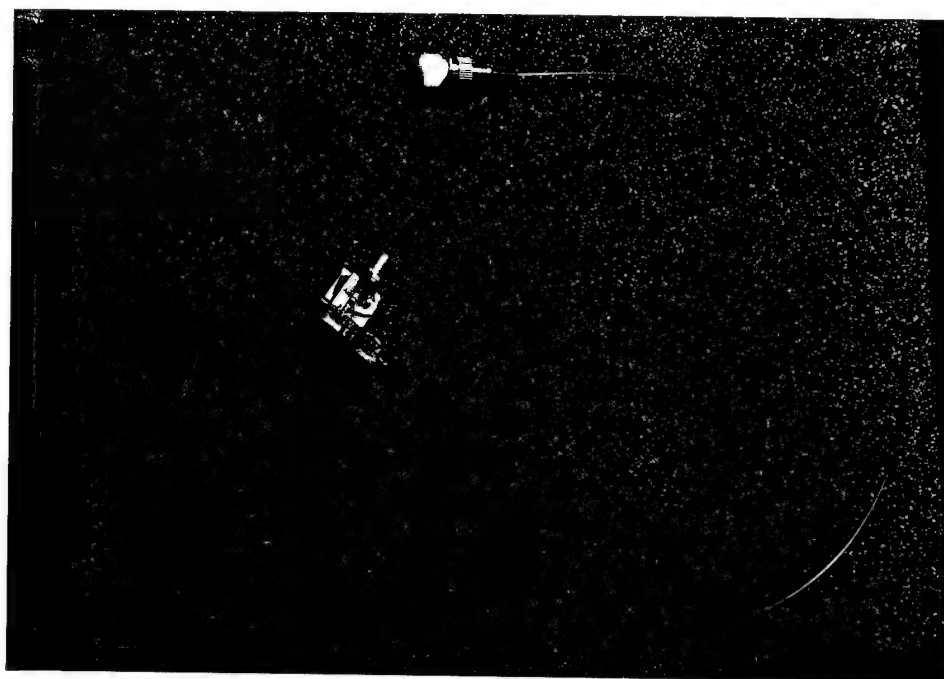


Figure 3-40
Single-Fiber Pigtailed Modulator Chip

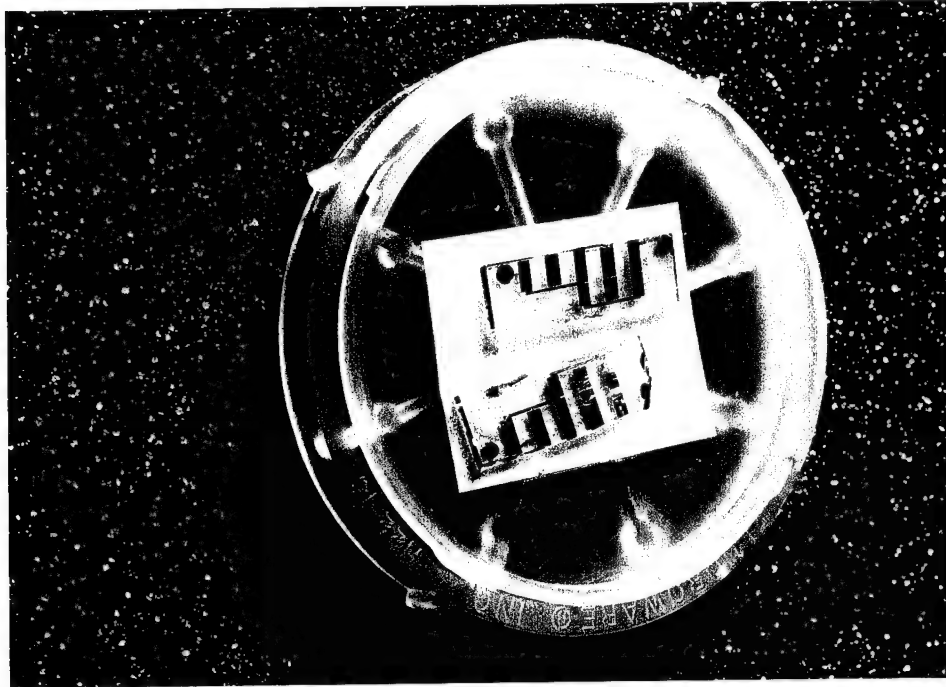


Figure 3-41
Two Additional Un-pigtailed Modulator Chips

3.4 Technical Difficulties Encountered in the Assembly of the Final Prototype

During the final assembly of the complete system prototype, many technical problems were encountered. A description of the problems and their solutions is given in the following sections.

3.4.1 Replacement of the Multimode Fibers to Improve Numerical Aperture (NA) Matching

As planned, four conventional multimode fibers (core/cladding ratio = 62.5/125 μ m) were initially used to transfer the light from the GRIN lens array to the photodetector array on the receiver board. Unfortunately, some unexpected optical power loss was found which affected the required power budget. This power loss was traced to a numerical aperture mismatch between the GRIN lens (NA = 0.35) and the multimode fiber (NA = 0.28). This problem has been solved by replacing the original fibers with new ones (core/cladding

ratio = 100/140 m and numerical aperture = 0.32). As a result, the optical power level has been recovered to the design parameters.

3.4.2 Reparation of Integrated Laser Diode Array and Detector Array

In accordance with the original plan, the final system assembly and alignment were performed in two main steps. The first step was to align a laser diode array on the receiver board to a photodetector array on the transmitter board through a fiber ribbon. During the process, a couple of unexpected problems were experienced. The first problem was a laser array dysfunction caused by end face contamination of the channel laser diode array. This was traced to a small glue spot stuck on the output surface of the bare laser chip, which significantly changed the reflection coefficient of the Fabry-Perot resonance cavity; thus, the laser was unable to reach the critical lasing condition. The second one was a laser array dysfunction caused by a loose bonding connection (either the original bonding connection was not strong enough and was loosened during transportation, or the technician carelessly touched the bonding wire). For each case, we had to replace the laser diode array and make a new bonding connection.

3.4.3 Solution of Over Heating Problems on the Receiver Board

During the initial assembly, it was found that the laser diode array always worked well at first with approximately 3 mW of total optical output power, but it then failed on subsequent efforts to operate it. After a laborious checking process, we found the source of the problem: the laser array was a chip-type of laser that only operates under 40° C while the local temperature on the originally designed board was near 50° C, because too much power was consumed by the original thermoelectric cooler (TEC) used. We solved this problem by changing the TEC and modifying the bias circuit. Now the laser diode array is working in the normal condition.

3.4.4 Repair of the Receiving Circuit Board

Circuit problems were found in both the high speed electronic transmitter board and the receiver board, which made the system's operation unstable; that is, sometimes it worked well, but other times it failed to function properly. The main difficulty is in the integration of the high speed electronic element array (instead of a single element). This array configuration introduces element-to-element crosstalk, cause circuit oscillation, increases the effective capacitance value (thus reducing operating speed), and creates electromagnetic interference. To address all of these problems, a new board design and packaging with good high frequency shielding between array elements is needed. Instead of initialing a new board activity, we re-engineered the existing boards. Although these re-engineering steps are not an optimal solution, it at least provided functional operation of the boards.

4.0 POTENTIAL APPLICATIONS

The high-density 3-D packaging and interconnection schemes proposed here for multichip module applications can be employed in DOD electronic systems to reduce size and weight, and to improve the speed of Very Large Scale Integration (VLSI), Application Specific Integrated Circuit (ASIC), and Very High Speed Integrated Circuit (VHSIC) multichip modules. They can improve the reliability of compactly packaged systems against radiation loss and electromagnetic interference. Due to the reduced use of electrical interconnects (used only to connect chip outputs with modulators and detectors), and the resulting reduced power consumption, an improvement in system thermal performance can also be expected. This compact 3-D-packaged system will be suitable for military applications. For example, it can be used in high-speed and reliable processors employed for rapid target recognition and missile interception. It can also be used to protect other military electronic systems against EMI-related electronic jamming. Civilian applications include forming high-speed MCM processors for medical image processing, data fusion, neural computing, and the construction of a new generation of high-speed 3-D, stacked, optoelectronic computers (see Figure 4-1). Applications in high-speed electronic instruments are a commercial goal. With this interconnect technique, computing speeds can exceed the present limit of several hundreds of MHz imposed primarily by the long electrical interconnects associated with long chip-to-chip and board-to-board distances. It will improve the performance and reduce the cost of high-speed electronic instruments such as signal generators, oscilloscopes, detector amplifiers, computers, and transceivers modules.

Hybrid packaged high speed optical and electronic computers could achieve computing speeds in excess of about 200 MHz. Furthermore, both high-speed laser transmitter arrays and receiver could find a large commercial market. Space programs can also benefit from the dimension and weight reductions, greater reliability, better system redundancy, and radiation-hard performance provided by this approach.

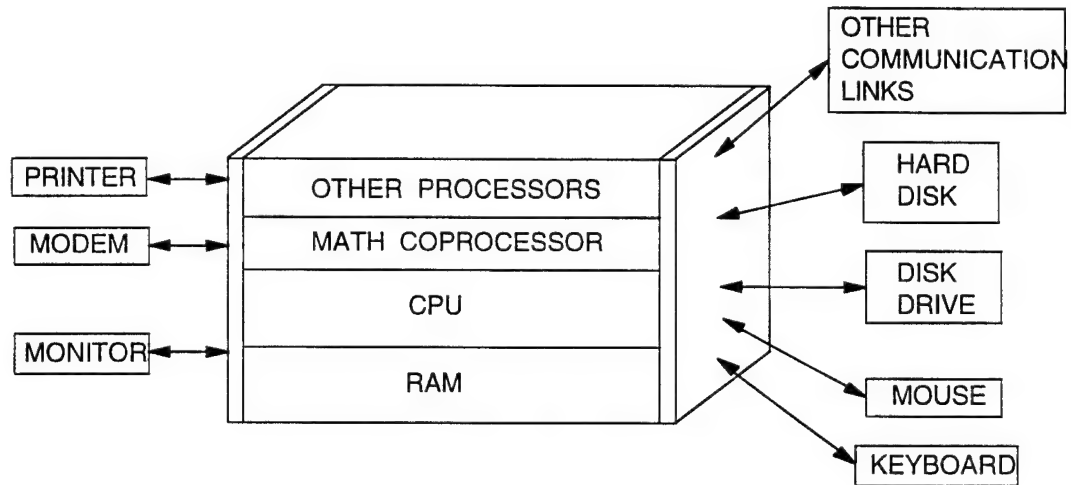


Figure 4-1
High-Speed Compact Packaged Hybrid Optic/electronic Computer

5.0 COMMERCIAL ACTIVITIES

Single-laser transmitters and detector receivers are commercially available. However, no transmitter or receiver arrays are commercially available for fiber ribbon communication applications. Physical Optics Corporation has identified this niche market during this program development period, and is developing transmitter and receiver arrays that can satisfy both the program requirements and also market needs.

To prototype a transmitter and receiver array, we have ordered packaging holders for laser arrays. Samples of laser arrays and detector arrays have been obtained from the Jet Propulsion Laboratory in Pasadena, California. Ribbon fibers have already been obtained. We have successfully packaged a laser transmitter array in a butterfly package with four fiber outputs. This package is shown in Figure 5-1. Other types of transmitter arrays (direct butt-coupling from laser arrays to fiber ribbons) and receiver arrays (direct butt-

coupling from fiber ribbons to detector arrays) are shown in Figures 5-2 and 5-3 respectively. More commercial effort from prototype to market is required.

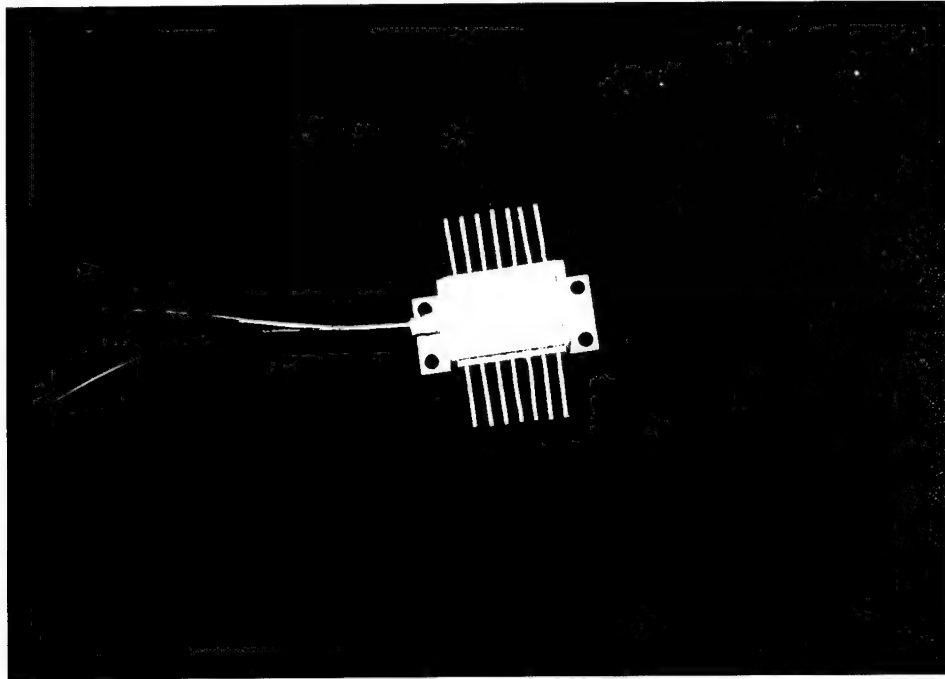


Figure 5-1
Packaged Laser Transmitter Array in a Butterfly Package with Temperature Control

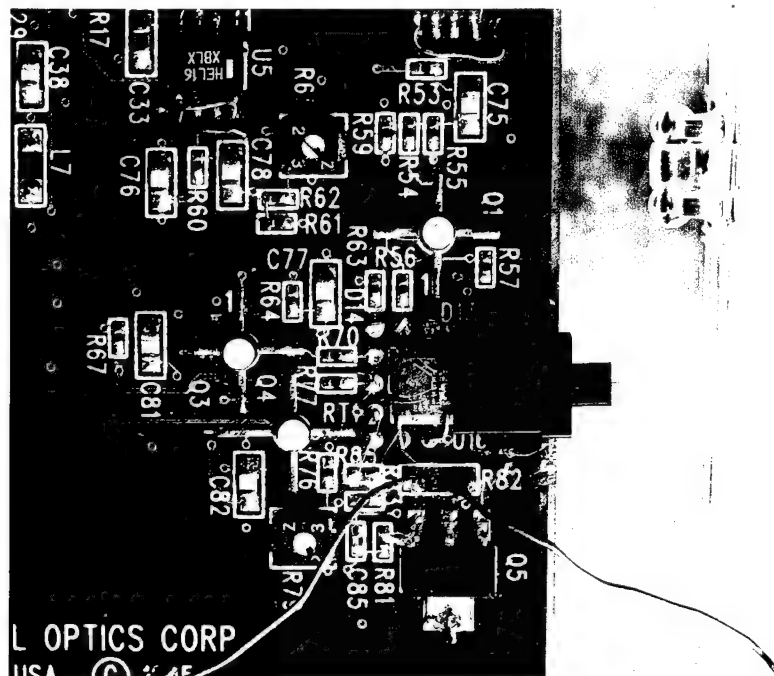


Figure 5-2
Another type of laser transmitter array with butt-coupling from laser array to fiber ribbon. The package can be very small when MCM technology is used for laser driving circuits.

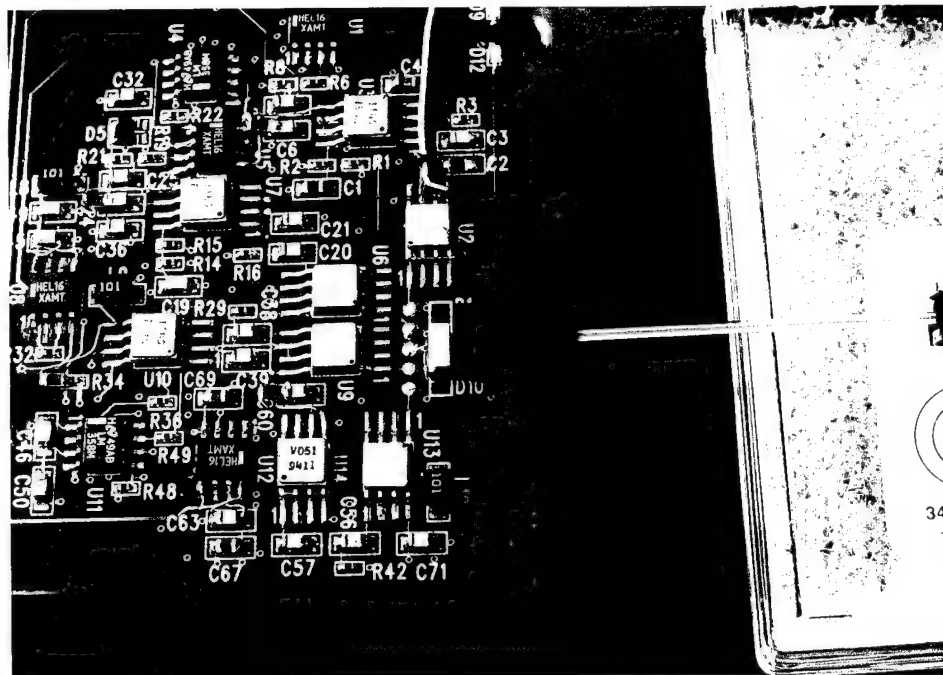


Figure 5-3
Receiver Array with Butt-Coupling from Fiber Ribbon to Photodetector Array. The package can be very small when MCM technology is used for receiver circuits.

6.0 PUBLICATIONS RESULTING FROM PROGRAM DEVELOPMENT

During Phase II program development, we have conducted some useful research studies. Some of the results are unique and thorough and are publishable. Two publications and two conference presentations have resulted from this program:

Publications:

1. M. R. Wang and F. Lin, "Design of Achromatic Holographic Grating Couplers for Substrate and Backplane Optical Interconnects," *Optics & Laser Technology* 26(4), 259-264 (1994) (an invited submission for the special edition on optical computing)
2. Guoda Xu, Michael R. Wang, and Freddie Lin, "Integrated Optical Mach-Zehnder Modulator Array for Optical Board-to-Board Interconnections," *Proceedings of SPIE*, Vol. 2291, 341-350 (1994)

Conference Presentations:

1. Michael R. Wang and Freddie Lin, "Design of Achromatic Holographic Grating Couplers for Backplane Optical Interconnects," Topical Meeting on Diffractive Optics: Design, Fabrication and Applications, Rochester, DMD2 (1994).
2. Guoda Xu, Michael R. Wang, and Freddie Lin, "Integrated Optical Mach-Zehnder Modulator Array for Optical Board-to-Board Interconnections," Conference of SPIE, on Integrated Optics and Microstructures II, San Diego (1994)

See Appendix A for publications.

7.0 CONCLUSION

In this program, we have conducted many research and development activities, including:

- Study, design, and analysis of the board-to-board optical interconnect structure.
- Design, fabrication, and testing of optical integrated waveguide devices such as channel waveguide, LiNbO₃ waveguide modulators, and modulator arrays.
- Design, fabrication, and testing of other devices needed to fabricate the board-to-board optical interconnect structure, including output beam collimation using GRIN lenses, backplane formation, and design and fabrication of optoelectronic transmitter and receiver array units.
- Construction of a mid-term and a final board-to-board optical interconnect system using the devices fabricated in the program. In the process of the final system construction, we encountered many difficulties in high speed optoelectronic circuits. This suggests further investigations are needed in this area.
- Construction and delivery of three optical board-to-board interconnect system devices: a fiber pigtailed 4-element array chip, a single fiber pigtailed modulator chip, and two un-pigtailed modulation chips.

In addition to the above technical efforts in this program, we have also identified many commercial application opportunities and scenarios. A few commercial device prototypes (laser transmitters and receivers) were designed and fabricated by us, in conjunction with NASA Jet Propulsion Laboratory. We are currently in the process of determining product positioning of these commercial prototypes and identifying the initial marketplaces to be focused on. It is expected that the technology developed in this program will provide a big contribution to these market/business opportunities.

8.0 REFERENCES

1. J. W. Goodman, F. J. Leonberger, S. Y. Kung, and R. A. Athale, "Optical Interconnections for VLSI Systems," *Proc. IEEE*, 72, 850 (1984)
2. L. D. Hutcheson, P. Haugen, and A. Husain, "Optical Interconnects Replace Hardwire," *IEEE Spectrum*, 24(3), 30 (1987)
3. "New Levels of Hybrid IC Density are Provided by Three-Dimensional Packaging," *Defense Sci.*, 7(5), 65 (1988)
4. M. R. Feldman, S. C. Esener, C. C. Guest, and S. H. Lee, "Comparison between Optical and Electrical Interconnects Based on Power and Speed Considerations," *Appl. Opt.*, 27, 1742 (1988)
5. P. R. Haugen, S. Rychnovsky, A. Husain, and L. D. Hutcheson, "Optical Interconnects for High Speed Computing," *Opt. Eng.*, 25, 1076 (1986)
6. D. H. Hartman, "Digital High Speed Interconnects: A Study of the Optical Alternative," *Opt. Eng.*, 25, 1086 (1986)
7. L. D. Hutcheson, "High Speed Optical Interconnects for Computing Applications," *Proc. SPIE*, 862, 2 (1987)
8. M. R. Feldman and C. C. Guest, "Interconnect Density Capabilities of Computer Generated Holograms for Optical Interconnection of Very Large Scale Integrated Circuits," *Appl. Opt.*, 28, 3134 (1989)
9. A. Guha, J. Bristow, C. Sullivan, and A. Husain, "Optical Interconnections for Massively Parallel Architectures," *Appl. Opt.*, 29, 1077 (1990)
10. B. D. Clymer and J. W. Goodman, "Optical Clock Distribution to Silicon Chips," *Opt. Eng.*, 25, 1103 (1986)
11. D. Z. Tsang, D. L. Smythe, A. Chu, and J. J. Lambert, "A Technology for Optical Interconnections Based on Multichip Integration," *Opt. Eng.*, 25, 1127 (1986)
12. E. E. E. Frietman, W. van Nifterick, L. Dekker, and T. J. M. Jongeling, "Parallel Optical Interconnects: Implementation of Optoelectronics in Multiprocessor Architectures," *Appl. Opt.*, 29, 1161 (1990)
13. K. Matsuda and J. Shibata, "Optical Interconnections and Optical Digital Computing Based on the Photonic Parallel Memory," *IEE Proc. J. Optoelectron.*, 138, 67 (1991)
14. M. R. Feldman and C. C. Guest, "Holograms for Optical Interconnects for Very Large Scale Integrated Circuits Fabricated by Electron-Beam Lithography," *Opt. Eng.*, 28, 915 (1989)
15. L. A. Bergman, W. H. Wu, A. R. Johnston, R. Nixon, S. C. Esener, C. C. Guest, P. Yu, T. J. Drabik, M. Feldman, and S. H. Lee, "Holographic Optical Interconnects for VLSI," *Opt. Eng.*, 25, 1109 (1986)
16. R. K. Kostuk, J. W. Goodman, and L. Hesselink, "Optical Imaging Applied to Microelectronic Chip-to-Chip Interconnections," *Appl. Opt.*, 24, 2851 (1985)

17. M. R. Feldman and C. C. Guest, "Computer Generated Holographic Optical Elements for Optical Interconnection of Very Large Scale Integrated Circuits," *Appl. Opt.*, 26, 4377 (1987)
18. F. B. McCormick and M. E. Prise, "Optical Circuitry for Free-Space Interconnections," *Appl. Opt.*, 29, 2013 (1990)
19. T. Sakano, T. Matsumoto, K. Noguchi, and T. Sawabe, "Design and Performance of a Multiprocessor System Employing Board-to-Board Free-Space Optical Interconnections: COSINE-1," *Appl. Opt.*, 30, 2334 (1991)
20. S. Kawai and Y. Kohga, "Computer-Generated Holograms for Free-Space Optical Interconnections," *Japan. J. Appl. Phys. 2 - Lett.*, 30, L2101 (1991)
21. H. M. Ozaktas, Y. Amitai, and J. W. Goodman, "Comparison of System Size for Some Optical Interconnection Architectures and the Folded Multi-Facet Architecture," *Opt. Comm.*, 82, 225 (1991)
22. A. Dickinson and M. E. Prise, "Free-Space Optical Interconnection Scheme," *Appl. Opt.*, 29, 2001 (1990)
23. D. Z. Tsang, "One-Gigabit per Second Free-Space Optical Interconnection," *Appl. Opt.*, 29, 2034 (1990)
24. M. R. Feldman, C. C. Guest, T. J. Drabik, and S. C. Esener, "Comparison between Electrical and Free-space Optical Interconnects for Fine Grain Processor Arrays Based on Interconnect Density Capabilities," *Appl. Opt.*, 28, 3820 (1989)
25. J. A. Fried, "Optical I/O for High Speed CMOS Systems," *Opt. Eng.*, 25, 1132 (1986)
26. P. M. Kopera, "Reliability of Passive Fiber-Optic Interconnects," *Fiber Integrat. Opt.*, 9, 53 (1990)
27. Y. Yamada, M. Yamada, H. Terui, and M. Kobayashi, "Optical Interconnections Using A Silica-Based Waveguide on A Silicon Substrate," *Opt. Eng.*, 28, 1281 (1989)
28. S. E. Schacham, H. Merkelo, L. T. Hwang, B. D. McCredie, M. S. Veatch, and I. Turlik, "Comparative Evaluation of Optical Waveguides as Alternative Interconnections for High Performance Packaging," *IEEE Trans. Compon. Hybrid. Manufac. Tech.*, 15, 63 (1992)
29. C. S. Li, C. M. Olsen, and D. G. Messerschmitt, "Analysis of Crosstalk Penalty in Dense Optical Chip Interconnects Using Single-Mode Waveguides," *J. Lightwave Technol.*, 9, 1693 (1991)
30. F. Lin, E. M. Strzelecki, and T. Jannson, "Optical Multiplanar VLSI Interconnects Based on Multiplexed Waveguide Holograms," *Appl. Opt.*, 29, 1126 (1990)
31. R. K. Kostuk, M. Kato, and Y. T. Huang, "Polarization Properties of Substrate-Mode Holographic Interconnects," *Appl. Opt.*, 29, 3848 (1990)
32. R. K. Kostuk, Y. T. Huang, D. Hetherington, and M. Kato, "Reducing Alignment and Chromatic Sensitivity of Holographic Optical Interconnects with Substrate-Mode Holograms," *Appl. Opt.*, 28, 4939 (1989)
33. Y. Amitai and J. W. Goodman, "Design of Substrate-Mode Holographic Interconnects with Different Recording and Readout Wavelengths," *Appl. Opt.*, 30, 2376 (1991)
34. J. Jahns and A. Huang, "Planar Integration of Free-Space Optical Components," *Appl. Opt.*, 28, 1602 (1989)
35. H. J. Haumann, H. Kobolla, F. Sauer, J. Schmidt, J. Schwider, W. Stork, N. Streibl, and R. V_ikel, "Optoelectronic Interconnection Based on Light Guiding Plate with Holographic Coupling Elements," *Opt. Eng.*, 30, 1620 (1991)
36. K. H. Brenner and F. Sauer, "Diffractive-Reflective Optical Interconnects," *Appl. Opt.*, 27, 4251 (1988)
37. T. Kubota and M. Takeda, "Array Illuminator Using Grating Couplers," *Opt. Lett.*, 14, 651 (1989)

38. M. Kato, Y. T. Huang, and R. K. Kostuk, "Multiplexed Substrate-Mode Holograms," *J. Opt. Soc. Am. A*, 7, 1441 (1990)
39. M. M. Downs and J. Jahns, "Integrated-Optical Array Generator," *Opt. Lett.*, 15, 769 (1990)
40. F. Sauer, "Fabrication of Diffractive-Refractive Optical Interconnects for Infrared Operation Based on Total Internal Reflection," *Appl. Opt.*, 28, 386 (1989)
41. P. Chavel and J. Taboury, "On Alleged and Real Advantages of Optical Interconnects: Examples," *Annales De Physique*, 16, 153 (1991)
42. M. R. Wang, G. J. Sonek, R. T. Chen, and T. Jansson, "Large Fanout Optical Interconnects Using Thick Holographic Gratings and Substrate Wave Propagation," *Appl. Opt.*, 31, 236-249 (1992)
43. R. T. Chen, H. Lu, D. Robinson, M. Wang, G. Savant, and T. Jansson, "Guided-Wave Planar Optical Interconnects Using Highly Multiplexed Polymer Waveguide Holograms," *J. Lightwave Technol.*, 10, 888-897 (1992)
44. M. R. Wang, G. J. Sonek, R. T. Chen, and T. Jansson, "Five-Channel Polymer Waveguide Wavelength Division Demultiplexer for the Near Infrared," *IEEE Photon. Technol. Lett.*, 3, 36-38 (1991)
45. R. A. Becker, "Broad-Band Guided-Wave Electro-optic Modulators," *IEEE J. Quantum Electron.*, QE-20, 723-727 (1984)
46. R. C. Alferness, "Guided-Wave Devices for Optical Communication," *IEEE J. Quantum Electron.*, QE-17, 946-959 (1981)
47. A. Neyer, "Electro-optic X-Switching Using Single Mode Ti-LiNbO₃ Channel waveguides," *Electron. Lett.*, 19, 533 (1983)
48. R. T. Chen and C. S. Tsai, "Thermal Annealed Single-Mode Proton Exchanged Channel Waveguide Cut Off Modulator," *Opt. Lett.*, 11, 546 (1986)
49. R. C. Alferness, "Efficient Waveguide Electro-optic TE - TM Mode Converter/Wavelength Filter," *Appl. Phys. Lett.*, 36, 513-515 (1980)
50. G. L. Tangonan, D. L. Persechini, J. F. Lotspeich, and M. K. Barnoski, "Electro-optic Diffraction Modulation in Ti-Diffused LiTaO₃," *Appl. Opt.*, 17, 3259-3263 (1978)
51. Y. K. Lee, and S. Wang, "Electro-optic Guided-to-Unguided Mode Converter," *IEEE J. Quantum Electron.*, QE-12, 273-281 (1976)
52. H. Onodera, I. Awai, M. Nakajima, and J. I. Ikenoue, "Light Intensity Modulation Based on Guided-to-Radiation Mode Coupling in Heterostructure Waveguides," *Appl. Opt.*, 23, 118-123 (1984)
53. H. Onodera and M. Nakajima, "High-Efficiency Light Modulator Using Guided-to-Radiation Mode Coupling in a Graded-Index Waveguide," *Appl. Opt.*, 25, 2175-2183 (1986)
54. D. Maucuse, "Electro-optic Coupling Between TE and TM Modes in Anisotropic Slabs," *IEEE J. Quantum Electron.*, QE-11, 759-767 (1975)
55. Michael R. Wang, Guoda Xu, Freddie Lin, and Tomasz Jansson, "Single-Mode/Multimode Waveguide Electro-optic Grating Coupler Modulator," *Appl. Phys. Lett.*, 66(20), 2628-2630 (1995)
56. R. Lytel, "Applications of Electro-optic Polymers to Integrated Optics," *SPIE*, 1216, 30-40 (1990).
57. S. Y. Wang, S. H. Lin, and M. Huong, "GaAs Traveling Wave Polarization Electro-optic Waveguide Modulator with Bandwidth in Excess of 20 GHz at 1.3 μ m," *Appl. Phys. Lett.*, 51, 83 (1987)
58. R. G. Hunsperger, "Integrated Optics: Theory and Technology," Springer Series in Optical Sciences, Third Edition, 1991.
59. E. A. J. Marcatilli, "Dielectric Rectangular Waveguide and Directional Coupler for Integrated Optics," *The Bell System Technical Journal*, pp.2071 (1969)
60. H. Kogelnik, "Coupled Wave theory for Thick Hologram Gratings," *Bell System Technol. J.*, 48, 2909-2947 (1969)

61. J. L. Jackel, C. E. Rice, and J. J. Veselka, "Proton Exchange for High-Index Waveguides in LiNbO₃," Appl. Phys. Lett., 41, 607 (1982)
62. J. L. Jackel, C. E. Rice, and J. J. Veselka, "Proton Exchange in LiNbO₃,"
63. N. A. Sanford, W. E. Lee, "Analysis of Proton Exchanged Channel Waveguides in LiNbO₃," Proc. SPIE, 578, 7 (1985)
64. M. Goodwin and C. Stewart, "Proton-Exchanged Optical Waveguides in Y-Cut Lithium Niobate," Electron. Lett., 19, 223-225 (1983)

ARMY RESEARCH LABORATORY
PHYSICAL SCIENCES DIRECTORATE
MANDATORY DISTRIBUTION LIST

August 1995
Page 1 of 2

Defense Technical Information Center*
ATTN: DTIC-OCC
8725 John J. Kingman Rd STE 0944
Fort Belvoir, VA 22060-6218
(*Note: Two DTIC copies will be sent
from STINFO office, Ft Monmouth, NJ)

Advisory Group on Electron Devices
ATTN: Documents
Crystal Square 4
1745 Jefferson Davis Highway, Suite 500
(2) Arlington, VA 22202

Director
US Army Material Systems Analysis Actv
ATTN: DRXSY-MP
(1) Aberdeen Proving Ground, MD 21005

Commander, CECOM
R&D Technical Library
Fort Monmouth, NJ 07703-5703
(1) AMSEL-IM-BM-I-L-R (Tech Library)
(3) AMSEL-IM-BM-I-L-R (STINFO Ofc)

Commander, AMC
ATTN: AMCDE-SC
5001 Eisenhower Ave.
(1) Alexandria, VA 22333-0001

Director
Army Research Laboratory
ATTN: AMSRL-D (John W. Lyons)
2800 Powder Mill Road
(1) Adelphi, MD 20783-1197

Director
Army Research Laboratory
ATTN: AMSRL-DD (COL Thomas A. Dunn)
2800 Powder Mill Road
(1) Adelphi, MD 20783-1197

Director
Army Research Laboratory
2800 Powder Mill Road
Adelphi, MD 20783-1197
(1) AMSRL-OP-SD-TA (ARL Records Mgt)
(1) AMSRL-OP-SD-TL (ARL Tech Library)
(1) AMSRL-OP-SD-TP (ARL Tech Publ Br)

Directorate Executive
Army Research Laboratory
Physical Sciences Directorate
Fort Monmouth, NJ 07703-5601
(1) AMSRL-PS
(1) AMSRL-PS-T (M. Hayes)
(1) AMSRL-OP-FM-RM
(22) Originating Office

ARMY RESEARCH LABORATORY
PHYSICAL SCIENCES DIRECTORATE
SUPPLEMENTAL DISTRIBUTION LIST
(ELECTIVE)

August 1995
Page 2 of 2

- Deputy for Science & Technology
Office, Asst Sec Army (R&D)
(1) Washington, DC 20310

- Cdr, Marine Corps Liaison Office
ATTN: AMSEL-LN-MC
(1) Fort Monmouth, NJ 07703-5033

- HQDA (DAMA-ARZ-D/
Dr. F.D. Verderame)
(1) Washington, DC 20310

- Director
Naval Research Laboratory
ATTN: Code 2627
(1) Washington, DC 20375-5000

- USAF Rome Laboratory
Technical Library, FL2810
ATTN: Documents Library
Corridor W, STE 262, RL/SUL
26 Electronics Parkway, Bldg 106
Griffiss Air Force Base
(1) NY 13441-4514

- Dir, ARL Battlefield
Environment Directorate
ATTN: AMSRL-BE
White Sands Missile Range
(1) NM 88002-5501

- Dir, ARL Sensors, Signatures,
Signal & Information Processing
Directorate (S3I)
ATTN: AMSRL-SS
2800 Powder Mill Road
(1) Adelphi, MD 20783-1197

- Dir, CECOM Night Vision/
Electronic Sensors Directorate
ATTN: AMSEL-RD-NV-D
(1) Fort Belvoir, VA 22060-5806

- Dir, CECOM Intelligence and
Electronic Warfare Directorate
ATTN: AMSEL-RD-IEW-D
Vint Hill Farms Station
(1) Warrenton, VA 22186-5100